Materials Technology Reports

https://ojs.acad-pub.com/index.php/MTR

ACADEMIC
ACADEMIC PUBLISHING PTE LTD

2024 VOLUME 2 ISSUE 2
ISSN: 3029-2646 (Online)

2

Editorial Team

Editor-in-Chief

Editorial Board Members

Maiyong Zhu
Jiangsu University
China

Aqib Mashood Khan
Nanjing University of Aeronautics and Astronautics
China

Volume 2 Issue 2 • 2024

Materials Technology Reports

ACADEMIC
ACADEMIC PUBLISHING PTE LTD

2024 | Volume 2 | Issue 2

Materials Technology Reports

https://ojs.acad-pub.com/index.php/MTR

Contents

Articles

Reviews

96 Thermoelectric materials—Challenges, approaches and classes

N. Karthikeyan, C. Prabhakaran, R. Akilan

Materials Technology Reports 2024, 2(2), 1630.
https://doi.org/10.59400/mtr1630

Article

Microwave absorption properties and mechanism of novel apatite-type materials $Mn_2Gd_{7.5}Ce_{0.5}(SiO_4)_6O_2$

Haikun Liu[1,*], Xiaoming Liu[1], Ning Liu[2,3], Lefu Mei[3]

[1] National Center of Technology Innovation for Display, Guangdong Juhua Research Institute of Advanced Display, Guangzhou 510525, China
[2] School of Science, China University of Geosciences, Beijing 100083, China
[3] School of Materials Science and Technology, China University of Geosciences, Beijing 100083, China
*** Corresponding author:** Haikun Liu, liuhk@nctid.com

CITATION

Liu H, Liu X, Liu N, Mei L. Microwave absorption properties and mechanism of novel apatite-type materials $Mn_2Gd_{7.5}Ce_{0.5}(SiO_4)_6O_2$. Materials Technology Reports. 2024; 2(2): 1630. https://doi.org/10.59400/mtr1630

ARTICLE INFO

Received: 20 August 2024
Accepted: 18 October 2024
Available online: 20 November 2024

Abstract: Manganese minerals possess a high intrinsic magnetic moment, making them excellent materials for microwave absorption. Rare earth elements, with their unique electronic structures and interactions between spin electrons and orbitals, can further enhance the performance of absorbing materials. In this study, we designed a novel microwave absorbing material by incorporating manganese into an apatite structure with adjustable chemical composition. The material $Mn_2Gd_{7.5}Ce_{0.5}(SiO_4)_6O_2$, exhibiting specific microwave absorption properties, was synthesized using a high-temperature solid-phase method. The results indicate that at a sample thickness of 5 mm, the absorption frequency bandwidth below −10 dB within the 2–12 GHz range reaches 1.2 GHz, with a peak absorption of −21.78 dB. Additionally, smaller particles were prepared using the sol-gel method, achieving a peak absorption of −39.75 dB. The primary absorption mechanism for both particle types is attributed to magnetic loss. This work presents a new approach to designing microwave absorbing materials and significantly contributes to expanding the range of apatite-type materials.

Keywords: apatite structure; $Mn_2Gd_{7.5}Ce_{0.5}(SiO_4)_6O_2$; microwave absorption performance

1. Introduction

For a long time, due to the significant research value and importance of absorbing materials, researchers have made substantial progress through extensive exploration. In recent years, manganese-containing minerals, recognized for their excellent absorption properties, have drawn increasing attention from researchers [1,2]. Manganese (Mn) naturally occurs in three valence states—Mn^{2+}, Mn^{3+}, and Mn^{4+}—which can undergo redox reactions, allowing them to transform into one another [3]. Under natural conditions, the transformation between these valence states is slow and inefficient. However, under microwave irradiation, the conversion rate is significantly enhanced, which is a key reason manganese-containing minerals are applied in the field of microwave absorption [4,5]. Despite the advancements in traditional manganese-based absorbing materials, research has predominantly focused on ferrite with spinel structures, magnetoplumbite types, garnet, and perovskite structures [6]. These manganese-based absorbing materials typically exhibit relatively simple structures. To expand the research system and scope of microwave absorbing materials, the development of novel manganese-containing structures has become highly significant.

Simultaneously, researchers exploring new absorbing materials have turned their focus to the “treasure house of new materials”—Rare earth elements. Due to their unique electronic structure, interactions between electron spin and orbit, strong crystal

fields, magneto-optical effects, atomic magnetic moments, anisotropy, high magnetostrictive coefficients, and low-temperature magnetic ordering transitions, rare earth absorbing materials have broadened absorption peaks and bands, often surpassing existing theoretical limitations [7,8]. These materials have garnered significant attention for their promising applications. By combining manganese (particularly divalent manganese) with rare earth elements in the microwave absorption field, it is possible to create materials with excellent microwave absorption properties within certain crystal structures. For example, rare-earth manganese-based oxide (LSMO), a material formed from LaMnO doped with oxides such as SrO, possesses a cadmium ore structure and exhibits a giant magnetoresistance effect, making it highly suitable for the development of absorbing materials [9]. Similarly, $LaBaMnO_3$, with its perovskite-type structure, demonstrates microwave absorption properties across the 2–18 GHz range, serving as a multifunctional material for both microwave and infrared applications [10]. These materials also offer the potential for compatible camouflage in radar and infrared wave bands.

With this in mind, we focused on the apatite-structured compounds. One key advantage of the apatite structure is its highly flexible framework, which allows for a wide range of elemental substitutions, thereby offering greater control over the material's dielectric and magnetic properties. This tunability can lead to enhanced impedance matching and optimized absorption performance over a broader frequency range. For the typical apatite-structured $A_{10}[MO_4]_6O_2$, the A-site is typically occupied by divalent cations such as Ca^{2+}, Mg^{2+}, and Mn^{2+}, but rare earth ions like Eu^{2+} or alkali metal ions can also occupy this position due to isomorphic replacement [11]. Similarly, $[PO_4]^{3-}$ ions can be substituted by $[SiO_4]^{4-}$ or $[GeO_4]^{4-}$ anions under varying conditions. We therefore selected the compound $Mg_2Y_8(SiO_4)_6O_2$ with an apatite structure for substitution, using ions with appropriate radii and charges, specifically Mn^{2+}/Gd^{3+} and Mg^{2+}/Y^{3+}. After substitution, the compound $Mn_2Gd_8(SiO_4)_6O_2$ was obtained. The Mn^{2+} ions possess five unpaired electrons in their outermost layer, giving them five spin magnetic moments. This characteristic suggests that divalent manganese ions have strong theoretical microwave absorption performance. (Trivalent and tetravalent manganese ions also exhibit some microwave absorption properties.). The Mn^{2+}/Gd^{3+} cations occupy two distinct positions: one is a triple trigonal prism formed by nine oxygen atoms, and the other is an irregular pentagonal biconical polyhedron coordinated by seven oxygen atoms [12,13]. Leveraging this feature, we further incorporated Ce^{3+} ions, known for their excellent microwave absorption properties, into various cation sites to induce lattice distortion and enhance microwave absorption performance.

In this study, we report on two synthetic methods used to evaluate the microwave absorption performance of the novel apatite compound $Mn_2Gd_{7.5}Ce_{0.5}(SiO_4)_6O_2$. The crystal structure of $Mn_2Gd_{7.5}Ce_{0.5}(SiO_4)_6O_2$, synthesized using the high-temperature solid-phase method, is presented for the first time, along with its microwave absorption properties. Building on this, the compound was further synthesized using the sol-gel method, resulting in smaller particle sizes and enhanced microwave absorption performance. These findings demonstrate that this design of microwave absorbing material is both feasible and effective.

2. Experimental section

2.1. Synthesis of $Mn_2Gd_{7.5}Ce_{0.5}(SiO_4)_6O_2$

First, $Mn_2Gd_{7.5}Ce_{0.5}(SiO_4)_6O_2$ was synthesized using the conventional high-temperature solid-state method. All raw materials were of analytical grade and obtained from Xilong Chemical Co., Ltd. Manganese carbonate ($MnCO_3$, 4 mmol), gadolinium oxide (Gd_2O_3, 1.5 mmol), silicon dioxide (SiO_2, 1 mmol), and cerium oxide (CeO_2, 0.5 mmol g) were weighed according to their stoichiometric ratios. After thorough grinding in an agate mortar for 5 minutes, the ground mixture was placed in a crucible, buried in carbon, and then calcined in a muffle furnace at 1100 °C for 4 hours. Once sintering was completed and the sample was fully cooled, it was ground again in a mortar to obtain the final sample.

Second, the smaller-sized particles were prepared using the sol-gel method, with metal nitrates as raw materials and tetraethyl orthosilicate as the silicon source. The following amounts were weighed according to the stoichiometric ratio: manganese nitrate tetrahydrate (0.2 mmol), gadolinium nitrate hexahydrate (0.75 mmol), cerium nitrate hexahydrate (0.05 mmol), tetraethyl orthosilicate (0.6 mmol), and citric acid $C_6H_8O_7 \cdot H_2O$ (3.2 mmol). The mixture was stirred at 80 °C to form a wet gel, which was then dried at 120 °C for 12 hours to form a dry gel. The dry gel was then sintered at 800 °C for 10 hours to obtain a precursor, which was further sintered at 1200 °C for 5 hours to produce the final $Mn_2Gd_{7.5}Ce_{0.5}(SiO_4)_6O_2$ sample.

2.2. Materials characterization

Powder X-ray diffraction (XRD, D8 Advance diffractometer, Bruker Corporation, Germany; 40 kV and 40 mA; Cu Kα, λ = 0.15406 nm) was used for phase identification. The structural analysis employed step scanning (2 θ ranging from 3° to 130°) at a rate of 2.5 s per step, with a step size of 0.02°. To verify whether the valence state of manganese matched the design, X-ray Photoelectron Spectroscopy (XPS, Thermo Scientific) was conducted using monochromatic Al Kα irradiation (150 W). The binding energy (BE) scale was calibrated using the adventitious carbon (C 1s) core level, assigned at 284.6 eV. The morphologies of these samples were examined by a Hitachi SU4800 field-emission gun scanning electron microscope (SEM).

2.3. Microwave absorption performance measurements

The microwave absorption properties of $Mn_2Gd_{7.5}Ce_{0.5}(SiO_4)_6O_2$ were analyzed using a microwave network analyzer (N5244A, Agilent) in the 2 to 18 GHz frequency range, with the coaxial wire method in free space. The sample powder (25 wt%) was thoroughly mixed with molten wax (75 wt%), and the mixture was pressed into toroidal samples. The outer diameter of the samples was 7.00 mm, the inner diameter was 3.04 mm, and the thickness was 3 mm.

3. Result and discussions

3.1. Characterizations of materials

The material $Mn_2Gd_{7.5}Ce_{0.5}(SiO_4)_6O_2$ was successfully synthesized using both the high-temperature solid-phase method and the sol-gel method. To study the structure of the samples, the powder X-ray diffraction (XRD) was employed. In **Figure 1b**, the XRD pattern of the $Mn_2Gd_{7.5}Ce_{0.5}(SiO_4)_6O_2$ sample prepared via the high-temperature solid-phase method is presented. The crystal face indices corresponding to the diffraction peak positions at 21.765°, 22.842°, 25.879°, 28.126°, 28.966°, 31.773°, 32.172°, and 32.902° are (200), (111), (002), (102), (210), (211), (112), and (300), respectively. No new diffraction peaks were observed compared to the $Ca_2Gd_8(SiO_4)_6O_2$ standard card (JCPDS no. 28–0212), indicating that the sample retained the apatite structure, and no new phases appeared [14]. However, the diffraction peaks of the sample showed a shift to the right compared to the standard card. This shift is due to the smaller ionic radius of divalent manganese ions compared to calcium ions. When calcium ions are substituted by manganese ions, some lattice parameters decrease. Since d is inversely proportional to sin θ, and in the 2 θ range of 10° to 70°, sin θ increases monotonically, the higher the position of the characteristic peak, the smaller the d value [15]. Additionally, for the $Mn_2Gd_{7.5}Ce_{0.5}(SiO_4)_6O_2$ sample, the slight difference in atomic volume between the Ce atom and the Gd atom means that the prepared $Mn_2Gd_{7.5}Ce_{0.5}(SiO_4)_6O_2$ maintains the apatite structure. Similarly, the XRD analysis of the sample prepared by the sol-gel method (**Figure 1a**) showed the same matching diffraction peaks when compared with the standard card (JCPDS No. 28–0212), confirming that the sample also exhibits an apatite structure.

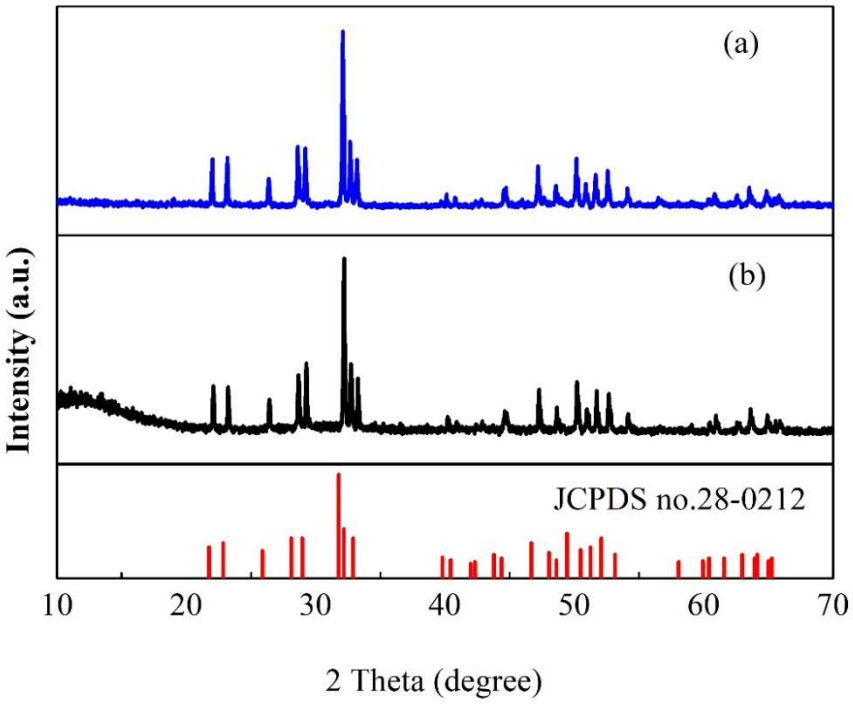

Figure 1. XRD patterns of. Mn2Gd7.5Ce0.5(SiO4)6O2 samples. **(a)** sol-gel synthesis of samples; **(b)** high temperature solid phase synthesis of samples.

The valence of manganese has a great influence on the microwave absorption properties of manganese-containing minerals due to the different number of electrons outside the nucleus, and the interactions between the different valence states also have

a certain influence on the microwave absorption properties of the materials [16,17]. In addition, due to the fact that rare earth element Ce is also a kind of variable element, the valence state of these two elements in the compound is necessarily a factor to be considered. The photoelectron survey spectrum of the $Mn_2Gd_{7.5}Ce_{0.5}(SiO_4)_6O_2$ sample is shown in **Figure 2**. The corresponding Mn element images are depicted in **Figure 2a,b**. Notably, two distinct broad peaks are observed in the $Mn_2Gd_{7.5}Ce_{0.5}(SiO_4)_6O_2$ sample, regardless of whether the sample was synthesized by the high-temperature solid-phase method or the sol-gel method. The wide survey scan of the XPS spectra revealed two peaks in the Mn 2p region at binding energies (BE) of 642.5 eV and 653.4 eV, corresponding to Mn $2p_{3/2}$ and Mn $2p_{1/2}$, respectively [18]. The BE difference (spin-orbit splitting) between the Mn $2p_{3/2}$ and Mn $2p_{1/2}$ peaks is 10.9 eV. Additionally, the fitted variance results, close to 1, suggest that Mn predominantly exists in the +2 oxidation state in the prepared samples. Meanwhile, the valence state of the cerium element on the sample surface corresponds to spin-orbit doublets characteristic of the +3 oxidation state (**Figure 2c,d**) [19].

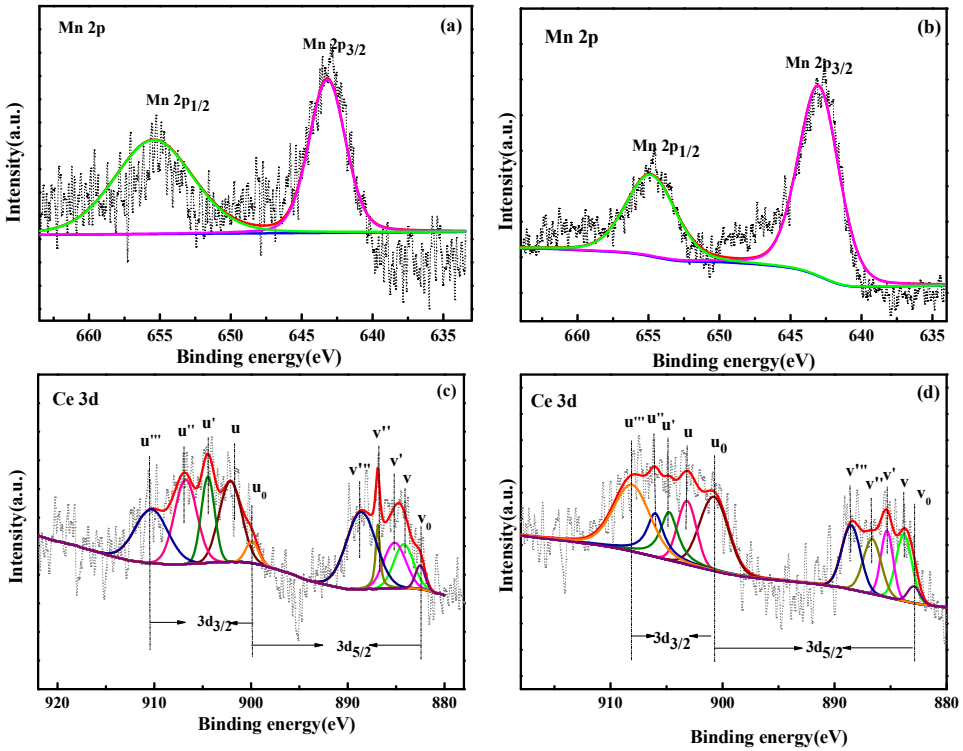

Figure 2. XPS spectra of $Mn_2Gd_{7.5}Ce_{0.5}(SiO_4)_6O_2$ samples. **(a)**, **(b)** Mn 2p of samples synthesized by high temperature solid phase method and sol-gel method; **(c)**, **(d)** Ce 3d of samples synthesized by high temperature solid phase method and sol-gel method.

The SEM images in **Figure 3a,b** show the microstructure of the samples synthesized by the high-temperature solid-state method and the sol-gel method, respectively. The particles of the sample prepared by the high-temperature solid-state method are larger and exhibit more significant agglomeration. In contrast, the sample synthesized by the sol-gel method shows a noticeable reduction in particle size, with less agglomeration. Larger particles tend to agglomerate, which prevents microwaves

from penetrating the material uniformly, thereby reducing the absorption performance. Smaller particles exhibit better dispersion, reducing agglomeration and increasing multiple scattering of microwaves within the material. This extends the propagation path of electromagnetic waves and increases the dissipation of electromagnetic energy, thereby improving microwave absorption efficiency [20].

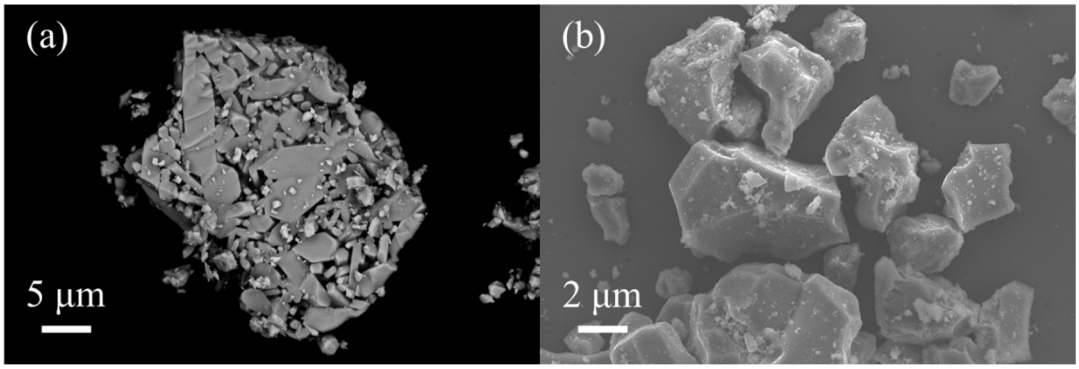

Figure 3. SEM images of the catalyst $Mn_2Gd_{7.5}Ce0.5(SiO_4)_6O_2$ samples, **(a)** high temperature solid phase synthesis; **(b)** sol-gel synthesis.

3.2. Microwave absorption performance measurements

To reveal the microwave absorption properties of the as synthesized samples, the reflection loss (RL) values of $Mn_2Gd_{7.5}Ce_{0.5}(SiO4)_6O_2$ samples were calculated using the relative complex permeability and permittivity at a given frequency and thickness layer according to the transmit line theory, which is summarized as the following equations [21]:

$$RL\ (dB) = 20 \log | (Z_{in} - Z_0)/(Z_{in} + Z_0) | \quad (1)$$

where Z_{in} and Z_0 represent the input impedance of the absorber and the impedance of free space. The absorber impedance can be calculated from the following equation [22]:

$$Z_{in} = Z_0(\mu_r/\varepsilon_r)^{1/2}\tan h\ [j\ (2\pi fd/c)\ (\mu_r\varepsilon_r)^{1/2}] \quad (2)$$

where ε_r and μ_r represent the relative complex permittivity and the relative complex permeability, respectively; f stands for the frequency; d is the thickness of toroidal shaped sample and c is the velocity of electromagnetic waves in free space. The relative complex permeability and permittivity were tested on a network analyzer with the frequency of a 2–12 GHz range.

The thickness of the sample is one of the crucial parameters that affects the intensity and position of the frequency at the RL minimum. To eliminate the influence of sample thickness, we prepared two sets of samples with thicknesses of 2, 3, 4, 5, and 6 mm. **Figure 4** illustrates the relationship between microwave reflectivity and frequency for the sample $Mn_2Gd_{7.5}Ce_{0.5}(SiO_4)_6O_2$, synthesized using the high-temperature solid-phase method and measured with vector network analysis under varying thicknesses. The data in **Figure 4a** reveals that when the sample thickness is 5 mm, the maximum absorption peak is −21.78 dB at a frequency of 5.2 GHz, with an effective microwave absorption bandwidth of 0.62 GHz. This figure clearly indicates that the intensity of microwave absorption is closely related to the thickness of the

sample. According to microwave absorption theory, sample thickness is generally proportional to microwave absorption ability; thus, within a certain range, greater thickness results in enhanced microwave absorption performance [23]. It is important to note that this relationship holds only within a specific range of sample thickness. For a wave-absorbing material, when the matching frequency exceeds the cutoff frequency, a matching thickness is established [24]:

$$t_m = c/(2\pi s_0) \quad (3)$$

where $s_0 = \mu * f_c$ (c is the light velocity, f_c is the relaxation frequency, μ_i is the initial permeability) matching thickness is only related to the performance parameter s_o of the material. When the thickness is lower than or higher than the matching thickness, the absorption coefficient of the material decreases.

The grain size of the sample is another crucial parameter that affects the microwave absorption properties of materials. Therefore, we prepared smaller samples using the sol-gel method to enhance these properties. For the samples synthesized via the sol-gel method, the same calculation method was employed. The results in **Figure 4b** indicate that the frequency position at the RL minimum shifts from higher to lower as the thickness increases, which is associated with quarter-wavelength attenuation. When the sample thickness is 6 mm, the maximum absorption peak rises to 39.75 dB at a frequency of 5.2 GHz, with an effective microwave absorption bandwidth of 0.62 GHz. This is due to the smaller grain size of the samples prepared by the sol-gel method compared to those obtained using the solid-phase method. This difference results in altered impedance matching conditions for the sample, leading to maximum microwave reflection loss at 6 mm. Additionally, the smaller size of the samples results in a larger specific surface area, more surface atoms, and more dangling bonds, which contribute to stronger interfacial polarization and increased multiple scattering.

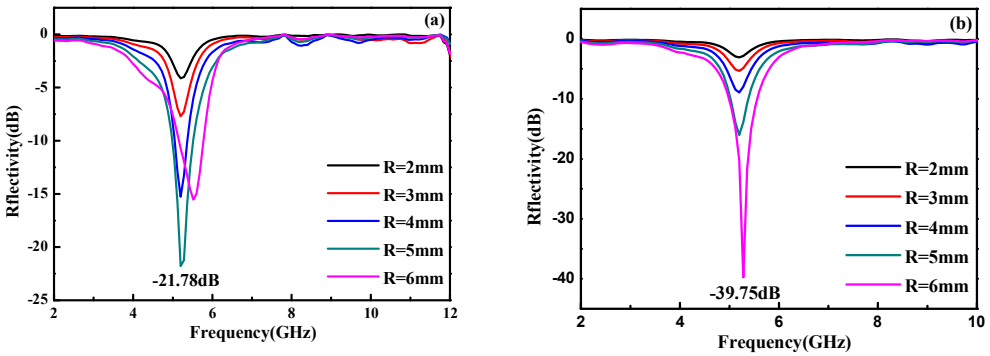

Figure 4. Frequency and microwave reflection losses for different thicknesses of $Mn_2Gd_{7.5}Ce_{0.5}(SiO_4)_6O_2$ compounds: **(a)** high temperature solid phase synthesis of samples; **(b)** sol-gel synthesis of samples.

As is well known, the synergy between the complex relative dielectric constant and permeability of a sample affects the minimum reflection loss (RL) mechanism of the material. When the dielectric constant is dominant, the reflection loss mechanism is primarily governed by dielectric loss, and the opposite is true when permeability dominates. The imaginary components of permittivity (ε″) and permeability (μ″)

indicate the material's energy dissipation capability, while the real components represent its ability to store electric (ε′) and magnetic (μ′) energy. **Figure 5** presents the complex dielectric constant, complex permeability, and tangential loss of our synthesized compounds combined with paraffin (in a 3:1 mass ratio) over a frequency range of 2 to 12 GHz. The samples were synthesized by the solid-phase method, as shown in **Figure 5a**. The real and imaginary parts of the composite dielectric constant $Mn_2Gd_{7.5}Ce_{0.5}(SiO_4)_6O_2$ increase slightly with frequency, showing no significant change in the overall composite dielectric constant. This indicates that the material exhibits no or only weak dielectric loss under the influence of a microwave alternating electric field. **Figure 5b** shows the relationship between magnetic permeability and frequency for the $Mn_2Gd_{7.5}Ce_{0.5}(SiO_4)_6O_2$. It can be observed that as the frequency increases, the real part of the magnetic permeability decreases significantly within the 4.8 GHz to 5.5 GHz range. The imaginary part of the magnetic permeability in **Figure 5b** also exhibits a sharp peak between 4.8 GHz and 5.5 GHz. This behavior, considering the trends of both μ′ and μ″, corresponds to domain resonance within this frequency range, while the remainder of the range corresponds to the relaxation spectrum. This frequency range aligns with the microwave absorption bandwidth and the frequency corresponding to the material's maximum microwave absorption peak. The observed magnetic tangent loss reaches up to 2.12 at 5.36 GHz (**Figure 5c**) and remains higher than the dielectric tangent loss across the entire frequency range, indicating that magnetic loss is the major contributor to electromagnetic loss.

The complex relative permittivity and permeability of the sample synthesized by the sol-gel method are shown in **Figure 5d–f**. The real part of the composite dielectric constant of $Mn_2Gd_{7.5}Ce_{0.5}(SiO_4)_6O_2$ slightly decreases with increasing frequency, while the imaginary part remains unchanged, indicating that the material will experience weak dielectric loss under the influence of a microwave alternating electric field. This suggests that dielectric loss is not a key factor in the microwave absorption properties of the material [25]. **Figure 5e** shows the relationship between magnetic permeability and frequency for the $Mn_2Gd_{7.5}Ce_{0.5}(SiO_4)_6O_2$. The figure shows that as frequency increases, the real part of the magnetic permeability first decreases and then increases, while the imaginary part exhibits the opposite trend. This observation is similar to the conclusion drawn from **Figure 5b**. However, the real and imaginary parts of the complex permeability (μ′, μ″) of the sample synthesized by the sol-gel method exhibit more fluctuations compared to those synthesized by the solid-phase method. This is because a decrease in particle size changes the resonance frequency of the particles, increasing both the absorption frequency and intensity. The tangent loss of $Mn_2Gd_{7.5}Ce_{0.5}(SiO_4)_6O_2$ composites in **Figure 5f** supports the same result as in **Figure 5c**, with magnetic loss still making the major contribution to electromagnetic loss.

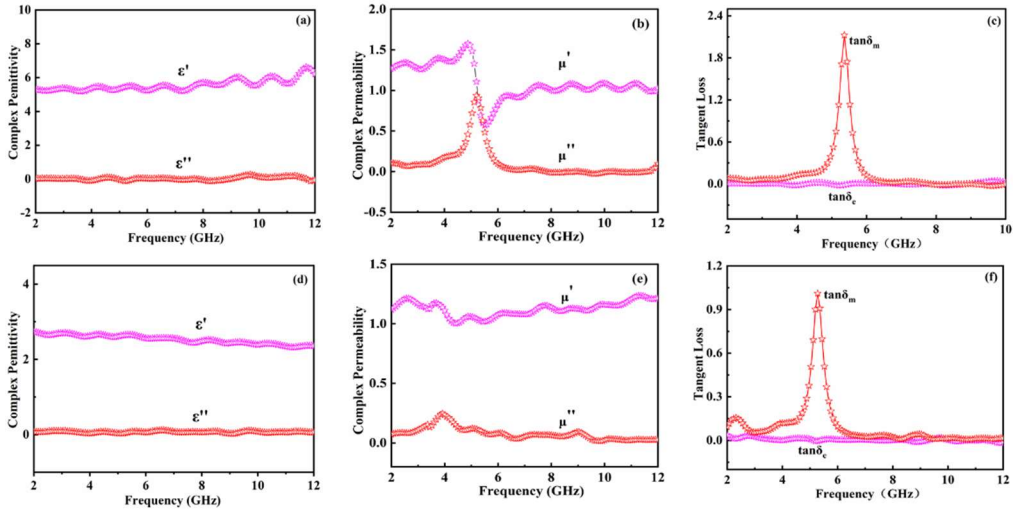

Figure 5. (a) Complex permittivity; **(b)** complex permeability; **(c)** tangent loss of high temperature solid phase synthesis of composites; **(d)** complex permittivity; **(e)** complex permeability; **(f)** tangent loss of Sol-gel synthesis of composites.

4. Conclusion

Microwave-absorbing materials with an apatite structure were successfully synthesized using both high-temperature solid-phase and sol-gel methods. The prepared samples exhibited notable microwave absorption properties, with particle sizes obtained from different preparation methods playing a crucial role in determining the microwave absorption bandwidth and depth. The microwave absorption properties of the material are primarily attributed to magnetic losses. This study provides a new perspective on the application of structural adjustment and the microwave absorption characteristics of apatite materials. The structural design of microwave-absorbing materials with rich properties and the research on apatite-structured materials in the field of microwave absorption hold significant research value and promising prospects.

Author contributions: Conceptualization, HL and LM; methodology, HL and NL; software, NL; validation, HL, XL and LM; formal analysis, NL; investigation, HL; resources, HL; data curation, NL; writing—original draft preparation, HL; writing—review and editing, NL; visualization, XL; supervision, HL; project administration, LM; funding acquisition, HL and LM. All authors have read and agreed to the published version of the manuscript.

Conflict of interest: The authors declare no conflict of interest.

References

1. Lan D, Li H, Wang M, et al. Recent advances in construction strategies and multifunctional properties of flexible electromagnetic wave absorbing materials. Materials Research Bulletin. 2023; 112630.
2. Wang D, Jin J, Guo Y, et al. Lightweight waterproof magnetic carbon foam for multifunctional electromagnetic wave absorbing material. Carbon. 2023; 202: 464–474.
3. Hu J, Liu S, Wang Y, et al. Manganese phosphate coated flaky FeSiAl powders with enhanced microwave absorbing properties and improved corrosion resistance. Materials Chemistry and Physics. 2023; 296: 127274.

4. Yang Z, Yu Z, Xu Z, et al. Molten salt-directed synthesis of carbon nanotube/C_3N_4/manganese carbodiimide (MnNCN): Novel microwave absorbing materials. Materials Research Bulletin. 2024; 175: 112757.
5. Jin L, Chen J, Zhang L, et al. Coupling dielectric and magnetic components on a ternary composite for enhancing impedance matching and microwave absorption. Ceramics International. 2024.
6. Vinnik DA, Gudkova SA, Zhivulin VE, et al. Ferrite-based solid solutions: structure types, preparation, properties, and potential applications. Inorganic Materials. 2021; 57: 1109–1118.
7. Deng Y, Wang L, Liu W, et al. Research Progress on Controllable Absorption Properties of Rare Earth Element Doped Electromagnetic Wave Absorbing Materials. Chinese Journal of Chemistry. 2024.
8. Chen Z, Li Z, Chen J, et al. Recent advances in selective separation technologies of rare earth elements: A review. Journal of Environmental Chemical Engineering. 2022; 10(1): 107104.
9. Guo J, Jing Y, Shen T, et al. Effect of doped strontium on catalytic properties of $La_{1-x}Sr_xMnO_3$ for rhodamine B degradation. Journal of Rare Earths. 2021; 39(11): 1362–1369.
10. Munazat DR, Kurniawan B, Kurita N, et al. Investigation of the impact of A-site cation disorder on the structure, magnetic properties, and magnetic entropy change of trisubstituted divalent ions in $La_{0.7}(Ba, Ca, Sr)_{0.3}MnO_3$ manganite. Physical Chemistry Chemical Physics. 2024; 26(26): 18343–18367.
11. Liu H, Liao L, Pan X, et al. Recent research progress of luminescent materials with apatite structure: a review. Open Ceramics. 2022; 10: 100251.
12. Jing XD, Li ZG, Chen ZT, et al. Effect of praseodymium valence change on the structure, magnetic, and microwave absorbing properties of M-type strontium ferrite: the mechanism of influence of citric acid dosage and calcination temperature. Materials Today Chemistry. 2023; 30: 101537.
13. Khanvilkar MB, Nikumbh AK, Pawar RA, et al. Effect of divalent/trivalent doping on structural, electrical and magnetic properties of spinel ferrite nanoparticles. Engineered Science. 2023; 22: 850.
14. Fu J, Liu N, Mei L, et al. Synthesis of Ce-doped $Mn_3Gd_{7-x}Ce_x(SiO_4)_6O_{1.5}$ for the enhanced catalytic ozonation of tetracycline. Scientific Reports. 2019; 9(1): 18734.
15. Gupta I, Singh D, Singh S, et al. Study of structural and spectroscopic characteristics of novel color tunable yellowish-white Dy^{3+} doped $Gd_4Al_2O_9$ nanophosphors for NUV-based WLEDs. Journal of Molecular Structure. 2023; 1272: 134199.
16. Tian F, Gao Y, Wang A, et al. Effect of Mn substitution on structural, magnetic and microwave absorption properties of Co_2Y hexagonal ferrite. Journal of Magnetism and Magnetic Materials. 2023; 587: 171229.
17. Yue J, Cheng L, Xiong J, et al. Effect of neodymium doping on structure, magnetic properties and microwave absorption performance of $SrMnO_3$. Journal of Rare Earths. 2024; 42(2): 354–363.
18. Yin Y, Yan S, Ni Z, et al. Economical synthesized Mn_3O_4/biomass-derived carbon from vegetable sponge composites and its excellent supercapacitive behavior. Biomass Conversion and Biorefinery. 2023; 13(13): 12115–12124.
19. Dhandapani P, Nayak PK, Maruthapillai A. Improved electrochemical performance and charge storage mechanism of $NiMnCoO_4$ by XPS study. Materials Chemistry and Physics. 2023; 297: 127287.
20. Zheng Q, Yu M, Wang W, et al. Enhanced microwave absorption performance of Fe/C nanofibers by adjusting the magnetic particle size using different electrospinning solvents. Ceramics International. 2020; 46(18): 28603–28612.
21. Quan B, Gu W, Sheng J, et al. From intrinsic dielectric loss to geometry patterns: Dual-principles strategy for ultrabroad band microwave absorption. Nano Research. 2021; 14: 1495–1501.
22. Lei C, Du Y. Tunable dielectric loss to enhance microwave absorption properties of flakey FeSiAl/ferrite composites. Journal of Alloys and Compounds. 2020; 822: 153674.
23. Elmahaishi MF, Ismail I, Muhammad FD. A review on electromagnetic microwave absorption properties: their materials and performance. Journal of Materials Research and Technology. 2022; 20: 2188–2220.
24. Yang SJ, Park KT, Im J, et al. Ultrafast 27 GHz cutoff frequency in vertical WSe_2 Schottky diodes with extremely low contact resistance. Nature communications. 2020; 11(1): 1574.
25. Wang F, Liu Y, Zhao H, et al. Controllable seeding of nitrogen-doped carbon nanotubes on three-dimensional Co/C foam for enhanced dielectric loss and microwave absorption characteristics. Chemical Engineering Journal. 2022; 450: 138160.

Materials Technology Reports 2024, 2(2), 1813.
https://doi.org/10.59400/mtr1813

Article

Study on the influence of aluminium nitride particulates on the dry sliding wear behavior and mechanical properties of aluminium 6061 alloy developed using stir casting method

Raghavendra Subramanya[1,*], Manjunatha Kuntanahalli Narayanappa[2], Nagesh Devareddy[3], Madusudhana Shettykothanuru Vemanna[4], Ravikumar Mukundaiah[5], Chandra Shekar Anjinappa[6], Thyagaraj Narasapura Rajanna[2], Arun Kumar Rudrappa[7]

[1] Department of Mechanical Engineering, Sai Vidya Institute of Technology, Bangalore 560064, India
[2] Department of Mechanical Engineering, Sri Jagadguru Chandrashekaranatha Swamiji Institute of Technology, Chickballapura 562101, India
[3] Department of Aeronautical Engineering, Sri Jagadguru Chandrashekaranatha Swamiji Institute of Technology, Chikaballpura 562101, India
[4] Department of Aerospace Engineering, Sri Jagadguru Chandrashekaranatha Swamiji Institute of Technology, Chikaballpura 562101, India
[5] Department of Mechanical Engineering, B.M.S College of Engineering, Bangalore 560019, India
[6] Department of Robotics and Artificial Intelligence Engineering, Bangalore Institute of Technology, Bangalore 560004, India
[7] Department of Mathematics, Sai Vidya Institute of Technology, Bangalore 560064, India
*** Corresponding author:** Subramanya Raghavendra, rvs.sdly@gmail.com

CITATION

Subramanya R, Kuntanahalli Narayanappa M, Devareddy N, et al. Study on the influence of aluminium nitride particulates on the dry sliding wear behavior and mechanical properties of aluminium 6061 alloy developed using stir casting method. Materials Technology Reports. 2024; 2(2): 1813. https://doi.org/10.59400/mtr1813

ARTICLE INFO

Received: 30 September 2024
Accepted: 19 November 2024
Available online: 22 November 2024

Abstract: Aluminium matrix composites (AMCs) reinforced with hard ceramic particles is currently being widely used as a composite material for a range of industrial and technical applications. In the current study, melt stirring was employed to incorporate Aluminium nitride (AlN) particulates into the aluminium 6061 alloy. In this study AlN particles in different proportions 2%, 4%, 6%, and 8% wt were used with Al6061 alloy. Scanning electron microscopy (SEM) and x-ray diffraction were used to characterise the stir cast composites and the base alloy. SEM analysis confirmed the uniform distribution of AlN particles within the Al matrix. The impact of AlN concentrations on the mechanical properties of Al6061 matrix composites was investigated. Pin on disc machines were utilised to examine the dry sliding wear properties of the composites that were manufactured. The presence of very hard AlN elements in the Al6061 matrix alloy significantly improved the mechanical and wear characteristics of the AMCs. As compared to the Al6061 base alloy, the test results showed that the Al6061 with 8% weight percentage AlN composites had better wear resistance and hardness yield strength and the alloy with 2% AlN showed highest tensile strength of 368 MPa. The good interfacial adhesion between fillers and matrix prevents cracking and allows for effective load transmission to the reinforcing phase. This is mainly because AlN is a highly strong and stiff material, and its incorporation gives strong reinforcement as well as increased tensile, flexural, and hardness strength to the composite. This enhancement in mechanical properties suggests potential applications in high-wear industries such as automotive and aerospace.

Keywords: aluminium nitride; stir casting; wear analysis; tensile; flexural

1. Introduction

In modern engineering applications, especially in aerospace and automotive industries, materials with enhanced mechanical and wear properties are in high demand. Aluminium matrix composites (AMCs) offer tuneable mechanical and physical properties, making them suitable for various engineering applications. These applications include aerospace automobile components such turbine blades, engine parts, and wings [1,2]. Furthermore, AMCs have a wide range of uses in the

automotive sector, including synchronizers, brake drums, piston rings, and many more [3,4]. It is well known that the final desired properties of the manufactured AMMCs have a significant influence on the reinforcement selection process, the type and proportion of reinforcement determine the composite's strength, hardness, and wear resistance.

Researchers consistently choose the use of particle and fiber reinforcements in composites because of their ability to give the metal matrix great strength, toughness, wear resistance, and fatigue resistance [5]. Particles, due to their ability to disperse uniformly within the matrix, often provide superior strength and toughness compared to fibers. However, due of their ease in fabrication and cheap modelling cost when compared to other reinforcements, research have concentrated more on investigating particle-based reinforcements.

Due to its multiple applications in fields such as semiconductors, electronics, aircraft, and corrosive chemical handling vessels, aluminium nitride (AlN) coating has garnered significant attention [6,7]. AlN has a wide range of applications due to its high hardness, high electrical resistivity, low coefficient of thermal expansion, outstanding physical and chemical stability—even at quite high temperatures—and great resistance to wear, abrasion, and corrosion. These properties make AlN an ideal candidate for reinforcement in AMCs, which this study aims to explore.

Sager et al. [8] examined the application of AlN particles as reinforcement in metal matrix composites and the way they affected the corrosion behaviour of the materials. The findings indicate that adding AlN reduces grain sizes and improves the matrix materials' resilience to corrosion [8]. The behaviour of stir-cast AlN reinforced AA7075 composites were elucidated by Mohanavel et al. [9]. They discovered that flexural strength, UTS, and hardness improved significantly with an increase in the weight percentage of AlN. Furthermore, it was clear from the SEM study that the particles were equally dispersed throughout the composites [9]. However, while their work focused on AA7075, the behavior of Al6061 composites remains underexplored, particularly with varying AlN concentrations. After examining the behaviour of AlN-filled Al composites, Min Zhao et al. [10]. came to the conclusion that the strong interfacial interaction between AlN and Al matrix was the reason for the significant rise in UTS [10].

The Al-AlN composites were fabricated by Lii et al. [11], and the results showed that the addition of AlN reinforcement significantly increased the composites' compressive strength, hardness, and fracture strength [12]. The addition of AlN content to magnesium alloy considerably enhanced its mechanical properties, such as yield strength, UTS, and plasticity, as reported by Khrustalyov et al. [13]. The impact of Al_2O_3 reinforcement on the wear-resistance (WR) of AA6061 and its composites reinforced with 10 vol% Al_2O_3 was documented by Pramanik et al. [14]. After undergoing direct chill casting, both aluminium alloy and composites were hot-extruded into bars. Results indicated that WR was greater in AA6061/Al_2O_3 composites than in base alloy.

Utilising the stir casting method, Pazhouhanfar and Eghbali [13] developed the AA2024 matrix composite reinforced with Al_2O_3 particles of different sizes, namely 16, 32, and 66 μm. The smaller particles (16 and 32 μm) led to agglomeration and segregation of the particles and porosity, whereas the coarser size (66 μm) had a

more uniform dispersion. The Al dendrites' early solidification during the composite's solidification was warranted. As the number of Al_2O_3 particles present grew and the particle size decreased, so did the tensile strength and hardness.

Tribological properties of aluminium 6061 alloy reinforced with hybrid composites of graphite and boron particles have been investigated by Nagesh et al. The Al6061 alloy is melted in a graphite crucible in an electrical furnace at a temperature of 720 ℃. In order to eliminate gases and prevent a temperature decrease during casting, the boron and graphite particles are warmed to 600 ℃. When the samples were put through a wear test, the hybrid composite outperformed mono composites in terms of wear resistance under the specified conditions [15].

Kumar et al. [16], carried out research on composites made of Al6061-SiC and Al7075-Al_2O_3. The liquid metallurgy method is used to create the composites, and 2–6% of the particles are distributed throughout the basic matrix. As the amount of filler in the composites grew, the microhardness of the Al6061-SiC and Al7075-Al_2O_3 composites rose as well, reaching 60-97VHN and 80-109VHN, respectively. Al6061-SiC composites have better tensile strength qualities than Al7075-Al_2O_3 composites, and the composites' tensile strength properties are found to be greater than those of the basic matrix. The composites had greater wear resistance, and SiC also made a substantial contribution to the Al6061-SiC composites' increased wear resistance.

The literature study that is quoted clarifies the important role that ceramic reinforcement—specifically, nitrides and Al_20_3—plays in aluminium-based composites. When this reinforcement is included into materials based on aluminium, it produces a strengthening effect that makes the composite material more resilient to deformation and failure. Reinforcement particles alter the material's behaviour by improving its mechanical characteristics, making it more suitable for a variety of situations needing increased strength.

Building upon these insights, the present study explores the effect of varying AlN concentrations in Al6061 composites. In particular, the application of aluminium nitride as reinforcements in casting-synthesised aluminium matrix composites is not as well documented. However, there is still limited research on the effects of AlN on the microstructural, mechanical, and tribological properties of Al6061 composites. This study aims to fill that gap by investigating the behavior of Al6061 composites with varying AlN content. Ultimately, this study aims to create and analyze Al6061 composites reinforced with AlN, focusing on optimizing their wear resistance, hardness, and compressive strength. Squeeze casting was used to precisely create Al6061 matrix composite enhanced with AlN in order to accomplish this challenging goal.

2. Materials and methods

The alloys for the investigation were produced using stir casting technique. Electric Furnace make VM10L1200 was used for the melting and casting procedures, aluminium alloy 6061 (AA6061) used as the base matrix alloy. Melting was carried out at 800 ℃ in a heat-resistant steel crucible. The graphite blade spinning at 400 rpm was used to agitate the molten metal for ten minutes when AlN

reinforcing particles (density 3.26 g/cm^3) of average diameter 10 µm were introduced. The blade was adjusted horizontally and vertically throughout the process to ensure even particle distribution and prevent dead zones in the melt. After that, samples were prepared in accordance with ASTM standards by pouring the molten composite into a cylindrical steel mould, which was preheated to 250^{0}C to avoid thermal shock and ensure a uniform cooling rate during solidification. The cast alloys produced had nominal percentages of 0%, 2%, 4%, and 6% AlN. ASTM-E8 standards were used to produce the tensile samples, ASTM-E10 standards were used for the hardness test, ASTM-E23 standards were used for the flexural test, and ASTM-G99-95 standards were used for the wear samples. The chemical compositions of Al6061 are shown in **Table 1**.

Table 1. Chemical composition of Al6061 and AlN.

Al6061	Elements	Cr	Cu	Mg	Zn	Fe	Mn	Si	Ti	Al
	Actual value %	0.35	0.40	1.20	0.25	0.70	0.15	0.80	0.15	95.85
AlN	Elements	O	N	Al						
	Actual value %	1.46	32.26	66.28						

2.1. X-ray diffraction analysis of Al6061 and AlN

X-ray diffraction assessment was achieved to evaluate the occurrence of Al and AlN reinforcement in the composite. XRD spectrum exhibits the occurrence of dual peaks related to Al6061 and AlN which are depicted in the **Figure 1**. XRD data obtained using a Cu-Ka source (wavelength of 0.1540598 nm) X-ray.

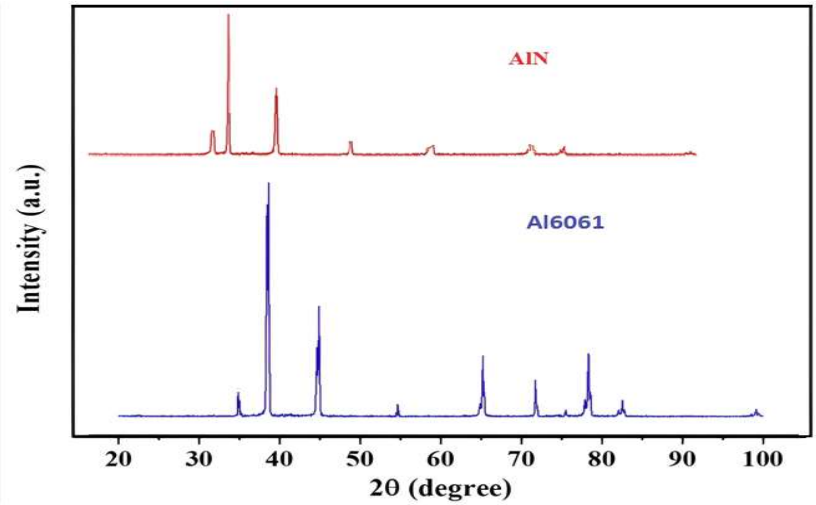

Figure 1. XRD peaks of A6061 and A1N.

Figure 1 shows the XRD pattern of sputtered AlN. The main peaks of the aluminium nitride are observed at Bragg's as 33.3°, 36.0°, 37.5°, and 42.6° corresponding to the crystallographic planes (100), (002), (101), and (220), respectively. The highest peak intensity was found for AlN with (002) orientation. A comparison of observed and standard values of the work investigated by Park and Kim [17]. The XRD showed the compounds present in the aged composites.

Aluminium having the highest peak, Mg and Si elements was present, confirming that it is a 6061 aluminium alloy.

2.2. Tensile, hardness and flexural strength

In the current study, prepared specimens were subjected to a tensile test on a universal testing machine (UTM), the samples were prepared using ASTM-E8 standards. Tensile tests were carried out on KIC-2-1000c machine, and at a test speed of 1 mm/min.

According to the results of the tensile tests as shown in **Figure 2**, the ultimate tensile strength of the alloy increases as the AlN weight percentage rises. Adding ceramic reinforcing AlN functions as a nucleation site and facilitates the crystallisation of the aluminium matrix in the AA6061 matrix. The dislocation motion of aluminium composites is robustly mediated by the improvised grain boundaries. Grain size has decreased as a result of the confined dislocations that are constantly moving across the matrix. This prevents the dislocation motion that builds up the composites' strengthening effect. This reduction in grain size impedes dislocation movement, thereby strengthening the composite. The spatial arrangement of reinforcement in the matrix alloy and the grain refinement seen in the microstructure are the reasons for the rise in hardness of composites. When compared to aluminium alloy, it is also discovered that the increased weight % of AlN acts as a constraint to resist the motion of dislocation, producing a higher hardness. The higher concentration of AlN particles creates more obstacles for dislocation movement, resulting in an increase in hardness.

The flexural test was also conducted on KIC-2-1000c UTM machine with cross head speed of 2 mm/min, the specimen was fabricated as per ASTM E23 standard, Similar trend is observed flexural test also (**Figure 2**), the alloy flexural strength increased as the AlN wt% increases. One of the main factors lowering the ductility is the ceramic-reinforced particles' brittle behaviour. The ductile matrix content can be decreased by increasing the weight percentage of AlN particles in the composites, which can counteract the aluminium matrix's capacity to flow. The flexural strength is calculated using Equation (1).

$$\sigma = (M/I)Y \tag{1}$$

where

σ: Bending stress

I: Moment of inertia

M: Bending Moment

Y: Young's Modulus

Arık et al. [18] studied the mechanical characteristics of B4C-reinforced MMCs with an Alumix-13 matrix, generated using hot compaction. They tested the hardness and three-point bending strength of the aged and non-aged composites. According to the results of the researchers' three-point bending tests, the B4C reinforcement material significantly increased the three-point bending strength of the powder metallurgical composite materials, while the composites containing 10% B4C decreased in strength. As a cause for this finding, they proposed that the increased tendency of fracture formation with the higher B4C ratio restricted the deformation

during the three-point bending test and most likely demonstrated a trend towards a cleavage fracture.

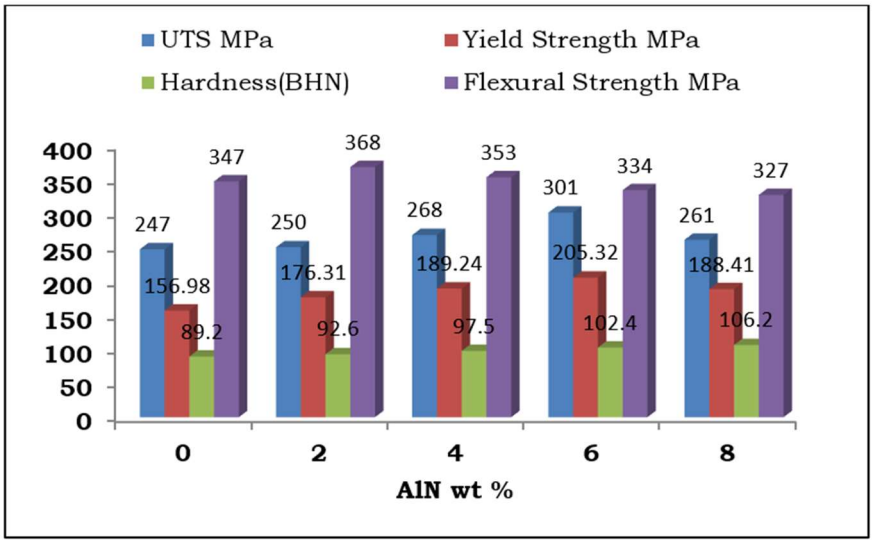

Figure 2. Tensile strength, hardness strength and flexural strength of AlN reinforced Al6061 alloy.

The hardness experiment was conducted using a main load of 100 kgf on a Rockwell hardness testing equipment, with the B scale selected. The specimen with 0% weight AlN had a hardness of 89.2 BHN; linear increases in hardness were achieved by adding 2%, 4%, and 6% weight AlN. The highest BHN recorded in 8% wt reinforced specimens was 106.2. These increases have been identified for enriching the weight proportion of the hard and brittle modes of the AlN particles in the Al6061 aluminium alloy. In a similar work, Hillary et al.'s [19] study examined the mechanical behaviour of Al6061 with silicon carbide (SiC) and titanium diboride (TiB_2) composites. The composite was made with 5 wt% SiC and 2/8 wt% TiB_2 using the traditional stir casting technique. The experiment's results demonstrated increases in micro hardness, tensile strength, and flexural strength of 8.18%, 20.19%, and 9.46%, respectively. Hard particles like SiC and TiB_2 boosted the hybrid composite's load-bearing capacity, which enhanced the mechanical performance of the as-cast Al-6061 composite.

This might be related to an increase in the quantity of hard ALN particles in the aluminium matrix, as well as their high hardness. The incorporation of reinforcement particles into the aluminium matrix increases their surface area while decreasing the size of the aluminium matrix grains. The presence of these hard surface regions on ALN particles provides significant resistance to plastic deformation, resulting in increased hardness of manufactured AMCs [20]. Furthermore, the presence of hard and brittle ALN particles in the soft and ductile Al6061 matrix decreases the ductility content of fabricated AMCs due to the low ductile content of matrix metal in the composite, which significantly improves the hardness of manufactured AMCs, the same phenomena were observed in the obtained result as shown in **Figure 2**.

The dispersion of the strengthening phase and bonding strength of ALN particles in the matrix significantly impact the ultimate tensile strength. This is a well-known dispersion-strengthening mechanism. As a result, the observed

undesirable decrease in ultimate tensile strength is mostly due to the creation of small AlN agglomerations inside the matrix. These AlN agglomerations often decrease the interfacial area between the reinforcement and the matrix. Furthermore, the existence of pores within the matrix caused by the overlapping of the AlN particles has a detrimental influence on the material's strength, resulting in fracture initiation in the composite under loading. This reduces interfacial energy bonding between reinforcement and matrix particles, this leads to reduce in the strength of the composites [21].

3. Wear analysis

Dry sliding tests were chosen to simulate real-world conditions where lubrication might be absent, such as in high-temperature environments. The wear test was performed with a 'Pin-on-Disc' wear testing equipment, using specimens with a diameter of 6 mm and a length of 40 mm, a dry sliding wear test was performed in accordance with ASTM-G99-95 standard, against a revolving EN32 steel disc with a hardness of 65 Rc. Testing was conducted using a Pin on-Disc wear test machine (Make: Ducom Instruments Pvt. Ltd., Model: TR20LE), whereby wear and tangential frictional force were tracked with the use of electronic sensors.

The parameters for tribological experiments include load 20 N, 40 N, and 60 N, as well as sliding velocity 1.5 m/s at intervals of 0.5. **Figure 3**, displays the results of the wear tests conducted on the produced composites and illustrates the relationship between the particular wear rate and the quantity of reinforcement in terms of sliding distance and applied load. The wear rates of all the alloy samples are clearly lower than those of the Al6061 alloy, as shown in **Figure 3**. The composite with 8 weight percent AlN has the lowest wear rate, the wear resistance of the 8 wt% AlN composites can be attributed to the uniform distribution of hard AlN particles that resist surface deformation and material removal during sliding. There are several reasons for the increased wear rate in the Al6061 alloy, including the presence of reinforced AlN, the uniform distribution of the reinforcement, the interfacial bonding between the reinforcement and matrix material, and the increased strength attained by

Smaller grains prevent dislocations from moving and lessen the likelihood that a fracture will spread, which is why this happens. AlN, on the other hand, is usually stronger and harder than the matrix material. These hard particles can withstand wear and distortion when included into a softer matrix, hence boosting the composite's overall hardness and wear resistance. Ensuring a consistent distribution of AlN inside the aluminium matrix enhances the composite's resilience to wear. This uniform distribution contributes to the development of a microstructure with several hard phases, which can lessen friction and stop wear tracks from forming.

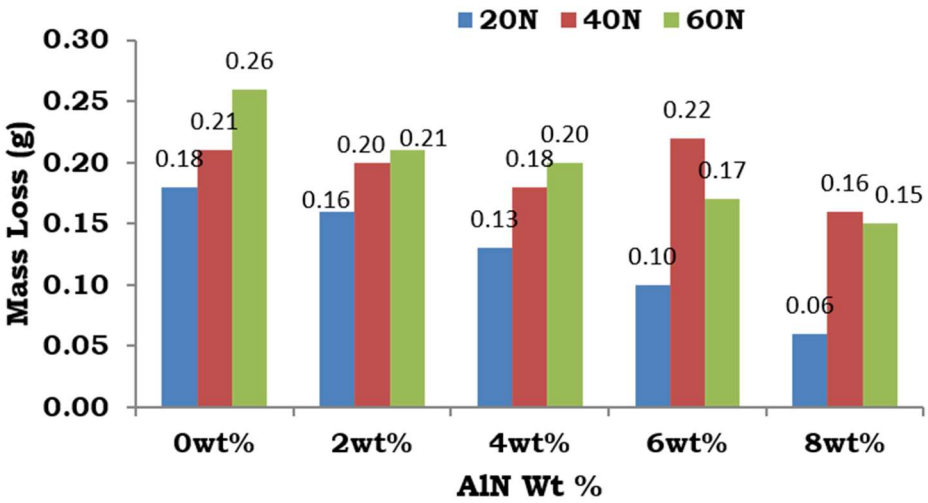

Figure 3. Mass loss of AlN reinforced Al6061 alloys at 20 N, 40 N and 60 N load conditions.

The impact of AlN weight percentage on wear weight loss during the wear test under various load circumstances, such as 20 N, 40 N, and 60 N, is shown in **Figure 4**. The weight loss is calculated using Equation (2).

$$\text{Weight loss(gm)} = \frac{\text{intial weight} - \text{final weight}}{\text{intial weight}} \quad (2)$$

The AlN composites with 8 weight percent reinforcement had the lowest mass loss, whereas the Al6061 matrices had the highest mass loss. It is evident that hard Nano AlN particles reinforced with Al6061 matrix result in a significant increase in mass loss.

The relationship between the rise in wear rate seen in both the Al6061 alloy and the AlN reinforced alloy and the increase in normal load is shown in **Figure 3**. The resistance provided by the brittle asperities and the combined surface effects of ploughing and delamination brought on by the increased load are the causes of this phenomena. Ultimately, the wear rate rises considerably as a result of this higher stress. Moreover, a rise in stress might cause subsurface micro cracking, which would alter or reduce the surface asperities which can be seen from SEM images in **Figures 5** and **6**. Aluminium alloy contains hard alloy particles, which combine to form a mechanically mixed layer (MML) that is made up of a strong layer and a stretchable aluminium base matrix. The resultant lower rate of wear is due to this multi-layered material's effective ability to limit material exchange from the surface, maintaining a mild wear regime primarily controlled by an oxidative process.

Similar findings were reported by Raviraj et al. [22] in their investigation of the aluminium, zinc, and magnesium alloy as well as Verma and Singh [23], when they investigated wear analysis of aluminium matrix composite reinforced with high entropy alloy particles.

3.1. Specific wear rate and co-efficient of friction

Because of the presence of AlN particles, which withstand the applied stress, the contact surface between the produced composite pin sample and the counter steel

disc is less than in the parent alloy. Furthermore, when sliding, the AlN reinforcement material cannot separate from the aluminium matrix due to the high integrity between the reinforcement particle and the Al6061 matrix. Consequently, in comparison to the monolithic alloy, the Al6061/8 weight percentage AlN composites exhibited the lowest wear rate. The effect of normal force on the wear rate of the Al alloy without reinforcement and the Al6061/AlN alloy is shown in **Figure 4**. The chart clearly shows that the produced AMCs and plain matrix Al's wear performance increased linearly with an increase in normal load. An increase in load results in a higher WR for Al6061.

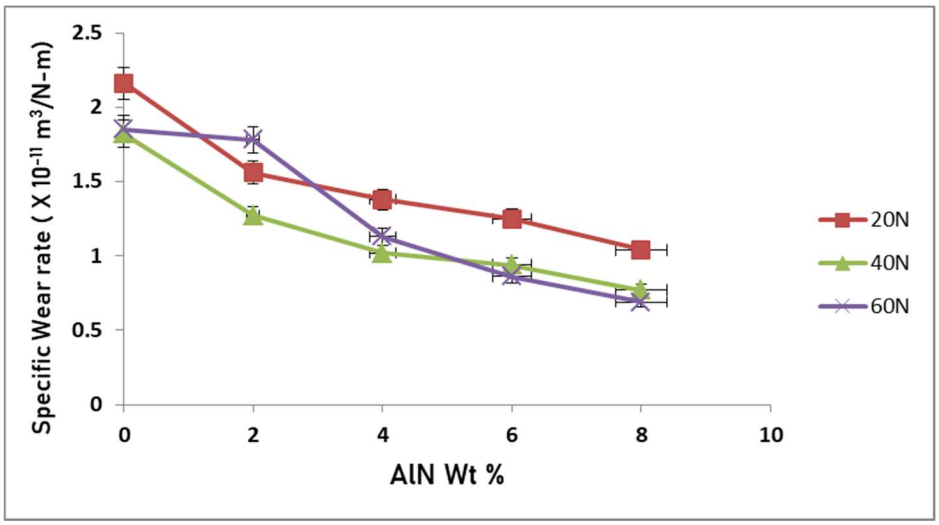

Figure 4. Specific wear rate of the AlN reinforced Al6061 alloy for different load conditions.

The surface material softens as a result of intense frictional heating brought on by increased applied stress. The hard asperity penetration much improves, leading to an increase in the composite material's plastic deformation. Consequently, these actions ultimately cause the composite's wear rate to increase.

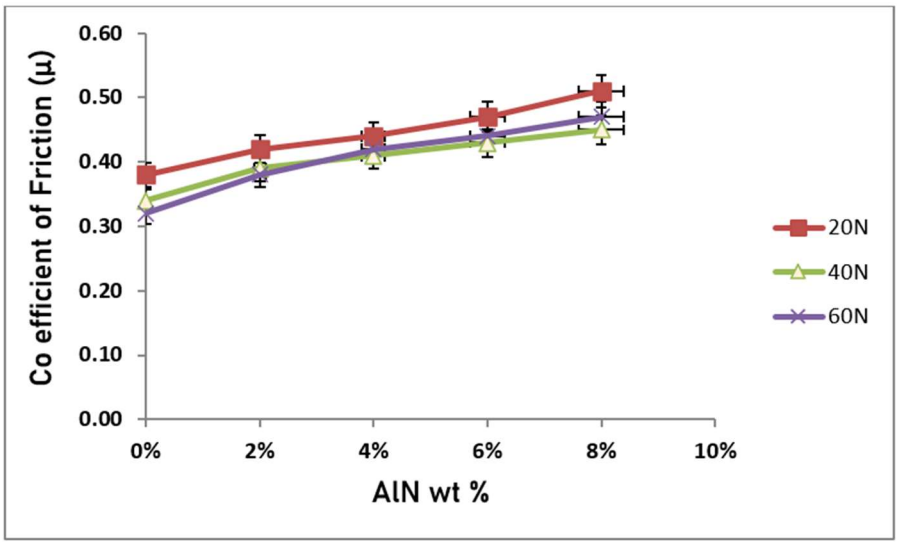

Figure 5. Friction coefficient of the AlN reinforced Al6061 alloy for different load conditions.

Figure 5 illustrates that the Al6061 has a lower coefficient of friction than the AlN-reinforced Al6061 samples. Variations in the degree of localised plastic deformation at actual contact locations might be the cause of variations in the friction coefficient. Because the AlN surfaces are tougher, it is anticipated that there would be less plastic deformation and reduced friction.It is clear that AlN reinforced alloys had less adhesive and abrasive wear because of their increased hardness and somewhat lower coefficient of friction, respectively.

A conductive epoxy composite with two hybrid filler reinforcement systems was created by Choi and Kim [24]. There are two types of systems: one with large-sized AlN particles and small-sized Al_2O_3 particles, and another with small-sized AlN particles and large-sized Al_2O_3 particles. At equal volume contents, this composite shows a higher packing density and a smaller surface area. The mechanical, electrical, and thermal characteristics of a modified AlN filled polyetherimide (PEI) composite were examined by Wu et al. [25]. With increased AlN levels, the tensile modulus, strength, thermal stability, and electrical characteristics improved. The values of the tensile strength are raised by 27% when 12.6 vol% AlN is added to the PEI matrix. The highest tensile modulus of the PEI matrix filled with 33.6 vol.% modified AlN fillers is 563.29 GPa, which is 300% more than the value of the pristine PEI matrix.

3.2. Morphology of worn-out surfaces

In order to comprehend the wear mechanism, it is necessary to examine the worn surfaces. At the sliding distance traversed with applied load condition, the worn surface topography is shown under SEM in **Figure 6**, showing prominent characteristics including asperity fragmentation, wear debris creation, fracture development, and delamination. Both the al6061 and the composite having AlN wt% Al6061 have more noticeable sliding grooves as a result of the asperities' abrasive ploughing effect on the tougher steel surface.

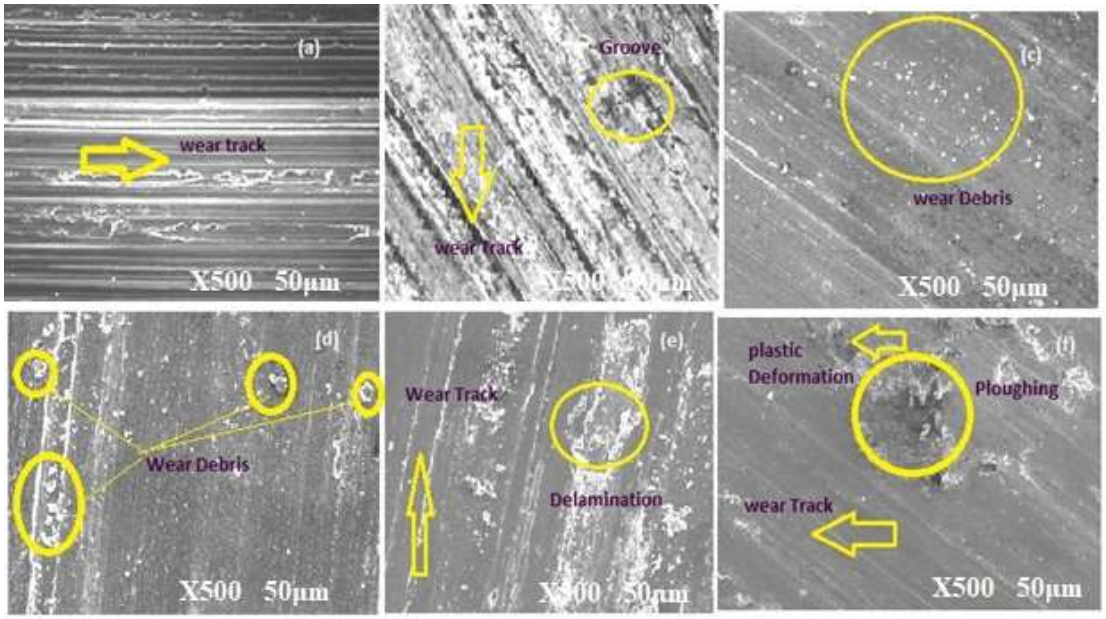

Figure 6. SEM morphology of worn out surfaces.

According to research by Tyagi et al. [26], the classification, geometry, and percentage of the reinforcing materials have a significant impact on the wear characteristics of Al-based composites.

In a study on the sliding wear performance of a hybrid Al2219/Grp/B4Cp composite, Rabindranath et al. [27] found that as load, speed, and travel distance rose, so did the wear in all the materials. On the other hand, the hybridised composite exhibited greater resistance to wear, most likely as a result of the presence of ceramic particle reinforcements. The pace at which material was removed from the composite's surface decreased as a result of the particles' strong resistance to the abrasive's micro-cutting of the composite.

Kumar et al. [28] investigated the wear response of an Al430-based composite including MgO and SiC. Investigators observed that the material wear increased as the reinforcing content increased. Maintaining a 2.5% reinforcement concentration at 600 rpm resulted in a 40% reduction in weight loss. Furthermore, a 45% and 91% wear decrease was seen at higher reinforcement concentrations of 5% and 7.5%, respectively. Additionally, compared to the basic alloy, the composite wear rate was reduced at different loads and speeds.

Delamination, adhesive, abrasive, and fretting wear modes can all affect Al-based MMCs. The relationship between each mechanism and surface morphology is discussed here. The Al6061/AlN alloy sample exhibits a mix of adhesion wear mechanism and deep grooves aligned in the sliding direction, indicating a plastic deformation caused by abrasion. As the two surfaces' interacting asperities fracture and undergo plastic deformation, fractured particles are created that serve as abrasive particles during sliding. As can be seen, these fragmented particles leave the surface and create voids. There have been reports of severe wear in several Al alloys in the past.

4. Conclusion

Al6061 alloy matrix composite reinforced with 0%, 2%, 4%, 6%, and 8% aluminium nitride (AlN) was successfully made using the stir cast approach and exhibited excellent qualities due to an efficient integration of the Al alloy and reinforcement components.

- The enhanced mechanical properties with higher AlN loading make these composites ideal for applications requiring high wear resistance and durability.
- For AlN reinforcement concentrations, the hardness values are progressively improved, ranging from 89.2 BHN at 0 wt% to 106.2 BHN at 8 wt%. Compared to plain matrix, the produced composites have a higher level of hardness.
- Al6061 with 6 wt% AlN alloy reveals 19.70% greater tensile strength when compared to Al6061 plain matrix alloy. Al6061/AlN composites achieves a peak yield strength of 205.32 MPa at 6% wt% AlN reinforcement.
- The wear rate reduced gradually when AlN was added, reaching a minimum at 8 wt% of AlN reinforcement.
- The adhesive mode of features for Al6061 matrix alloy and the abrasive mode of characteristics for Al6061/AlN AMCs are revealed by worn surface morphology. The composites made of Al6061/8 wt% AlN are ultimately shown

to have the best mechanical and wear characteristics. This makes Al6061/8 wt% AlN composites highly suitable for use in demanding environments such as automotive components or industrial machinery. Future studies could explore the long-term durability of these composites in various operational environments.

Author contributions: Conceptualization, SR and RM; methodology, MKN and MSV; software, CSA; validation, CSA and AKR; formal analysis, TNR and ND; investigation, SR, RM and CSA; resources, MKN and ND; data curation, RM and SR; writing—original draft preparation, SR; writing—review and editing, SR and RM; visualization, TNR and MSV; supervision, SR.

Conflict of interest: The authors declare no conflict of interest.

References

1. Tiwari A, Alenezi MR, Jun SC, et al. Advanced Composite Materials. Scrivener Publishing; 2016. pp. 1–462.
2. Backman DG, Williams JC. Advanced Materials for Aircraft Engine Applications. Science. 1992; 255(5048): 1082–1087. doi: 10.1126/science.255.5048.1082
3. Skoczylas J, Samborski S, Kłonica M. The Application of Composite Materials in The Aerospace Industry. Journal of Technology and Exploitation in Mechanical Engineering. 2019; 5(1). doi: 10.35784/jteme.73
4. Bhoi NK, Singh H, Pratap S. Developments in the aluminum metal matrix composites reinforced by micro/nano particles—A review. Journal of Composite Materials. 2019; 54(6): 813–833. doi: 10.1177/0021998319865307
5. Tanzi MC, Farè S, Candiani G. Organization, Structure, and Properties of Materials. Foundations of Biomaterials Engineering. 2019; 3–103. doi: 10.1016/b978-0-08-101034-1.00001-3
6. Gredelj S, Gerson AR, Kumar S, McIntyre NS. Plasma nitriding and in situ characterisation of aluminium. Applied Surface Science. 2002; 199(1–4): 234–247. doi: 10.1016/S0169-4332(02)00841-3
7. Blum M, Gyoktepeliler-Akin E, Killinger A. High velocity suspension flame spraying of AlN/Al_2O_3 composite coatings. Surface and Coatings Technology. 2022; 441: 128588. doi: 10.1016/j.surfcoat.2022.128588
8. Sager A, Esen I, Ahlatçi H, et al. Characterization and corrosion behavior of composites reinforced with ZK60, AlN, and SiC particles. Engineering Science and Technology, an International Journal. 2023; 41: 101389. doi: 10.1016/j.jestch.2023.101389
9. Mohanavel V, Ravichandran M. Experimental investigation on mechanical properties of AA7075-AlN composites. Materials Testing. 2019; 61(6): 554–558. doi: 10.3139/120.111354
10. Zhao M, Wu G, Zhu D, et al. Effects of thermal cycling on mechanical properties of AlNp/Al composite. Materials Letters. 2004; 58(12–13): 1899–1902. doi: 10.1016/j.matlet.2003.12.004
11. Lii DF, Huang JL. Shao-Ting Chang the mechanical properties of AlN/Al composites manufactured by squeeze casting. J. Eur. Ceram. Soc. 2002; 22: 253–261. doi:10.1016/S0955-2219(01)00255-2
12. Khrustalyov A, Zhukov I, Nikitin P, et al. Study of Influence of Aluminum Nitride Nanoparticles on the Structure, Phase Composition and Mechanical Properties of AZ91 Alloy. Metals. 2022; 12(2): 277. doi: 10.3390/met12020277
13. Pazhouhanfar Y, Eghbali B. Microstructural characterization and mechanical properties of TiB_2 reinforced Al6061 matrix composites produced using stir casting process. Materials Science and Engineering: A. 2018; 710: 172–180. doi: 10.1016/j.msea.2017.10.087
14. Pramanik. Effects of reinforcement on wear resistance of aluminum matrix composites. Transactions of Nonferrous Metals Society of China. 2016; 26(2): 348–358. doi:10.1016/S1003-6326(16)64125-0
15. D N, S R, Sivaram N, et al. Tribological characteristics of Al6061, boron, and graphite hybrid metal matrix composites. Advances in Materials and Processing Technologies. 2021; 8(3): 3248–3262. doi: 10.1080/2374068x.2021.1946323
16. Kumar GBV, Rao CSP, Selvaraj N, et al. Studies on Al6061-SiC and Al7075-Al2O3 Metal Matrix Composites. Journal of Minerals and Materials Characterization and Engineering. 2010; 09(01): 43–55. doi: 10.4236/jmmce.2010.91004
17. Park MH, Kim SH. Thermal conductivity of AlN thin films deposited by RF magnetron sputtering. Materials Science in Semiconductor Processing. 2012; 15(1): 6–10. doi: 10.1016/j.mssp.2011.04.007

18. Arık H, Kırmızı G, Özçatalbaş Y. Investigation of Production and Mechanical Properties of Alumix13-B4C MMK Material by TM Method. The Journal of International Manufacturing and Production Technologies. 2017.
19. Hillary JJM, Ramamoorthi R, Joseph JDJ, et al. A study on microstructural effect and mechanical behaviour of Al6061–5%SiC–TiB2 particulates reinforced hybrid metal matrix composites. Journal of Composite Materials. 2019; 54(17): 2327–2337. doi: 10.1177/0021998319894666
20. Şenel MC, Gürbüz M, Koç E. Fabrication and characterization of aluminum hybrid composites reinforced with silicon nitride/graphene nanoplatelet binary particles. Journal of Composite Materials. 2019; 53(28–30): 4043–4054. doi: 10.1177/0021998319853329
21. Abdelatty R, Khan A, Yusuf M, et al. Effect of Silicon Nitride and Graphene Nanoplatelets on the Properties of Aluminum Metal Matrix Composites. Materials. 2021; 14(8): 1898. doi: 10.3390/ma14081898
22. Shetty R, Hindi J, B MG, et al. Effect of metallic reinforcement and mechanically mixed layer on the tribological characteristics of Al-Zn-Mg alloy matrix composites under T6 treatment. Cogent Engineering. 2023; 10(1). doi: 10.1080/23311916.2023.2200900
23. Verma PK, Singh A. Mechanical and dry sliding tribological characteristics of aluminium matrix composite reinforced with high entropy alloy particles. Tribology International. 2024; 191: 109055. doi: 10.1016/j.triboint.2023.109055
24. Choi S, Kim J. Thermal conductivity of epoxy composites with a binary-particle system of aluminum oxide and aluminum nitride fillers. Composites Part B: Engineering. 2013; 51: 140–147. doi: 10.1016/j.compositesb.2013.03.002
25. Wu SY, Huang YL, Ma CCM, et al. Mechanical, thermal and electrical properties of aluminum nitride/polyetherimide composites. Composites Part A: Applied Science and Manufacturing. 2011; 42(11): 1573–1583. doi: 10.1016/j.compositesa.2011.06.009
26. Tyagi L, Butola R, Jha AK. Mechanical and tribological properties of AA7075-T6 metal matrix composite reinforced with ceramic particles and aloevera ash via Friction stir processing. Materials Research Express. 2020; 7(6): 066526. doi: 10.1088/2053-1591/ab9c5e
27. Ravindranath VM, Shiva Shankar GS, Basavarajappa S, et al. Dry sliding Wear Behavior of Hybrid aluminum Metal Matrix composite reinforced with Boron carbide and graphite particles. Materials Today: Proceedings. 2017; 4(10): 11163–11167. doi: 10.1016/j.matpr.2017.08.082
28. Mohan Kumar S, Pramod R, Govindaraju HK. Evaluation of Mechanical and Wear Properties of Aluminium AA430 Reinforced with SiC and Mgo. Materials Today: Proceedings. 2017; 4(2): 509–518. doi: 10.1016/j.matpr.2017.01.051

Materials Technology Reports 2024, 2(2), 1699.
https://doi.org/10.59400/mtr1699

Article

Preparation and characterization of $CuBO_2$-based photocatalysts and doped variants

Soheila Azordeh[1,*], Mehdi Asadi[2], Abdolali Alemi[1,*]

[1] Department of Chemistry, Tabriz University, Tabriz 5166616471, Iran
[2] Faculty of Natural Sciences, Geochemistry and Gemological Laboratory, University of Tabriz, 5166616471 Tabriz, Iran
*** Corresponding authors:** Soheila Azordeh, soheila.azorde@gmail.com; Abdolali Alemi, alemi@tabrizu.ac.ir

CITATION

Azordeh S, Asadi M, Alemi A. Preparation and characterization of $CuBO_2$-based photocatalysts and doped variants. Materials Technology Reports. 2024; 2(2): 1699. https://doi.org/10.59400/mtr1699

ARTICLE INFO

Received: 6 September 2024
Accepted: 20 November 2024
Available online: 26 November 2024

Abstract: An eco-friendly $CuBO_2$-based photocatalyst has been doped by a lanthanide for the first time. Gd^{3+} and Gd^{3+}/Bi^{3+}-doped $CuBO_2$ are synthesized by the hydrothermal method to study their magnetic properties. Then they are analyzed by XRD, UV-Vis, SEM, and VSM. The maximum amount of doping is x = 0 − 1.5% in $Cu_{1-3x}Gd_{3x}BO_2$ and $Cu_{1-3x}Bi_{3x/2}Gd_{3x/2}BO_2$ formulas as they are analyzed in XRD. For concentrations higher than x = 2%, the additional peak indicates that doping is incomplete. The XRD pattern of $CuBO_2$ confirms that its crystal structure is a hexagonal one with the $R\bar{3}m$ space group. According to UV-Vis analysis, the bandgap energies are 2.711, 2.753, and 2.765 for $CuBO_2$ and doped systems. Additionally, the morphology of particle sizes is confirmed according to SEM images. Meanwhile, the magnetic properties of synthesized material are studied by VSM, and the doped compound exhibited higher magnetic properties than $CuBO_2$, which is associated with the exchange interaction of electron and d spins in Gd^{3+} and Bi^{3+}. The study aims to provide insights into the magnetic properties of lanthanide-doped $CuBO_2$-based photocatalysts, potentially paving the way for developing improved magnetic materials for various applications.

Keywords: bandgap energy; $CuBO_2$; photocatalyst; lanthanide; magnetic properties

1. Introduction

One of the most intriguing issues for materializing oxide-based electronics is researching and expanding p-type wide-bandgap oxide materials. In order to achieve technologies such as electronics that are invisible and utilize wide bandgaps, p-type transparent conducting oxides (TCOs) are considered as key factors due to their appropriate electrical and optical features [1].

In the last decades, $CuBO_2$ has been known as the newest material among Copper delafossites, which can be as a hopeful electrical conductivity and splendid transparency at room temperature. However, few studies have been conducted on this important and valuable material [2–4]. This material with high photocatalytic activity was introduced as a p-type material of the environment-friendly TCO group by Chattopadhyay's research group [1].

Copper metaborate belongs to the group of oxide copper compounds and has various magnetic features [5]. Hence, Roessli et al. have reported that temperature changes affect the magnetic phase of such material and the phase changes from the paramagnetic to the commensurate weak ferromagnetic by decreasing temperature at $10 \leq T \leq 21$ K under zero magnetic field [6].

There are other various types of these compounds, i.e., CuB_2O_4, $Cu_3B_2O_6$, $Cu_2[BO(OH)_2](OH)_3$, $Cu_3B_6O_{12}\cdot H_2O$ and $Cu_3B_6O_{12}$ each of which is utilized in the

optical devices and electrodes according to their magnetic and electrical properties, respectively [7].

Chattopadhyay et al. studied the photocatalytic performance of this delafossite material for the first time with a standard photocatalytic set-up that showed the photocatalytic efficiency increased with decreasing particle size. The efficient photocatalytic performance made this novel p-type wide bandgap semiconductor an indeed multifunctional material [1].

In another study, Mero et al. studied the optical features of copper metaborate by spectroscopic ellipsometry and Raman scattering spectroscopy. The results illustrated that temperature reduction caused an unusual redshift to appear in the bandgap. In addition, upon cooling at 21 K—that is, the canted antiferromagnetic ordering temperature—the irregularities were observed in the bandgap, peak energy, and normalized intensity of charge transfer bands [8].

Scanlon et al. have utilized GGA corrected for on-site Coulomb interactions (GGA + U) and a hybrid density functional (HSE06) for investigating and computing the geometry and electronic structure of $CuBO_2$. The analysis of band extrema shows that boron (B) does not contribute to the state that controls conductivity. Also, good p-type conductivity was forecast. It is noticeable that the smaller Cu-Cu distance in such material in comparison with any other delafossites caused this increasing conductivity [4].

Other studies have investigated changes in the magnetic and optical properties of doped copper metaborate by Ni^{2+} and Mn^{2+} [9–11]. Doping is a common method used to intentionally introduce impurities (other cations) into the structure of semiconductors, thereby changing their electrical, optical, and magnetic properties, and improving their bandgap properties [12–14]. Hence, Khanh et al. demonstrated that electric polarization can be created and controlled in doped copper metaborate by Ni^{2+} under a magnetic field by investigating the magnetoelectric effect in the Ni/copper metaborate system [9].

On the other hand, lanthanides have recently gained attention due to their magnetic, optical, and electrical properties [15–19].

In this study, gadolinium has been selected as a lanthanide with magnetic properties [20,21], and the changes in the magnetic properties of doped copper metaborate by Gd^{3+} and Gd^{3+}/Bi^{3+} are compared. Notably, this is the first time a lanthanide has been doped into the copper metaborate structure in order to improve its magnetic properties.

2. Materials and methods

Copper acetate (99.99%), borax (99.0%), and bismuth nitrate pentahydrate (99.99%) purchased from Sigma-Aldrich, and sodium hydroxide (99.0%) and gadolinium oxide (99.9%) purchased from Merck, were used in the synthesis method. The purity of used materials is 99%. Also, XRD (Siemens D500), SEM (TESCAN MIRA3-FEG), UV-Vis (Sinco 4100), and VSM 7400 Lake Shore (VSM) are used for analyzing synthesized nanostructures.

2.1. Synthesis of $Cu_{1-3x}Gd_{3x}BO_2$

Gadolinium oxide was dissolved in the minimum amount of nitric acid according to **Table 1** with a determined molar ratio to use its nitrate in the reaction. Then copper acetate and 0.04 molar borax solutions are prepared in a separate beaker and added into the gadolinium-nitrate solution, and stirred for 30 min at 25 ℃. Next, 0.2 molars of NaOH are added to the main solution and stirred for 2 min at the same temperature. The mixture will be entered into the autoclave and heated for 10 hours at 180 ℃. The last step is cooling, filtering, washing with deionized water, and drying the obtained powder at room temperature [1,22,23].

Table 1. The ratio of used materials for the synthesis of $Cu_{1-3x}Gd_{3x}BO_2$.

Sample	Nitric acid (M)	Borax (mol)	Gadolinium oxide (mol)	Copper acetate (mol)	*x* (%)
A	0.2	0.0008	0.0062	0.003341	0.005
B			0.0124	0.003324	0.01
C			0.0186	0.003307	0.015
D			0.0248	0.003290	0.02

2.2. Synthesis of $Cu_{1-3x}Gd_{3x/2}Bi_{3x/2}BO_2$

Gd^{3+}/Bi^{3+} doped-$CuBO_2$ catalyst was synthesized by the same method in 2.1. The difference is that the ratio of used materials is according to **Table 2**.

Table 2. The ratio of used materials for the synthesis of $Cu_{1-3x}Gd_{3x/2}Bi_{3x/2}BO_2$.

Sample	Nitric acid (M)	Borax (mol)	Bismuth nitrate (mol)	Gadolinium oxide (mol)	Copper acetate (mol)	*x* (%)
A	0.2	0.0008	0.000017	0.0062	0.003324	0.01
B			0.0000255	0.0093	0.003307	0.015
C			0.000034	0.0124	0.003290	0.02

3. Results and discussion

3.1. XRD Pattern

According to the JCPDS card (No. 28–1256), the synthesized $CuBO_2$ organizes a hexagonal structure with an $R3\bar{m}$ space group [24,25]. XRD patterns in **Figure 1a,b,c** show there is no additional peak to behold in x = 1.5%. It can be concluded that Gd^{3+} is solvable in the $Cu_{1-3x}Gd_{3x}BO_2$ system up to x = 1.5%, while when x goes to 2%, there will be three additional peaks at 2θ = 28.15, 36.45, and 52.22. This could be related to oxidized non-doped gadolinium in the process of synthesis. **Figure 1d** indicates that incomplete doping is in accordance with gadolinium oxide peaks in the JCPDS card (No. 42–1465).

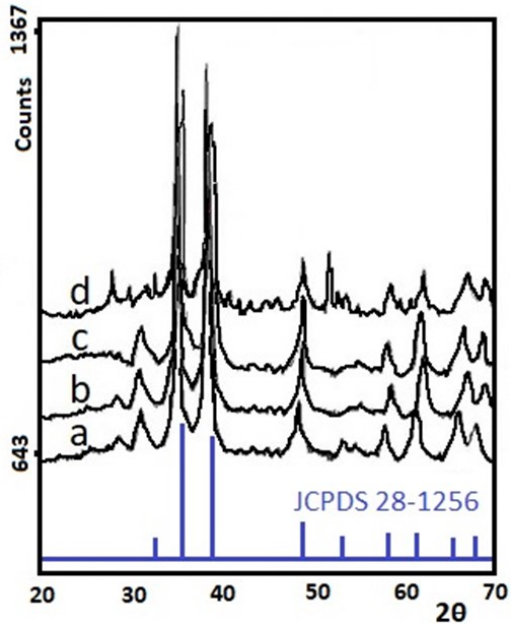

Figure 1. XRD patterns of $Cu_{1-3x}Gd_{3x}BO_2$ (**a**) x = 0.5%; (**b**) x = 1%; (**c**) x = 1.5%; and (**d**) x = 2%.

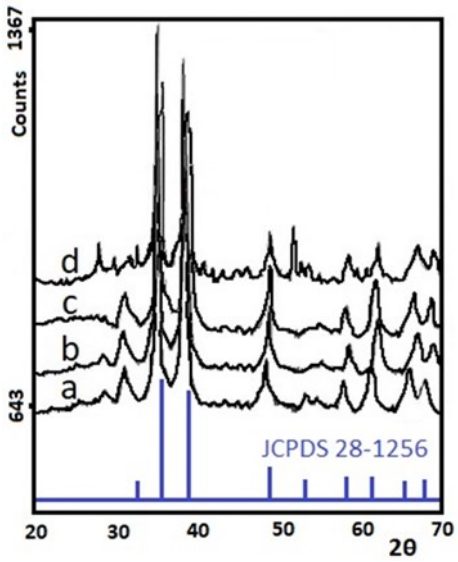

Figure 2. XRD spectra of (**a**) $Cu_{1-3x}Gd_{3x/2}Bi_{3x/2}BO_2$ (x = 1%); (**b**) $Cu_{1-3x}Gd_{3x/2}Bi_{3x/2}BO_2$ (x = 1.5%); (**c**) $Cu_{1-3x}Gd_{3x/2}Bi_{3x/2}BO_2$ (x = 2%).

Based on XRD spectra in **Figure 2a** and **2b**, it can be concluded that Bi^{3+} and Gd^{3+} are soluble in $Cu_{1-3x}Gd_{3x/2}Bi_{3x/2}BO_2$ system at the same concentration (x = 1.5%). **Figure 2c** illustrates that when x increases to 2%, there will be an additional peak at 2θ = 42.89, which shows incomplete doping.

3.2. UV-Vis analysis

The purpose of carrying out UV-Vis analysis is to calculate the bandgap and investigate electron transfer. **Figure 3** illustrates the UV-Vis spectra of $CuBO_2$, showing that absorption intensity has been increased by doping and a small shift has been observed in the wavelengths.

Indeed, electron transfer in copper metaborate is related to ligand-to-metal charge transfer [LMCT]. The absorption band is near 457 nm. This could be related to the electron transfer from the oxygen 2p orbital to the copper 4s orbital [LMCT].

It should be mentioned that LMCT is electron transfer from the valence band (O^{2-} : 2*p*) to the conductive band (Cu^{+}: 4*s*). There is no d-to-d orbital electron transfer because d orbitals are occupied in Cu^{+}. This applies to Bi^{3+} (6*p*) too. But f orbitals (4*f*) are partially filled in Gd^{3+}; therefore, *f*-to-*f* orbital electron transfer can occur. Hence, they have shifted to shorter wavelengths.

In order to calculate bandgap energy, Equation (1) is used, where h is Planck's constant, c is the velocity of light, and λ is the wavelength [26]:

$$E = hc/\lambda$$
$$E = 1239/\lambda \text{ (eV)} \quad (1)$$

The calculated bandgap energies for $CuBO_2$, $Cu_{1-3x}Gd_{3x}BO_2$, and $Cu_{1-3x}Gd_{3x/2}Bi_{3x/2}BO_2$ are 2.711, 2.753, and 2.765 eV, respectively.

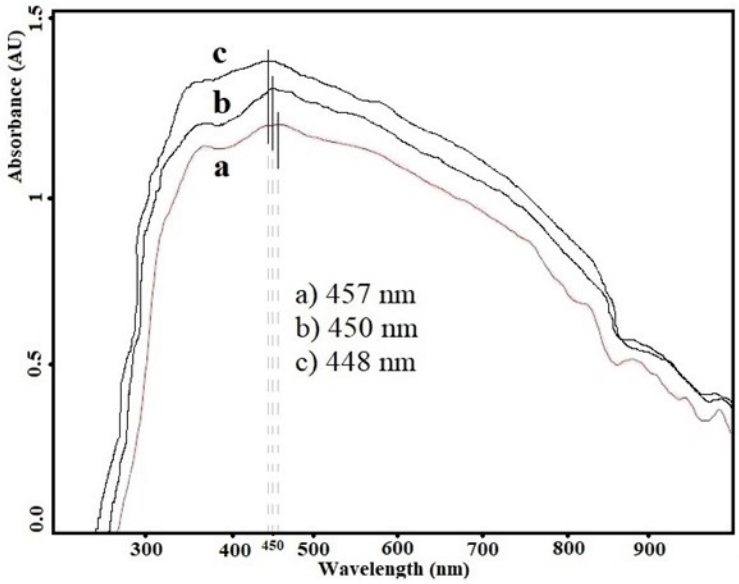

Figure 3. UV-Vis spectra of (**a**) $CuBO_2$ nanopowders; (**b**) $Cu_{1-3x}Gd_{3x}BO_2$ (x = 1.5%); and (**c**) $Cu_{1-3x}Gd_{3x/2}Bi_{3x/2}BO_2$ (x = 1.5%).

3.3. Magnetic spectra analysis

Magnetic measurements of samples were performed by VSM. The results are demonstrated in the magnetization curves based on magnetic field strength. **Figures 4a–4c** indicates magnetization curves based on the magnetic field in synthesized nanopowders for different x at room temperature. As seen, all samples include a hysteresis curve, so they have paramagnetic properties. (Hc) and (Ms) of samples are seen in graphs.

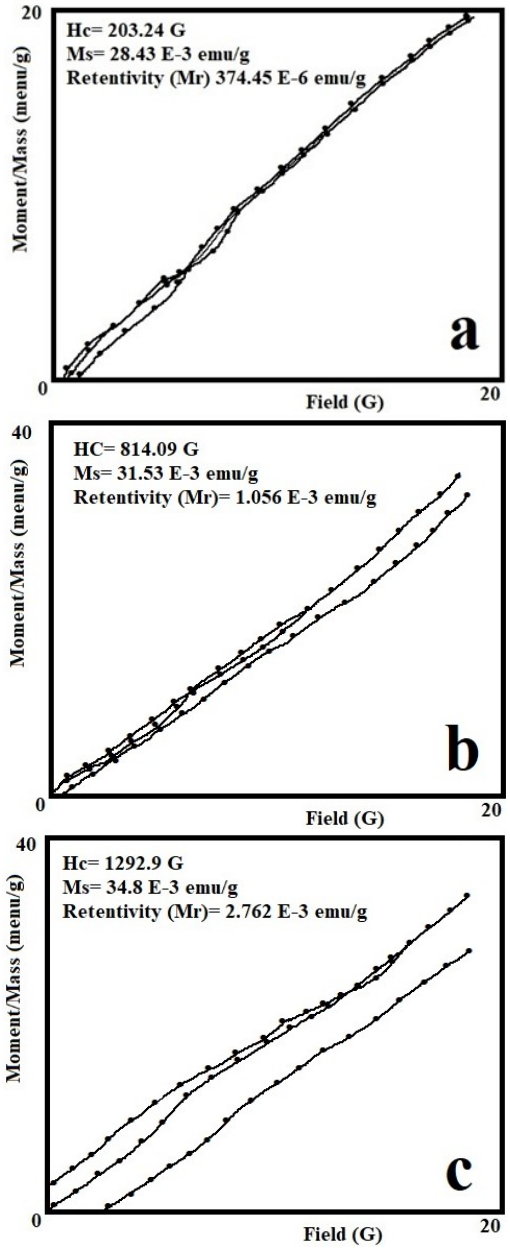

Figure 4. Magnetization curve on the basis of the external magnetic field in room temperature of **(a)** $CuBO_2$ nanopowders; **(b)** $Cu_{1-3x}Gd_xBO_2$ (x = 1.5%); and **(c)** $Cu_{1-3x}Gd_{3x/2}Bi_{3x/2}BO_2$ (x = 1.5%).

As can be seen in **Figure 4**, (Ms) increases as the type of doped element changes. This is because of the increase in the replacement magnetic moment in the host network [27]. Indeed, in a magnetic network, electrons will be polarized by the injection of magnetic ions at a determined level. It is the result of exchange interactions in Ruderman-Kittel-Kasuya-Yosida (RKKY). This impurity can have paramagnetic properties [28]. Therefore, paramagnetic features in doped compositions are obtained by the exchange interaction of electron and d spins in Gd^{3+} and Bi^{3+}. The interaction can cause a regular arrangement of adjacent spins and the magnetization of the network.

3.4. SEM images

The purpose of electron microscopy images is the analysis of surface morphology, grain size, and distribution. The magnifications of 30000x and 50000x for analyzing powders were used (**Figure 5**). The frequency of particles shows that their size is around 60 nm. It should be mentioned that the distribution is high and the highest frequency is in the range of 59 nm to 65 nm.

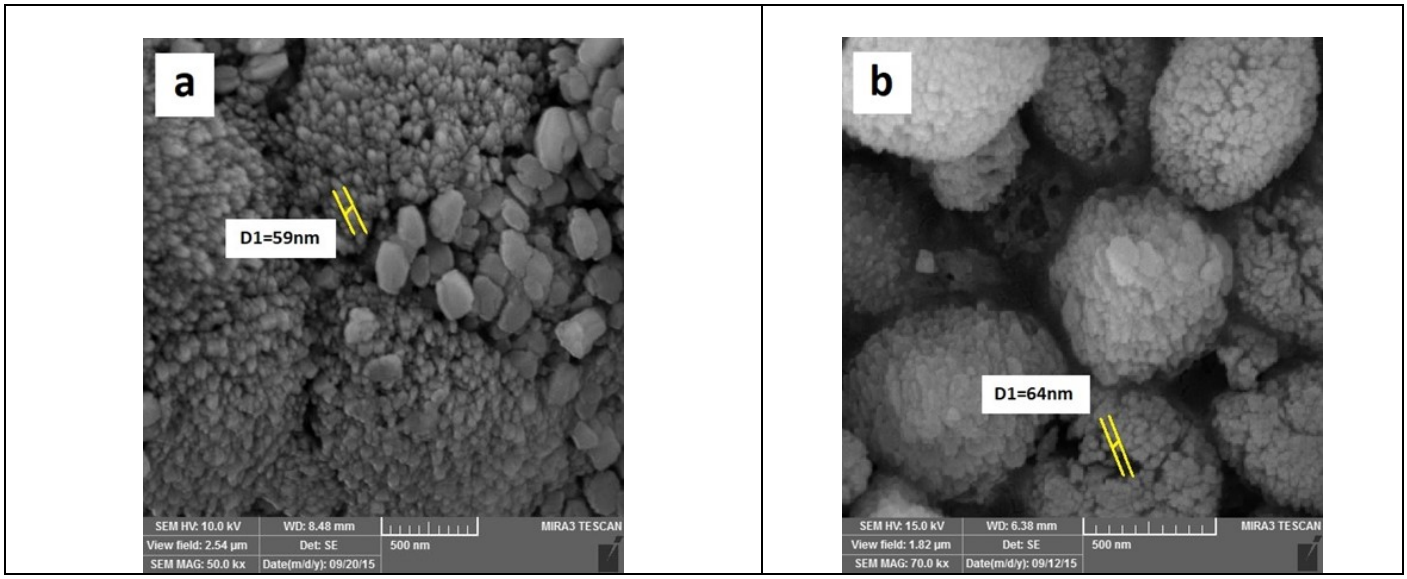

Figure 5. SEM image of **(a)** $Cu_{1-3x}Gd_{3x}BO_2$; and **(b)** $Cu_{1-3x}Gd_{3x/2}Bi_{3x/2}BO_2$.

4. Conclusion

This study successfully doped nano $CuBO_2$ with a lanthanide for the first time. The XRD pattern of the synthesized samples illustrated that the maximum amount of doping is $x = 0 - 1.5\%$. In concentrations higher than $x = 2\%$, additional peaks are observed that indicate doping is incomplete. LMCT is electron transfer from the valence band (O^{2-}: 2*p*) to the conductive band (Cu^{+}: *4s*). There is no *d*-to-*d* orbital electron transfer because *d* orbitals are occupied in Cu^{+}. This applies to Bi^{3+} (6*p*) too. But *f* orbitals (4*f*) are partially filled in Gd^{3+}, so *f*-to-*f* orbital electron transfer can be carried out. Hence, they have shifted to shorter wavelengths, and the calculated bandgap energies for $CuBO_2$, $Cu_{1-3x}Gd_{3x}BO_2$, and $Cu_{1-3x}Gd_{3x/2}Bi_{3x/2}BO_2$ are 2.711, 2.753, and 2.765 *eV*, respectively. Magnetic curves of samples demonstrated that all of the samples include hysteresis curves, and (Ms) increases as the type of doped element changes. It is because of the increase in the replacement magnetic moment in the host network. Therefore, paramagnetic properties in doped compositions are obtained by the exchange interaction of electron and *d* spins in Gd^{3+} and Bi^{3+}. The interaction can cause a regular arrangement of adjacent spins and the magnetization of the network.

Author contributions: Conceptualization, SA and MA; methodology, SA; software, SA; validation, SA and AA; formal analysis, SA and AA; investigation, SA and MA; resources, SA and MA; data curation, SA and AA; writing—original draft preparation, SA and MA; writing—review and editing, SA and MA; visualization,

SA; supervision, AA; project administration, SA and AA; funding acquisition, AA. All authors have read and agreed to the published version of the manuscript.

Conflict of interest: The authors declare no conflict of interest.

References

1. Santra S, Das NS, Chattopadhyay KK. Wide band gap p-type nanocrystalline CuBO2 as a novel UV photocatalyst. Materials Research Bulletin. 2013; 48(7): 2669–2677. doi: 10.1016/j.materresbull.2013.03.034
2. Snure M, Tiwari A. CuBO2: A p-type transparent oxide. Applied Physics Letters. 2007; 91(9). doi: 10.1063/1.2778755
3. Zheng Y, Wang Z, Tian Y, et al. Synthesis and performance of 1D and 2D copper borate nano/microstructures with different morphologies. Colloids and Surfaces A: Physicochemical and Engineering Aspects. 2009; 349(1–3): 156–161. doi: 10.1016/j.colsurfa.2009.08.012
4. Scanlon DO, Walsh A, Watson GW. Understanding the p-Type Conduction Properties of the Transparent Conducting Oxide CuBO2: A Density Functional Theory Analysis. Chemistry of Materials. 2009; 21(19): 4568–4576. doi: 10.1021/cm9015113
5. Bolsunovskaya O, Popov M, Petrakovskii G, et al. Magnetic structure and elementary excitation spectra of copper metaborate. Journal of Magnetism and Magnetic Materials. 2006; 300(1): e392–e394. doi: 10.1016/j.jmmm.2005.10.127
6. Roessli B, Schefer J, Petrakovskii GA, et al. Formation of a Magnetic Soliton Lattice in Copper Metaborate. Physical Review Letters. 2001; 86(9): 1885–1888. doi: 10.1103/physrevlett.86.1885
7. Kipcak AS, Senberber FT, Aydin Yuksel S, et al. Synthesis, characterisation, electrical and optical properties of copper borate compounds. Materials Research Bulletin. 2015; 70: 442–448. doi: 10.1016/j.materresbull.2015.05.003
8. Mero RD, Lai CH, Du CH, et al. Spectroscopic Signature of Spin–Charge–Lattice Coupling in CuB2O4. The Journal of Physical Chemistry C. 2021; 125(7): 4322–4329. doi: 10.1021/acs.jpcc.1c00111
9. Khanh ND, Abe N, Kubo K, et al. Magnetic control of electric polarization in the noncentrosymmetric compound (Cu,Ni)B2O4. Physical Review B. 2013; 87(18). doi: 10.1103/physrevb.87.184416
10. Molchanova AD, Boldyrev KN, Erofeev AS, et al. Magnetic phase transitions and linear magnetic dichroism in manganese-doped copper metaborate (Cu,Mn)B2O4. Journal of Physics: Conference Series. 2017; 917: 072003. doi: 10.1088/1742-6596/917/7/072003
11. A.D. Molchanova, E.M. Moshkina, M.S. Molokeev, E.V. Tropina, A.F. Bovina, K.N. Boldyrev, Synthesis and optical properties of nickel-doped copper metaborate crystals, Opt. Spectrosc. 2022, 130.
12. Giri S, Trewyn BG, Stellmaker MP, et al. Stimuli—Responsive Controlled—Release Delivery System Based on Mesoporous Silica Nanorods Capped with Magnetic Nanoparticles. Angewandte Chemie International Edition. 2005; 44(32): 5038–5044. doi: 10.1002/anie.200501819
13. Bergemann C, Muller-Schulte D, Oster J, et al. Magnetic ion-exchange nano- and microparticles for medical, biochemical and molecular biological applications. J. Magn. Magn. Mater. 1999; 194: 45.
14. Nunez L, Kaminski MD. Transuranic separation using organophosphorus extractants adsorbed onto superparamagnetic carriers. J. Magn. Magn. Mater. 1999; 194: 102.
15. Ellis MC. Understanding Magnetic and Optical Properties of Lanthanide-Doped Oxide Nanospinels and Heterometallic Formate Metal-Organic Frameworks [PhD thesis]. Florida State University Libraries; 2020.
16. Reisfeld R. Optical Properties of Lanthanides in Condensed Phase, Theory and Applications. AIMS Materials Science. 2015; 2(2): 37–60. doi: 10.3934/matersci.2015.2.37
17. Brik MG, Srivastava AM. 1.8 Electronic properties of the lanthanide ions. Rare Earth Chemistry. 2020: 83–96. doi: 10.1515/9783110654929-008
18. Kurzen H, Bovigny L, Bulloni C, et al. Electronic structure and magnetic properties of lanthanide 3+ cations. Chemical Physics Letters. 2013; 574: 129–132. doi: 10.1016/j.cplett.2013.04.070
19. Sorace L, Gatteschi D. Lanthanides and an Actinides in molecular magnetism 1st ed. In:Electronic Structure and Magnetic Properties of Lanthanide Molecular Complexes. Wiley-VCH Verlag GmbH & Co. KGaA; 2015.
20. Ncube S, Coleman C, Strydom A, et al. Kondo effect and enhanced magnetic properties in gadolinium functionalized carbon nanotube supramolecular complex. Scientific Reports. 2018; 8(1). doi: 10.1038/s41598-018-26428-y
21. Serga V, Burve R, Maiorov M, et al. Impact of Gadolinium on the Structure and Magnetic Properties of Nanocrystalline Powders of Iron Oxides Produced by the Extraction-Pyrolytic Method. Materials. 2020; 13(18): 4147. doi:

10.3390/ma13184147

22. Bae J, Shin D, Jeong H, et al. Highly Water-Resistant La-Doped Co3O4 Catalyst for CO Oxidation. ACS Catalysis. 2019; 9(11): 10093–10100. doi: 10.1021/acscatal.9b02920
23. Santra S, Das NS, Maiti S, et al. Wide band gap p-type CuBO2 nanostructures by hydrothermal route and fabrication high quality p-CuBO2/n-ZnO nano-heterojunction. Chemical Physics Letters. 2014; 604: 97–100. doi: 10.1016/j.cplett.2014.04.052
24. Ruttanapun C. Optical and electronic properties of delafossite CuBO2 p-type transparent conducting oxide. Journal of Applied Physics. 2013; 114(11): 113108. doi: 10.1063/1.4821960
25. Santra S, Das NS, Chattopadhyay KK. Sol–gel synthesis and characterization of wide band gap p-type nanocrystalline CuBO2. Materials Letters. 2013; 92: 198–201. doi: 10.1016/j.matlet.2012.10.094
26. Connors KA. The Phenomenological Theory of Solvent Effects in Mixed Solvent Systems. Handbook of Solvents. 2014: 467–490. doi: 10.1016/b978-1-895198-64-5.50013-1
27. Madhusudan KR, Manorama SV, Ramachandra RA. Bandgap studies on anatase titanium dioxide nanoparticles. Mater. Chem. Phys. 2003; 78: 239.
28. Morales AE, Mora ES, Pal U. Use of diffuse reflectance spectroscopy for optical characterization of un-supported nanostructures. Rev. Mex. de Fis. 2007; 53: 18.

Materials Technology Reports 2024, 2(2), 1762.
https://doi.org/10.59400/mtr1762

Article

Potentiality of alginate-yeast biosorbent for biogas purification

Norli Ismail[1,*], Bilhate Chala[2], Joachim Mueller[2], Hans Oechsner[3]

[1] Environmental Technology Division, School of Industrial Technology, Universiti Sains Malaysia, Gelugor, Penang 11800, Malaysia
[2] Institute of Agricultural Engineering (440e), Department of Agricultural Engineering in the Tropics and Subtropics, University of Hohenheim, 70599 Stuttgart, Germany
[3] State Institute of Agricultural Engineering and Bioenergy, University of Hohenheim, 70599 Stuttgart, Germany
*** Corresponding author:** Norli Ismail, norlii@usm.my

CITATION

Ismail N, Chala B, Mueller J, Oechsner H. Potentiality of alginate-yeast biosorbent for biogas purification. Materials Technology Reports. 2024; 2(1): 1762. https://doi.org/10.59400/mtr1762

ARTICLE INFO

Received: 23 September 2024
Accepted: 27 November 2024
Available online: 3 December 2024

Abstract: The paper discussed the current research on the applicability of biosorbents for the purification of biogas, particularly the decrease of H_2S by using encapsulated or embedded biological biomass. This study investigated the potential of alginate-yeast biosorbent (AlgY) for biogas purification, focusing on hydrogen sulfide (H_2S) removal. A biogas column test was conducted to compare the biosorption efficiency of AlgY and pure alginate beads. Using Response Surface Methodology (RSM), the effects of column length, acquisition time, and biosorbent type were evaluated for CH_4, CO_2, and H_2S removal. Results depicted significant H_2S reduction, with AlgY achieving a p-value of < 0.0001 and a high correlation coefficient (R^2 = 0.9518). The relatively high correlation coefficient (R^2) of the tested quadratic model of all the responses were recorded (R^2; 0.5560, 0.5048, and 0.9518 for CH_4, CO_2, and H_2S respectively). According to the studies' preliminary findings, the type of biosorbent has a significant role in determining the biosorption effectiveness. The ANOVA of model terms depicted a significant p-value ($p < 0.05$) indicated a potential alginate-yeast (AlgY) biosorbent for H_2S purification or reduction.

Keywords: biosorbent; yeast-alginate bead; biogas

1. Introduction

The article reported the previous and ongoing research works on biobased materials that are biofiller and biosorbent adaptable for pollutant reduction through the encapsulated microbial biomass and embedded yeast biomass respectively. The findings broaden the green process technology approaches and help to minimize the secondary pollution problems in addressing environmental sustainability. The other part of the article presented the findings of the biosorbent preliminary study synthesized from dry yeast and maize silage biomass.

Various materials including microalgal biomass olive pomace [1], and banana fiber [2] have been previously examined for this purpose. Ciapponi [3] investigated how renewable fillers influence the mechanical properties of plasticized gluten. The findings revealed that incorporating microalgal biomass, which resulted in a modest enhancement of surface sensitivity to water. However, despite this increase in surface sensitivity, the biomass contributed to a reduction in water absorption kinetics and were assessed for materials in the presence of different flexibilities.

Consequently, biomass that derived from microalgae emerges as a compelling and sustainable resource for developing gluten-based materials, particularly for enhancing mechanical properties without compromising thermal stability or water resistance. Current research predominantly focuses on the progression of Polymer

Matrix Composites (PMCs), which are strengthened with various fibers (both natural and synthetic) and supplemented with fillers (both organic and inorganic). This emphasis is due to the inherent in these composites is a wide range of characteristics and attributes [4,5].

The possibility of yeast (Saccharomyces cerevisiae) biomass was encapsulated or immobilized in the calcium alginates beads. The findings of calcium alginatere beads encapsulated with yeast biomass for hydrogen sulphides (H_2S) and carbon dioxide concentration are presented. As mentioned in other sources, the majority of yeasts exhibit robust growth within the pH range of 4.5 to 6.5. However, virtually all species demonstrate the capability to thrive in media with either more acidic or alkaline conditions. Saccharomyces cerevisiae for instance, the primary species employed in industrial bioethanol production achieves optimal growth under pH conditions ranging from 4.0 to 6.0 [6]. Fungi growth is regulated by various factors, among them signalling molecules like hydrogen sulphide (H_2S), traditionally considered a toxic gas devoid of physiological function. Enzymatically and endogenously produced in numerous species, H_2S acts as a gaseous signalling molecule, playing a crucial role in various essential biological functions. A surface, intersurface, metabolism reaction could be a possible mechanism which occurs during the treatment process [7]. The experimental design incorporated the use of Response Surface Methodology (RSM). RSM offers a structured statistical design methodology for investigating the collective impact of two or more variables employed in an experiment [8].

Drawn from enzymatic reactions, particularly those originating from in vivo CO_2 metabolic processes, this approach could offer a more efficient and environmentally friendly method for CO_2 conversion. This is attributed to its elevated stereospecificity and enantioselectivity [9]. In principle, the biomineralization processes can employ carbon dioxide (CO_2) to produce $CaCO_3$ particles, and this preparation is recognized as an environmentally conscious and eco-friendly method for carbon dioxide sequestration [10]. The CO_2 catalytic conversion into $CaCO_3$ particles using calcium alginate (CA) occurs through three distinct stages.

$$CO_2 + H_2O \leftrightarrow CA\ HCO^{-3} + H^+ \quad (1)$$

$$HCO^{-3} \rightarrow H^+ + CO_2{}^{-3} \quad (2)$$

$$Ca^{2+} + CO_2{}^{-3} \rightarrow CaCO_3 \quad (3)$$

Of the mentioned reactions, step (1) is the least rapid, signifying that it serves as the rate-limiting step. Of the mentioned reactions, step (1) is the least rapid, signifying that it serves as the rate-limiting step [11]. The core concept is that CA catalyzes the swift conversion of H_2O and CO_2 into H^+ and HCO_3^- ions initially. Following this, the HCO_3^- undergoes an easy transformation into CO_3^{2-}, subsequently reacting with the introduced Ca^{2+} to yield $CaCO_3$ [12]. Bioassimilation refers to the mechanism through which organisms assimilate specific elements, compounds, or particles from their surroundings, incorporating them into their own physiological structures. It holds a crucial function in diverse living systems, manifesting both advantageous and adverse impacts on species and ecosystems

[13,14]. Adsorption is defined as the alteration in the density of a molecule at the surface layer of a solid material in comparison to the bulk phase per unit surface area. The term sorption is a comprehensive expression encompassing both absorption and adsorption processes [15]. These terms are often confused. Absorption is the incorporation of a substance in one state into another of a different state (e.g., liquids being absorbed by a solid or gases), i.e., into a three-dimensional matrix [16]. Biosorption or bio-adsorption may be simply defined as the removal of substances from pollution matrix of phases by biological materials [17].

The precise binding mechanisms may range from physical, i.e., electrostatic interactions, van der Waals forces, hydrogen bond, to chemical binding, i.e., ionic and covalent. Some of the reported mechanisms include absorption, (surface) adsorption, ion exchange, binding or surface complexation, (surface) precipitation or microprecipitation, and mineral nucleation. Biosorption is a property of both living and dead organisms, and their components. While most biosorption research concerns metals and related substances, the term is now applied to particulates and all manner of organic substances as well. Practically, all biological material has an affinity for metal species [18]. However, the term "biosorption" refers to the passive or physicochemical attachment of a sorbate to a biosorbent, essentially the binding of a chemical species to biopolymers. The definition, thus, specifically excludes metabolic or active uptake by living, metabolizing cells. In the literature, the term "biosorbent" includes the usage of dead biomass such as fibres, peat, rice hulls, forest by-products, chitosan and agro-food wastes as well as living plants, fungi, algae (unicellular microalgae, cyanobacteria, multicellular macroalgae) and bacteria. Biosorbents represent cheap filter materials often with high affinity, capacity and selectivity, and they are abundant and already available in most places [19–21].

2. Materials and method

2.1. Experimental setup and preparation of yeast-alginate bead

The experiments were conducted in a controlled laboratory setting. The experimental setup of the biosorbent preparation and the biogas purification column test are illustrated in **Figures 1** and **2** respectively.

A calcium alginate bead and yeast-alginate beads/biosorbent were prepared as described by [22] with minor modification. Alginate solution was firstly performed by stirring sodium alginate (Fisher Scientific) in warm distilled water. Yeast-alginate beads were prepared by mixing Saccharomyces cerevisiae with sodium alginate, followed by crosslinking with $CaCl_2$. Crosslinking agents were selected based on their ability to enhance bead stability and biosorption capacity. The 3.5 g dried yeast, Saccharomyces cerevisiae was mixed with 8 g of sodium alginate and added to 400 mL warm (50–60 °C) distilled water and stir on the heater-magnetic stirrer for 5–10 min to obtain a yeast-alginate slurry. Later the heater was switch off and the calcium alginate (control) and yeast alginate slurry were kept under gentle stirring until the mixtures are mixed completely. The immobilization of Saccharomyces cerevisiae biomass was carried out in a 1 L beaker containing 0.1 M $CaCl_2$ solution with the agitation speed of 450 rpm. The prepared slurries were added drop-wise in a $CaCl_2$ solution using an appropriate dropper manually. The bead size (3 ± 0.3 mm of

diameter) formed was stirred in the $CaCl_2$ solution for 20 min at room temperature to allow complete gelation. The spherical beads were washed several times to eliminate the remaining $CaCl_2$.

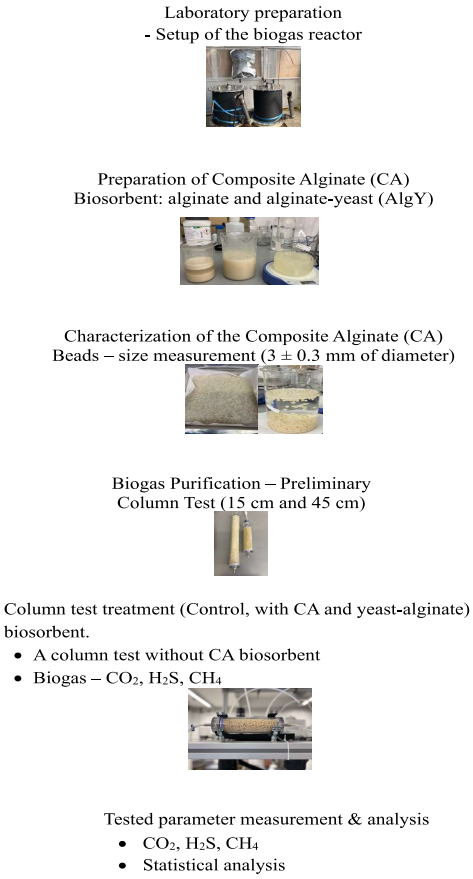

Figure 1. Illustrated the research flowchart of the study.

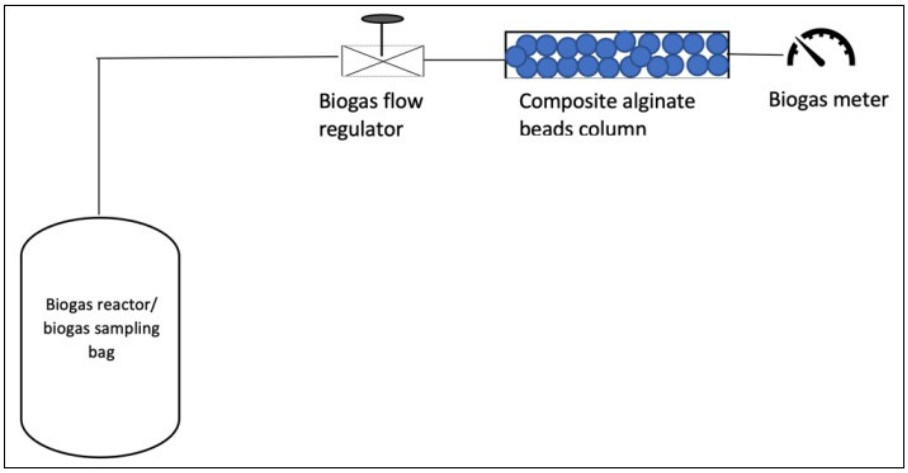

Figure 2. Schematic diagram of the biogas purification column test set up.

2.2. Design of experiment for biosorption test column

A Central Composite Design (CCD) was employed to investigate the effects of column length (15–45 cm), acquisition time (5–20 min), and biosorbent type (control and AlgY). **Table 1** summarized the CCD design of experiment depicted the three

levels of the two numerical parameter variables, column length and acquisition time. Two different types of scrubbers/biosorbents that is sodium alginate and Alginate-yeast were selected as categorical variables. Statistical analyses using RSM were conducted with Design Expert software, evaluating model adequacy through *p*-values and R^2. The effects of these parameters on the ability of alginate-yeast encapsulation on the methane, carbon dioxide and hydrogen sulphide concentration of the maize silage anaerobic digester were discussed based on the response surface methodology (RSM) central composite design (CCD) and fitted model looking at the factor's interaction.

The experimental data were analyzed by RSM using the Design Expert 11.0 trial version (STAT-EASE Inc., Minneapolis, USA). The response surface was applied to describe the effects of different factors on yeast alginate biosorption. The 16 runs in a single block were designed to study the effects of three factors on three response variables. The Fisher's test (*F*-value) and *p*-value at 95% confident level was used to evaluate the statistically significant of the model equation and the model term. **Table 2** illustrated the summary of CCD experimental design selected for the experiment. The quality of the model fitted to the quadratic regression equation was determined via the coefficient of determination (R^2). The fitted equation was presented in contour and 3D plots to explain the relationship between the responses and the experimental levels. The results depicted the response variables of yeast alginate biosorbent with the control.

Table 1. Range of numerical and categorical variables used in the RSM central composite design.

Factors	Unit	Type	Symbol codes	Coded levels	
				−1	1
Length of column	cm	Numeric	X_1	15	45
Acquisition time	minute	Numeric	X_2	5	20
Type of biosorbent	-	Categoric	X_3	Control	AlgY

Table 2. Summary of RSM central composite design carried out in the study.

	Factor			The experimental response data		
Run	Column length	Acquisition time	Type of biosorbent	CH_4	CO_2	H_2S
	cm	Minute	-	%	%	ppm
1	30	5	Control			
2	45	5	AlgY			
3	15	12.5	AlgY			
4	30	5	AlgY			
5	45	20	AlgY			
6	45	12.5	AlgY			
7	15	12.5	Control			
8	30	20	Control			
9	45	12.5	Control			
10	15	20	Control			

Table 2. (*Continued*).

	Factor			The experimental response data		
Run	**Column length**	**Acquisition time**	**Type of biosorbent**	**CH_4**	**CO_2**	**H_2S**
	cm	**Minute**	**-**	**%**	**%**	**ppm**
11	15	20	AlgY			
12	45	5	Control			
13	15	5	Control			
14	45	20	Control			
15	30	20	AlgY			
16	15	5	AlgY			

3. Results

3.1. Performance of the preliminary study of the alginate biosorbent

The results of the preliminary study were depicted in **Tables 3** and **4** for the descriptive statistic of the biosorbent performance and the experimental response data (CH_4, CO_2, H_2S) towards the factors studied respectively. The results exhibited a promising reduction in H_2S concentrations for the alginate-yeast (AlgY) biosorbent. Alginate-yeast was observed to improve CH_4 purification compared to control of the overall experimental runs. Similar trend occurred in CO_2 concentrations reduction.

The Central Composite Design (CCD) of RSM was operated to analyse the three parameters; column length (X_1), acquisition time (X_2), and type of biosorbent (X_3) for biogas purification. The three independent factors were studied at two levels (−1, 1) as stated in **Table 1**. The CH_4, CO_2 and H_2S sorption efficiencies were noted as response values; Y_1, Y_2 and Y_3 respectively. Each experiment was the average of the triplicate. The 16 runs were randomly performed to analyse the process variable (**Table 2**). For Central Composite design, an appropriate fitted quadratic model was established to illustrate the effect of each factor and their quadratic interaction, which is determine in the following Equation (1).

$$Y = a_0 + \sum_{i=1}^{n} a_i + \sum_{i=1}^{n} a_{ii} X_i^2 + \sum_{i=1}^{n} \sum_{j=1}^{n} a_{ij} X_i X_j + \varepsilon \quad (1)$$

where Y is the predicted response, x_i and x_j are independent factors, a_0 is intercept, ai is linear coefficient, a_{ii} is quadratic coefficient, and a_{ij} is interaction coefficient, respectively whilst, ε is the random error or uncertainties between predicted values. **Table 3** is the presented results (descriptive statistic) of the study outcomes/findings. It is not a data from any references.

Table 3. A descriptive statistic of the biosorption performance.

Response	Unit	Minimum	Maximum	Mean	Std. Dev.
CH_4	%	51.3157	64.1025	55.9976	2.3037
CO_2	%	29.8682	40.9008	38.0869	3.0642
H_2S	ppm	0.0000	0.0045	0.0019	0.0014

Table 4. Experimental response data of the CCD.

	Factor			The experimental response data		
Run	**Column length**	**Acquisition time**	**Type of biosorbent**	**CH_4**	**CO_2**	**H_2S**
	cm	Minute	-	%	%	ppm
1	30	5	Control	54.0805	41.1018	0.0031
2	45	5	AlgY	55.7741	40.3798	0.0000
3	15	12.5	AlgY	55.6839	33.0012	0.0000
4	30	5	AlgY	61.5787	27.3164	0.0000
5	45	20	AlgY	57.7003	38.2491	0.0000
6	45	12.5	AlgY	56.1015	39.9914	0.0000
7	15	12.5	Control	51.5724	31.4814	0.0024
8	30	20	Control	55.3274	40.1459	0.0037
9	45	12.5	Control	55.3609	40.1261	0.0034
10	15	20	Control	55.7223	39.7518	0.0042
11	15	20	AlgY	55.9157	39.2705	0.0007
12	45	5	Control	55.5904	39.9123	0.0037
13	15	5	Control	55.9445	39.7251	0.0045
14	45	20	Control	55.1074	40.1981	0.0032
15	30	20	AlgY	57.3776	38.0508	0.0000
16	15	5	AlgY	56.0173	36.0266	0.0015

Response surface methodology (RSM) analysis of central composite design and model fitting were depicted in **Tables 5** and **6**. The experimental data, methane (CH_4), carbon dioxide (CO_2) and hydrogen sulphide (H_2S) in **Table 4** were utilized to develop the statistical model using multiple regression analysis fitting the quadratic model according to Equation (1). **Table 5** exhibited the fitted quadratic equation a significant model representing the relationships between H_2S and column length (X_1), acquisition time (X_2) and type of biosorbent (X_3). Among the tested model term H_2S depicted a significant response of the quadratic model with the *p*-value of 0.0006 suggesting a H_2S purification was significant at 95% (**Table 6**) in comparison to CH_4 and CO_2. Alginate-yeast (AlgY) recorded a *p*-value of < 0.0001 indicates the type of biosorbent is an importance factor which determine the biosorption efficiency. The relatively high correlation coefficient (R^2) of the tested quadratic model of all the responses were as follows; R^2 = 0.5560, 0.5048 and 0.9518 for CH_4, CO_2 and H_2S.

The Predicted R^2 of 0.7493 for H_2S is in reasonable agreement with the Adjusted R^2 of 0.8968 and the difference is less than 0.2. Whereby adequate precision measures the signal to noise ratio. A ratio greater than four (4) is desirable thus the ratio of 10.817 for H_2S indicates an adequate signal and suggested the model can be used to navigate the design space compared to CH_4 and CO_2 with recorded ratio of 3.6937 and 3.1679 respectively. Therefore, the H_2S results of the statistical analyses indicate the high adequacy of the tested quadratic model to represent the desired response of the parameter variables in this preliminary study of the biogas purification through biosorption with alginate-yeast biosorbent.

Table 5. The fitted model equations showing coefficients in terms of coded factors.

Response	Fitted model equation
H_2S	$0.0009 - 0.0002X_1 - 0.0001X_2 - 0.0016X_3 + 0.0001X_1X_2 - 0.0001X_1X_3 - 0.0001X_2X_3 + 0.0005X_1^2 + 0.0008X_2^2$

Table 6. Summary of analysis of variance (ANOVA) of fitted model.

Factors	Responses fitted to the quadratic model.					
	CH_4 (%)		CO_2 (%)		H_2S (ppm)	
	F-value	*p*-value	*F*-value	*p*-value	*F*-value	*p*-value
Model	1.10	0.4586	0.8919	0.5666	17.30	0.0006[Sig]
X_1-Column length	0.4902	0.5064	1.97	0.2030	2.30	0.1732
X_2-Acquisition time	0.0723	0.7958	0.6445	0.4485	0.2555	0.6288
X_3-Type of biosorbent	4.90	0.0625	1.56	0.2512	129.53	< 0.0001[Sig]
X_1X_2	0.1006	0.7604	0.2015	0.6671	0.1380	0.7213
X_1X_3	0.0159	0.9032	0.0056	0.9425	0.5007	0.5021
X_2X_3	0.1828	0.6818	0.8011	0.4005	0.0920	0.7705
X_1^2	0.8611	0.3843	1.06	0.3383	2.25	0.1770
X_2^2	1.15	0.3198	1.52	0.2578	4.91	0.0623
R^2	0.5560		0.5048		0.9518	
Adjusted R^2	0.0485		−0.0612		0.8968	
Predicted R^2	−1.3315		−1.3656		0.7493	
Adequate Precision	3.6937		3.1679		10.8167	

3.2. Effect of parameter variables on bead stability

The fitted quadratic equation of CH_4, CO_2 and H_2S were presented in response 3D surface plots as illustrated in **Figure 3a,b**, **Figure 4a,b** and **Figure 5a**,**b** to describe the relationship between the factors studied (column length, acquisition time, type of biosorbent). The interaction between sodium alginate and $CaCl_2$ solution, lead to a Ca^{2+} substitution with the Na^+ ions and later cross-interact with carboxylate groups (-COO-) and negatively polar groups (-OH) [23]. The process progressively integrates *Saccharomyces cerevisiae* into the gel formation. In addition, the yeast biomass was successfully encapsulated within the gel beads. The study applied the best reported conditions of sodium alginate and $CaCl_2$ concentrations, gelation time and mixing rpm from the published literature to obtain the beads stability. **Figure 3a,b** to **Figure 5a**,**b** illustrated the hydrogen sulphide, carbon dioxide and methane biosorption contour profile at different acquisition time and column length of alginate-yeast (AlgY) and Control respectively.

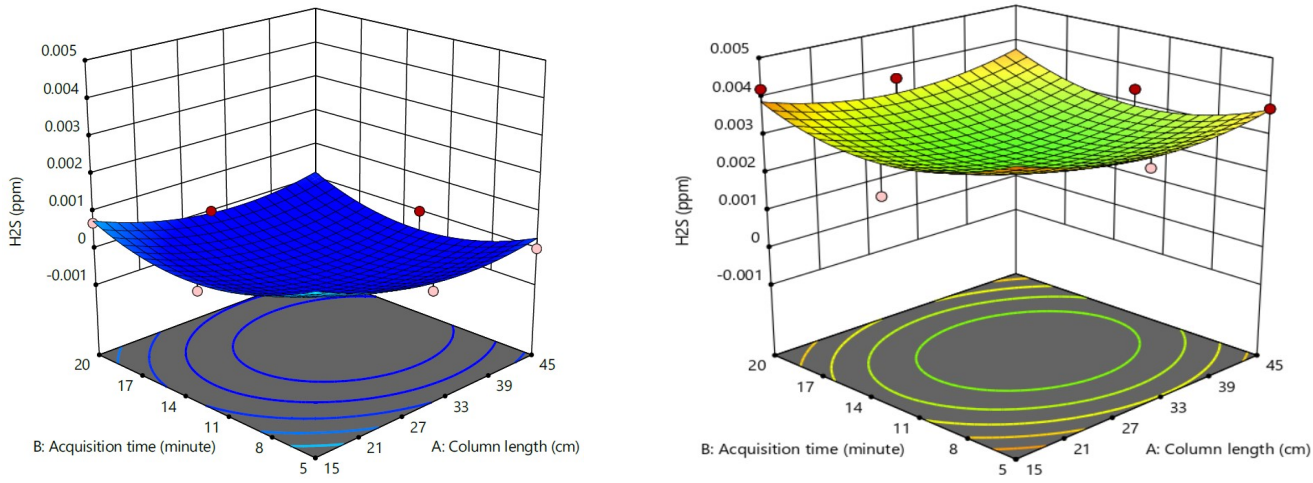

(a) **(b)**

Figure 3. Hydrogen sulphide biosorption contour profile at different acquisition time and column length. **(a)** AlgY; **(b)** control.

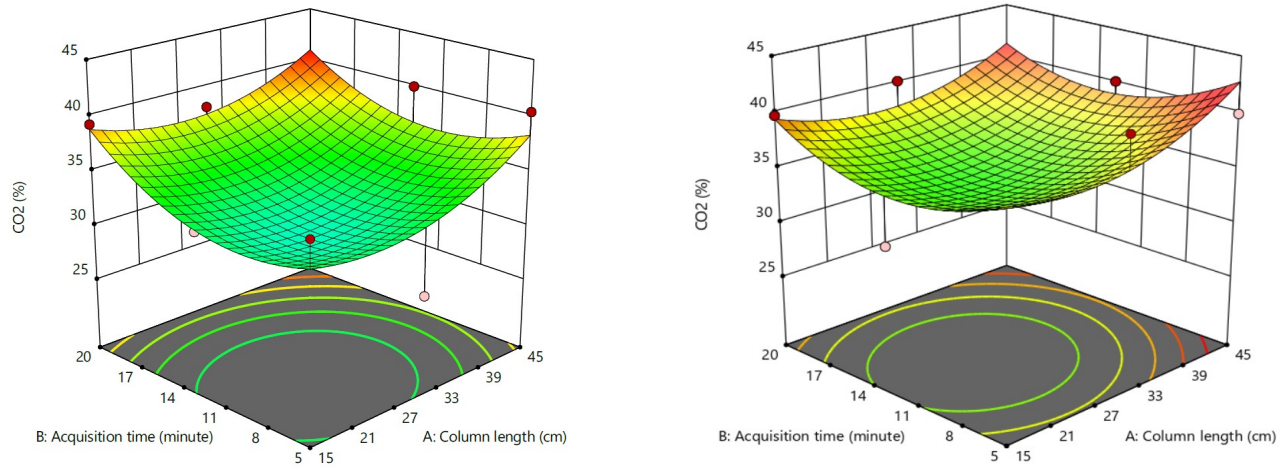

(a) **(b)**

Figure 4. Carbon dioxide biosorption contour profile at different acquisition time and column length. **(a)** AlgY; **(b)** control.

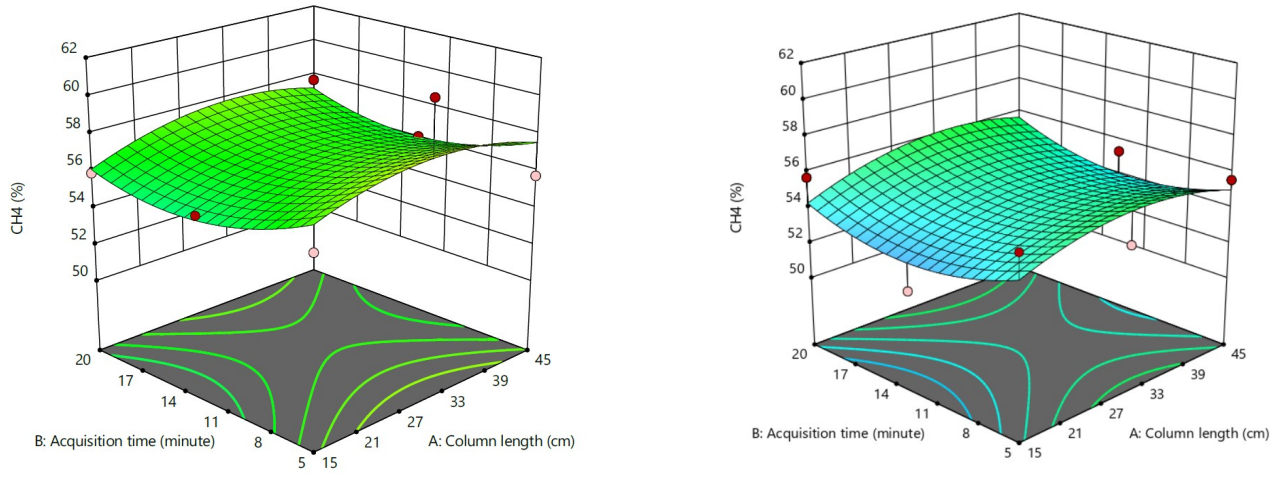

(a) **(b)**

Figure 5. Methane biosorption contour profile at different acquisition time and column length. **(a)** AlgY; **(b)** control.

The results exhibited the good absorption for H_2S compared to CO_2 and CH_4 with the encapsulated yeast beads as biosorbent. In addition, the effect of acquisition time and length of column insignificantly affected the biosorption and recommended further experiment should be incorporated the concentration of the encapsulated yeast biomass to correlate growth profile of the *Saccharomyces cerevisiae* during the biogas purification. The ANOVA of model terms in **Table 6** indicated only the factor of type of biosorbent represented a significant term ($p < 0.05$), suggesting the type of biosorbent variables of alginate bead could be considered to have a primary influence on gas biosorption. Varying a $CaCl_2$ and sodium alginate concentration will be added in the future work for cell encapsulation stability and efficiency.

4. Discussion

Alginate is presently employed across numerous industrial sectors, spanning biotechnology, bioengineering, biomedicine, clinical applications, pharmaceuticals, chemicals, textiles, packaging, construction, food and beverage production, aquaculture, dentistry, paper manufacturing, arts and crafts, as well as leisure activities [24]. Despite great potential in various applications, alginate exhibits some limitations especially when exposed to the physiological environment in sustaining the structure stability. As reported by [25] to address this issue, various materials have been introduced into the alginate structure, resulting in the formation of robust composite materials. For example, incorporating adhesive peptides, natural polymers, or synthetic polymers into alginate moieties yields an enhanced composite material. This material not only exhibits superior mechanical properties compared to native alginate but also offers additional healing capabilities and facilitates improved tissue regeneration for instance in medical applications and the food industry.

The reported findings additionally suggests that the carboxylic groups present on the surface of TEMPO-oxidized nanocellulose (TOCN) may contribute to the formation of the structure of alginate-based films. The enhanced insolubility and mechanical strength, coupled with the decreased water vapour permeability of the crosslinked films, could significantly broaden the utilization of polysaccharides in diverse applications, particularly in food packaging [26]. Cross-linking also significantly enhances mechanical properties, along with the use of suitable plasticizers, which enhance film flexibility and broaden their potential applications [27,28]. A notable feature of alginates is their ability to interact with multivalent metal cations, particularly calcium ions, which create linkages between MM and GG blocks of the polymer, resulting in a three-dimensional network [29–31].

The prevalent approach for removing hydrogen sulfide and carbon dioxide from gas entails subjecting natural gas to an alkaline solution. One widely recognized approach for hydrogen sulfide removal relies on the reaction between hydrogen sulfide and iron oxide, wherein the gas is directed through a bed of wood chips infused with iron oxide. Solid sorbents utilized in fixed bed reactors for H_2S capture can operate through two distinct mechanisms that is physisorption which weak bonds form between H_2S and the substrate. Chemisorption involves chemical bonds between the adsorbate and the substrate [32]. Biosorbents, originating from sustainable sources like plant-based materials, animal waste, and marine biomass,

can be conveniently tailored to enhance their adsorption capacity. This adaptability makes them exceptionally effective in tackling a wide range of pollutants [33,34]. Several studies have reported the biosorption efficiency of colour chemicals in textile wastewater using bacterial biomass [35]. The ability of bacterial biomass to adhere to dye particles is due to the presence of hydroxyl, carboxyl, amino, and phosphate groups within the peptidoglycan layer of the cell wall. As biosorption is a metabolically self-sufficient process, microbial cell growth does not necessitate additional nutrients. Utilizing a straightforward entrapment technique, Saccharomyces pastorianus, a representative yeast strain, was immobilized and subsequently microencapsulated in alginate for the purpose of eliminating cationic dye [36].

Numerous research groups have focused on employing the most prevalent biopolymers to adsorb hazardous heavy metal ions and other noxious pollutants. In recent studies, it has been found that the most effective polymers for adsorption are not cellulose or starch, but rather chitin, algae, and their primary derivatives, chitosan and alginate [37]. Among these polymers, alginate has garnered interest for its environmentally friendly nature and cost-effectiveness. Derived from brown algae, alginate can be readily shaped into beads or biofilm through uncomplicated immersion in a crosslinking agent, such as multi-valent cations. Typically, the process of alginate encapsulation includes forming spherical beads by introducing an alginate solution into a solution containing a crosslinking agent [38]. While alginate encapsulation offers numerous advantages, it has not been applied as an encapsulation polymer for dry yeast clay, specifically Saccharomyces cerevisiae, in the context of atmospheric pollutant adsorption.

Encapsulated cells experience restrained replication, enhancing their ability to convert substrate into product more efficiently compared to planktonic cells. This limited replication also contributes to their increased stress resistance [39]. Typically, encapsulated cells demonstrate higher product yields than planktonic cells, as they direct less substrate toward the generation of new biomass [40]. This efficiency enables them to process feedstock more effectively. Additionally, alginate beads exhibit good reusability, maintaining their performance even after undergoing five rounds of simple sorption–desorption procedures.

Biosorption of alginate derived from brown algae widely employed for heavy metals removal in polluted water. The sodium alginate biosorbent possess high affinity through gelation [41] and rich in functional groups like carboxyl and hydroxyl, can effectively crosslink with cations [42]. The carboxyl group's negative nature allows for electrostatic adsorption with heavy metal ions, leading to chelation simultaneously [43]. In other reported study Ca-alginate beads was addressed to portray a biodegradable property. They exhibit significant efficacy in removing uranium and thorium ions with high capacity, presenting a promising alternative for the biosorption of radionuclides from waste streams [44]. Thus, the efficacy of the biopolymers has yet to be explored to achieve sufficient selectivity for toxic gases abatement and gas purification.

The limitation on using calcium alginate matrices for encapsulating cells in wastewater pollution abatement may stem from the existence of elevated concentrations of dissolved monovalent cations (mainly Na^+, K^+, and Mg^{2+}) in

high-salt effluents. These cations have the potential to displace divalent cations, ultimately causing the degradation of the polymer matrix structure [45]. Typically, the formation of a three-dimensional polymer network is facilitated by the ionic interaction between alginate chains and calcium ions [46]. Strategies such as modification, immobilization, or encapsulation using various organic or inorganic materials could enhance the selectivity and stability of Ca-alginate beads. These microorganisms exhibit remarkable pollutant uptake capabilities, can self-regenerate, and incur minimal operational costs. Moreover, Versatility in utilizing a diverse range of carbon or nitrogen sources is evident in both pure and mixed bacterial cultures [47]. Finally, this study demonstrated the potential application of the dual function of biological biomass (i) biofilter and (ii) biosorbent incorporated with natural polymers suggestting a viable green material for pollution abatement that is able to minimize the carbon footprint. The possible mechanism of the AlgY absorbent in reducing the H_2S concentration is through the alteration of H_2S biogas to act as a signaling molecule. The signalling molecule promotes the growth of yeast. Gu et al. [48] reported the effect of the phenotypic or transcriptomic alternations on the fungal growth enhancement by H_2S is exhibited in the intracellular association of H_2S in their findings.

5. Conclusion

This research employs RSM to assess alginate-yeast (AlgY) performance under varying experimental conditions, bridging existing gaps in biosorption efficiency studies. The overall preliminary findings of AlgY as a biosorbent for biogas reduction especially for H_2S, reveal a positive potential application and can be explored further. The significance of the screening model of AlgY biosorbent depicted the type of biosorbent variables of alginate bead influence the biogas sorption. The results exhibited the potential of AlgY for biogas purification, achieving significant H_2S removal ($R^2 = 0.9518$, $p < 0.0001$). Hydrogen sulfide (H_2S) is a common contaminant in biogas that poses environmental and operational challenges. Biosorbents such as alginate-yeast (AlgY) have gained attention due to their biodegradability, cost-effectiveness, and potential for gas purification however this preliminary work can be further explored to determine the compositions of the spent AlgY biosorbent. The spent AlgY biosorbent composition analyses will lead to the understanding of the H_2S reduction mechanism as well as CO_2 and CH_4 responses. AlgY offers a potentially sustainable alternative to traditional chemical-based methods and, open path for the physico-chemical and biological-based reaction mechanisms. The preliminary findings of the study are unable to explain the reduction mechanism of the tested gaseous which reflected the high removal efficiencies reported for H_2S. It is best to run the Langmuir and Freundlich isotherms study to estimate the adsorption capacity of the AlgY biosorbent. Transmission electron microscopy (TEM) and scanning electron microscopy (SEM) can be used to further visualize any changes in the internal and surface structure of the AlgY biosorbent.

6. Recommendation

Varying a $CaCl_2$ and sodium alginate concentration can be considered in future work for cell encapsulation stability and efficiency. This can be entailed and explored in (i) optimizing $CaCl_2$ and sodium alginate concentrations to improve biosorption, (ii) exploring alternative crosslinking agents like iron and (iii) evaluating the economic feasibility of scaling up AlgY biosorbents.

Author contributions: Conceptualization, NI and BC; methodology and formal analysis, NI and BC; resources, JM and HO; writing—original draft preparation, NI; writing—review and editing, NI and JM. All authors have read and agreed to the published version of the manuscript.

Acknowledgments: The authors would like to express their appreciation to German Academic Exchange Service (DAAD): Research Stays for University Academics and Scientists, 2023 (57681226).

Conflict of interest: The authors declare no conflict of interest.

References

1. Boudria A, Hammoui Y, Adjeroud N, et al. Effect of filler load and high-energy ball milling process on properties of plasticized wheat gluten/olive pomace biocomposite. Advanced Powder Technology. 2018; 29(5): 1230-1238. doi: 10.1016/j.apt.2018.02.015
2. Nataraj D, Sakkara S, HN M, et al. Properties and applications of citric acid crosslinked banana fibre-wheat gluten films. Industrial Crops and Products. 2018; 124: 265-272. doi: 10.1016/j.indcrop.2018.07.076
3. Ciapponi R, Turri S, Levi M. Mechanical Reinforcement by Microalgal Biofiller in Novel Thermoplastic Biocompounds from Plasticized Gluten. Materials. 2019; 12(9): 1476. doi: 10.3390/ma12091476
4. Madhu P, Sanjay MR, Senthamaraikannan P, et al. A review on synthesis and characterization of commercially available natural fibers: Part-I. Journal of Natural Fibers. 2018; 16(8): 1132-1144. doi: 10.1080/15440478.2018.1453433
5. Rohan T, Tushar B, G T M. Review of natural fiber composites. IOP Conference Series: Materials Science and Engineering. 2018; 314: 012020. doi: 10.1088/1757-899x/314/1/012020
6. Wu Y, Li B, Miao B, et al. Saccharomyces cerevisiae employs complex regulation strategies to tolerate low pH stress during ethanol production. Microbial Cell Factories. 2022; 21(1). doi: 10.1186/s12934-022-01974-3
7. Gu Z, Sun Y, Wu F, et al. Mechanism of Growth Regulation of Yeast Involving Hydrogen Sulfide From S-Propargyl-Cysteine Catalyzed by Cystathionine-γ-Lyase. Frontiers in Microbiology. 2021; 12. doi: 10.3389/fmicb.2021.679563
8. Baş D, Boyacı İH. Modeling and optimization I: Usability of response surface methodology. Journal of Food Engineering. 2007; 78(3): 836-845. doi: 10.1016/j.jfoodeng.2005.11.024
9. Bierbaumer S, Nattermann M, Schulz L, et al. Enzymatic Conversion of CO2: From Natural to Artificial Utilization. Chemical Reviews. 2023; 123(9): 5702-5754. doi: 10.1021/acs.chemrev.2c00581
10. Zhang H, Zhang T, Zang J, et al. Construction of alginate beads for efficient conversion of CO2 into vaterite CaCO3 particles. Food Hydrocolloids. 2022; 130: 107693. doi: 10.1016/j.foodhyd.2022.107693
11. Wu S, Chen J, Ma L, et al. Design of carbonic anhydrase with improved thermostability for CO2 capture via molecular simulations. Journal of CO2 Utilization. 2020; 38: 141-147. doi: 10.1016/j.jcou.2020.01.017
12. Qian C, Ren X, Rui Y, et al. Characteristics of bio-CaCO3 from microbial bio-mineralization with different bacteria species. Biochemical Engineering Journal. 2021; 176: 108180. doi: 10.1016/j.bej.2021.108180
13. Nikolaivits E, Pantelic B, Azeem M, et al. Progressing Plastics Circularity: A Review of Mechano-Biocatalytic Approaches for Waste Plastic (Re)valorization. Frontiers in Bioengineering and Biotechnology. 2021; 9. doi: 10.3389/fbioe.2021.696040
14. El-Sherif DM, Eloffy MG, Elmesery A, et al. Environmental risk, toxicity, and biodegradation of polyethylene: a review. Environmental Science and Pollution Research. 2022; 29(54): 81166-81182. doi: 10.1007/s11356-022-23382-1

15. Crini G, Lichtfouse E, Wilson LD, et al. Conventional and non-conventional adsorbents for wastewater treatment. Environmental Chemistry Letters. 2018; 17(1): 195-213. doi: 10.1007/s10311-018-0786-8
16. Gadd GM. Biosorption: critical review of scientific rationale, environmental importance and significance for pollution treatment. Journal of Chemical Technology & Biotechnology. 2008; 84(1): 13-28. doi: 10.1002/jctb.1999
17. Vijayaraghavan K, Balasubramanian R. Is biosorption suitable for decontamination of metal-bearing wastewaters? A critical review on the state-of-the-art of biosorption processes and future directions. Journal of Environmental Management. 2015; 160: 283-296. doi: 10.1016/j.jenvman.2015.06.030
18. Aksu Z. Application of biosorption for the removal of organic pollutants: a review. Process Biochemistry. 2005; 40(3-4): 997-1026. doi: 10.1016/j.procbio.2004.04.008
19. Lim AP, Aris AZ. A review on economically adsorbents on heavy metals removal in water and wastewater. Reviews in Environmental Science and Bio/Technology. 2013; 13(2): 163-181. doi: 10.1007/s11157-013-9330-2
20. Ong ST, Keng PS, Lee SL, et al. Low Cost Adsorbents for Sustainable Dye Containing-Wastewater Treatment. Asian Journal of Chemistry. 2014; 26(7): 1873-1881. doi: 10.14233/ajchem.2014.15653
21. Gupta VK, Nayak A, Agarwal S. Bioadsorbents for remediation of heavy metals: Current status and their future prospects. Environmental Engineering Research. 2015; 20(1): 1-18. doi: 10.4491/eer.2015.018
22. Soo CL, Chen CA, Bojo O, et al. Feasibility of Marine Microalgae Immobilization in Alginate Bead for Marine Water Treatment: Bead Stability, Cell Growth, and Ammonia Removal. International Journal of Polymer Science. 2017; 2017: 1-7. doi: 10.1155/2017/6951212
23. Touloupakis E, Rontogiannis G, Silva Benavides AM, et al. Hydrogen production by immobilized Synechocystis sp. PCC 6803. International Journal of Hydrogen Energy. 2016; 41(34): 15181-15186. doi: 10.1016/j.ijhydene.2016.07.075
24. Hurtado A, Aljabali AAA, Mishra V, et al. Alginate: Enhancement Strategies for Advanced Applications. International Journal of Molecular Sciences. 2022; 23(9): 4486. doi: 10.3390/ijms23094486
25. Ahmad Raus R, Wan Nawawi WMF, Nasaruddin RR. Alginate and alginate composites for biomedical applications. Asian Journal of Pharmaceutical Sciences. 2021; 16(3): 280-306. doi: 10.1016/j.ajps.2020.10.001
26. Xiao J, Zhao K, Tian X, et al. Impact of calcium-carboxylate interactions in cellulose nanofiber reinforced alginate based film with triple-decker-like structure. LWT. 2021; 151: 112197. doi: 10.1016/j.lwt.2021.112197
27. Russo R, Malinconico M, Santagata G. Effect of Cross-Linking with Calcium Ions on the Physical Properties of Alginate Films. Biomacromolecules. 2007; 8(10): 3193-3197. doi: 10.1021/bm700565h
28. Zhao Y, Qiu J, Xu J, et al. Effects of crosslinking modes on the film forming properties of kelp mulching films. Algal Research. 2017; 26: 74-83. doi: 10.1016/j.algal.2017.07.006
29. Li D, Wei Z, Xue C. Alginate-based delivery systems for food bioactive ingredients: An overview of recent advances and future trends. Comprehensive Reviews in Food Science and Food Safety. 2021; 20(6): 5345-5369. doi: 10.1111/1541-4337.12840
30. Girón-Hernández J, Gentile P, Benlloch-Tinoco M. Impact of heterogeneously crosslinked calcium alginate networks on the encapsulation of β-carotene-loaded beads. Carbohydrate Polymers. 2021; 271: 118429. doi: 10.1016/j.carbpol.2021.118429
31. Senturk Parreidt T, Müller K, Schmid M. Alginate-Based Edible Films and Coatings for Food Packaging Applications. Foods. 2018; 7(10): 170. doi: 10.3390/foods7100170
32. Georgiadis A, Charisiou N, Goula M. Removal of Hydrogen Sulfide From Various Industrial Gases: A Review of The Most Promising Adsorbing Materials. Catalysts. 2020; 10(5): 521. doi: 10.3390/catal10050521
33. Crini G, Torri G, Lichtfouse E, et al. Dye removal by biosorption using cross-linked chitosan-based hydrogels. Environmental Chemistry Letters. 2019; 17(4): 1645-1666. doi: 10.1007/s10311-019-00903-y
34. Osman AI, Farrell C, Al-Muhtaseb AH, et al. The production and application of carbon nanomaterials from high alkali silicate herbaceous biomass. Scientific Reports. 2020; 10(1). doi: 10.1038/s41598-020-59481-7
35. Ellafi A, Dali A, Mnif S, et al. Microbial Enzymatic Degradation, Spectral Analysis and Phytotoxicity Assessment of Congo Red Removal By Bacillus spp. Catalysis Letters. 2023; 153(12): 3620-3633. doi: 10.1007/s10562-023-04272-8
36. Blaga AC, Zaharia C, Suteu D. Polysaccharides as Support for Microbial Biomass-Based Adsorbents with Applications in Removal of Heavy Metals and Dyes. Polymers. 2021; 13(17): 2893. doi: 10.3390/polym13172893
37. Benettayeb A, Ghosh S, Usman M, et al. Some Well-Known Alginate and Chitosan Modifications Used in Adsorption: A Review. Water. 2022; 14(9): 1353. doi: 10.3390/w14091353
38. He Y, Zhang N, Gong Q, et al. Alginate/graphene oxide fibers with enhanced mechanical strength prepared by wet spinning.

Carbohydrate Polymers. 2012; 88(3): 1100-1108. doi: 10.1016/j.carbpol.2012.01.071

39. Gulli J, Yunker P, Rosenzweig F. Matrices (re)loaded: Durability, viability, and fermentative capacity of yeast encapsulated in beads of different composition during long-term fed-batch culture. Biotechnology Progress. 2019; 36(1). doi: 10.1002/btpr.2925
40. Moreno-García J, García-Martínez T, Mauricio JC, et al. Yeast Immobilization Systems for Alcoholic Wine Fermentations: Actual Trends and Future Perspectives. Frontiers in Microbiology. 2018; 9. doi: 10.3389/fmicb.2018.00241
41. Gao X, Guo C, Hao J, et al. Adsorption of heavy metal ions by sodium alginate based adsorbent-a review and new perspectives. International Journal of Biological Macromolecules. 2020; 164: 4423-4434. doi: 10.1016/j.ijbiomac.2020.09.046
42. Feng Y, Wang Y, Wang Y, et al. In-situ gelation of sodium alginate supported on melamine sponge for efficient removal of copper ions. Journal of Colloid and Interface Science. 2018; 512: 7-13. doi: 10.1016/j.jcis.2017.10.036
43. Rusu L, Suceveanu EM, Blaga AC, et al. Insights into Recent Advances of Biomaterials Based on Microbial Biomass and Natural Polymers for Sustainable Removal of Pharmaceuticals Residues. Polymers. 2023; 15(13): 2923. doi: 10.3390/polym15132923
44. Kumar M, Seth A, Singh AK, et al. Remediation strategies for heavy metals contaminated ecosystem: A review. Environmental and Sustainability Indicators. 2021; 12: 100155. doi: 10.1016/j.indic.2021.100155
45. Voo WP, Ravindra P, Tey BT, et al. Comparison of alginate and pectin based beads for production of poultry probiotic cells. Journal of Bioscience and Bioengineering. 2011; 111(3): 294-299. doi: 10.1016/j.jbiosc.2010.11.010
46. Klokk TI, Melvik JE. Controlling the size of alginate gel beads by use of a high electrostatic potential. Journal of Microencapsulation. 2002; 19(4): 415-424. doi: 10.1080/02652040210144234
47. Shabir M, Yasin M, Hussain M, et al. A review on recent advances in the treatment of dye-polluted wastewater. Journal of Industrial and Engineering Chemistry. 2022; 112: 1-19. doi: 10.1016/j.jiec.2022.05.013
48. Gu Z, Sun Y, Wu F, et al. Corrigendum: Mechanism of Growth Regulation of Yeast Involving Hydrogen Sulfide From S-Propargyl-Cysteine Catalyzed by Cystathionine-γ-Lyase. Frontiers in Microbiology. 2021; 12. doi: 10.3389/fmicb.2021.761240

Materials Technology Reports 2024, 2(2), 1879.
https://doi.org/10.59400/mtr1879

Review

Energy systems and green sourced nanomaterials—A today's outlook

Ayesha Kausar

National Center for Physics, Quaid-i-Azam University Campus, Islamabad 45320, Pakistan; asheesgreat@yahoo.com

CITATION

Kausar A. Energy systems and green sourced nanomaterials—A today's outlook. Materials Technology Reports. 2024; 2(2): 1879. https://doi.org/10.59400/mtr1879

ARTICLE INFO

Received: 17 October 2024
Accepted: 7 November 2024
Available online: 20 November 2024

Abstract: Owing to current growing demands of environmental friendly energy devices, innumerable green materials/nanomaterials have been applied to design the desired high tech devices. Amongst energy devices, supercapacitors have been ranked distinctively for efficient energy storage competence. Principally, green nanocomposites derived from green or ecological polymers and green nanoparticles have been scrutinized for supercapacitor components. Concerning this, current review has been planned to sketch the energy storage application of green nanocomposites, predominantly for supercapacitors. In this concern, mostly synthetic green polymers (such as polyaniline, polypyrrole, etc.) and their blends with natural polymers (like chitosan) having fine biodegradability, non-toxicity, low cost, and superior device end performance have been found as the noteworthy materials. Additionally, green nanofillers like carbon nanoparticles (carbon nanotube, graphene, etc.) and metal nanoparticles have been processed with green polymers via ecological techniques, like in situ, solution, sonication, mixing, hydrothermal, exfoliation, reduction, etc., to form the anticipated energy device components. In consequence, the designed ecological nanocomposites expectedly had the advantages of low price/weight, superior mechanical/heat resilience, electron transference, capacitance, power/charge density, charge-discharge, sustainability as well as environmentally friendliness for energy related methodological systems. Incidentally, the design and performance challenges towards the application of ecological nanocomposites in energy storage devices have been conversed.

Keywords: green; polymer; nanofiller; nanocomposite; supercapacitor; environmental; high performance

1. Introduction

With the advancements in the materials and nanotechnological breakthroughs, green materials/nanomaterials having facile biodegradability and sustainability features have been the focus of recent technical researches [1,2]. For nanocomposites, essential environmental materials like natural or synthetic green polymers have been investigated as matrix materials [3,4]. Further, numerous nanoparticles of inorganic (metal, ceramics) and organic (carbon, polymers) types have been studied for advanced green nanocomposites [5]. In consequence, the nanocomposites designed from green matrices and nanofillers have been reported for valuable structural, mechanical, biodecomposibility, and sustainability features for progressive applications [6,7]. Besides, one important aspect of the green nanomaterials has been identified as the utilization of environmentally safe processing techniques to avoid any probable green house effects [8]. Ultimately, carefully designed green nanocomposites have been scrutinized for demanding industrial level employments, including energy sector, electronics, engineering, biomedical, etc. [9]. Use of environmentally safe nanomaterials have recently gained much curiosity in the energy/electronics fields [10]. In this concern, various combinations of eco polymers and eco nanoparticles

have been focused for advanced energy devices and systems [11]. Furthermore, use of advanced green synthesis techniques has been engrossed to form the green nanomaterials for high tech energy applications [12]. Especially, in the field of energy storing devices, like supercapacitors, interesting field researches have been observed concentrating the use of green nanomaterials, instead of traditional non-ecological materials designs in practice [13,14].

Accordingly, disciplined research attempts have been observed for the synthesis of ecological or green materials or nanocomposites for energy storage devices [15]. For example, research reports have been detected on conducting polymers and graphene-based nanomaterials using green methods for supercapacitor electrodes having environmental friendliness, low price, superior surface area, capacitance, and charge-discharge properties [16]. Lots of attempts have been reported in recent years (2020–2024) on supercapacitor electrodes derived from conducting polymers (polyaniline, polypyrrole, polythiophene, and polythiophene) and carbon nanoparticles with sustainability and ecofriendliness for application in supercapacitor electrodes [17,18]. Çıplak et al. [19] formed ecological polyaniline/graphene/gold nanoparticles, by green in situ polymerization method, for supercapacitor electrode applications. Consequently, the environmentally friendly supercapacitor electrode showed reasonable specific capacitance of 212.8 Fg^{-1}. In recent years, Arthisree et al. [20] formed environmentally friendly high performance supercapacitor electrodes using polyacrylonitrile, polyaniline, and quantum dots. Consequently, the polyacrylonitrile/polyaniline/quantum dot nanocomposite showed high specific capacitance of up to 600 Fg^{-1}. More recently, Zhao et al. [21] used carboxyl substituted dipyridophenazine and MXene based green nanocomposites to design electrodes for efficient energy storing devices. The resulting nanomaterial had reasonably high reversible capacity of 172.6 mAh cm^{-3} in 4000 cyclic performances. The carboxyl substituted dipyridophenazine/MXene were suggested for ecofriendly flexible portable energy storing device applications. Hence, lots of recent researches have been seen on the green and sustainable nanocomposite electrodes for environmentally friendly charge storage devices [22].

Along these lines, this novel review has thrown light upon the existing designs and demanding necessities regarding the implementations of green nanocomposites for energy storage systems. In this concern, essential green polymers and nanofiller based designs have been argued here. Effectiveness of green nanomaterials to attain low weight, cheap, robust, and sustainable green supercapacitor components, having high specific capacitance, power/charge density, recyclability, etc., have been surveyed for commercial energy devices applications. It seems that future of energy storage systems, like supercapacitors, relies upon more precise research endeavors to identify high-tech green/sustainable designs having least processing and performance related challenges.

2. Concept of green polymers, nanofillers and nanocomposites

Recognition of natural or green polymers can be related to centuries back with the wood, cotton, and natural rubber like materials [23,24]. Later, natural green polymers like cellulose, chitosan, starch, nylons, etc. and synthetic green polymers

like poly (vinyl alcohol), poly (ethylene glycol), poly (lactic acid), etc., have been foreseen [25,26]. Green polymers usually own biodegradability, sustainability, and environmentally friendly features [27,28]. Moreover, synthetic green polymers must be processed via ecological routes to maintain the environmental demands [29]. Further, green polymers have been observed practically beneficial for a number of industrial applications due to their increasing demand for engineering structures, adhesive/coating, and biomedical industries [30–32]. Besides, for reinforcing green polymeric matrices, numerous ecologically beneficial green nanofillers have been adopted including the polymeric nanoparticles, metal nanoparticles, carbon nanoparticles, and inorganic nanoparticles like nanoclays [33–35]. **Figure 1** shows few examples of essential ecological or green nanoparticles and also the green polymers used for environmentally friendly nanocomposites.

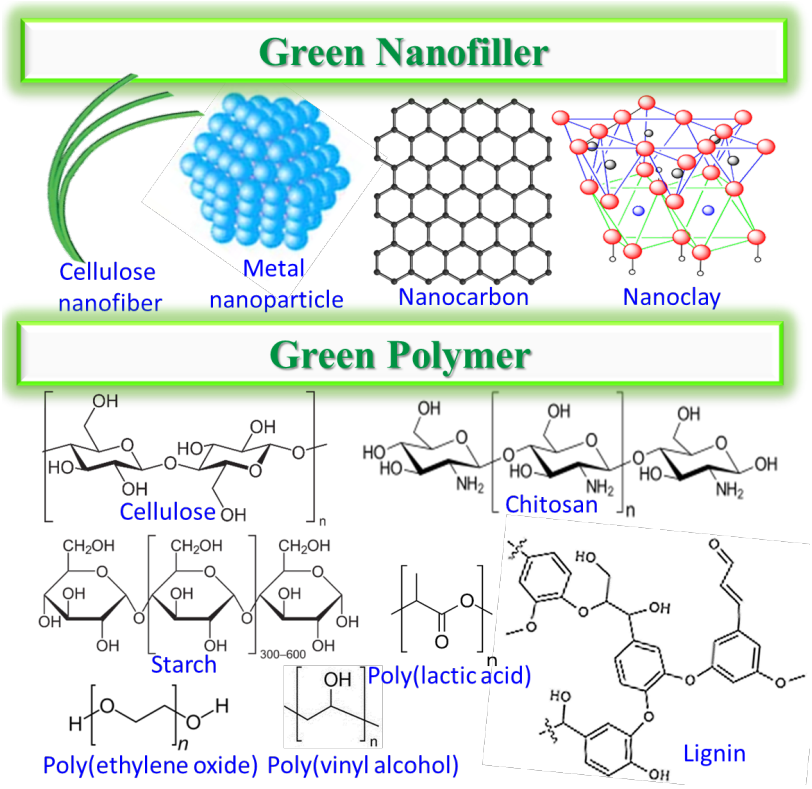

Figure 1. Few green polymers and green nanofillers.

For green nanocomposites, starch has been adopted as a low-cost natural polymer having facile biodegradation and environmentally friendly nature [36,37]. For example, Cheviron et al. [38] formed green nanocomposites based on starch and silver nanoparticles and explored for antimicrobial packaging applications. Similarly, the nanocomposites of lignin, cellulose, and allied natural green polymers have been reported [39,40].

Chitosan is an important green polymer used as matrix material for nanocomposites [41]. Regarding green metal nanoparticle-based system, Hashem et al. [42] prepared the chitosan/gold nanoparticle hybrid using a green chemical reduction method. **Figure 2A** shows the transmission electron microscopy image of the chitosan/gold nanoparticle hybrid having gold nanoparticles of sizes in the range of

20–120 nm in the matrix. **Figure 2B** depicts the particle size distribution of the chitosan/gold nanoparticle hybrid with average nanoparticle sizes of ~ 200 nm, owing to the insertion in the polymeric matrix and coating with the polymer. In addition, **Figure 2C** shows the X-ray diffraction patterns of the chitosan/gold nanoparticle hybrid with characteristic diffraction peaks for chitosan (22.8°) and gold nanoparticle peaks at 37.9° and 44.1°–77.4° due to crystallinity of the nanocomposite sample. Carlo et al. [43] also loaded gold nanoparticles in chitosan matrix using a green solution route based on $HAuCl_4$ salt and caffeic acid. The chitosan/gold nanoparticle nanocomposites had fine biodegradability and biocompatibility features.

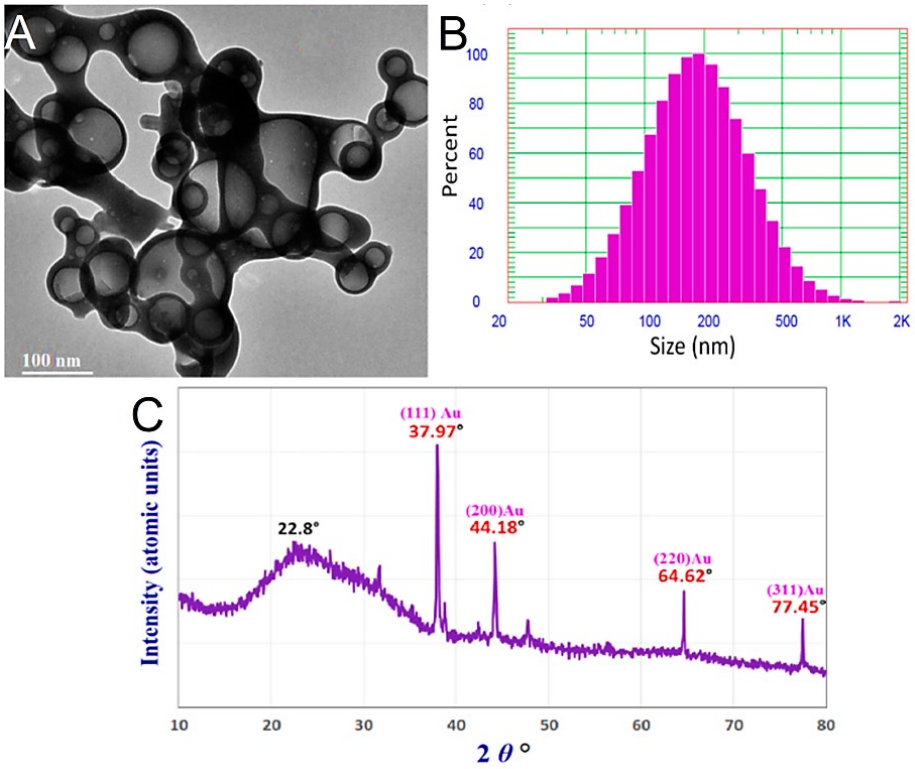

Figure 2. (A) Transmission electron microscopy image of the chitosan/gold nanoparticle hybrid; **(B)** particle size distribution of the chitosan/gold nanoparticle hybrid; **(C)** X-ray diffraction patterns of the chitosan/gold nanoparticle hybrid [42]. Reproduced with permission from MDPI.

Poly (ethylene glycol) is a synthetic green polymer having water solubility, biodegradability, and non-toxicity properties and it is widely applied as a matrix for nanofillers [44]. Including metal nanoparticles or carbon nanofillers in poly (ethylene glycol) matrix has been found to enhance the heat stability and mechanical properties of the resulting nanomaterials [45]. For example, Nguyen et al. [46] applied green plasma assisted chemical reduction approach for the formation of the poly (ethylene glycol) functional gold nanoparticle nanocomposite. **Figure 3A** shows a simple synthetic process for plasma assisted formation of the poly (ethylene glycol) functional gold nanoparticle nanocomposite. The as prepared poly (ethylene glycol) functional gold nanoparticle sample was scanned for the scanning electron microscopy images of different resolutions, as given in **Figure 3B,C**. According to the micrographs, gold nanoparticles had fine dispersions in the polymer and own uniform

quasi spherical shapes.

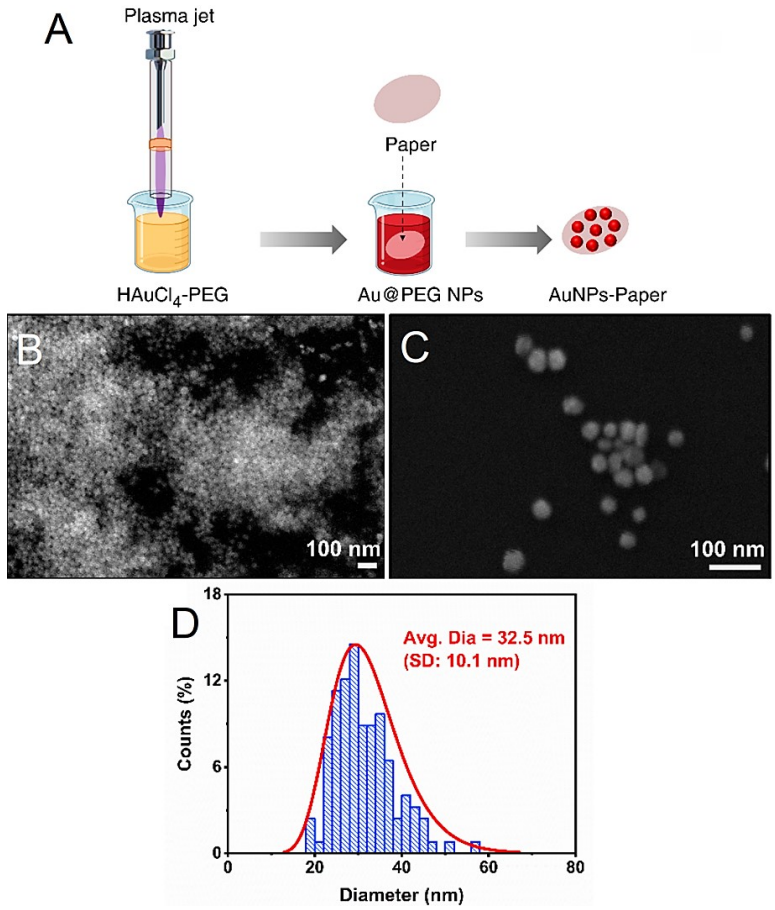

Figure 3. (A) Process for the plasma assisted synthesis of poly (ethylene glycol) functional gold nanoparticles (Au@PEG NPs); scanning electron microscopy images of Au@PEG NPs: **(B)** at 60,000 × resolution; and **(C)** at 160,000 × resolution; **(D)** the particle size distribution of Au@PEG NPs, with average particle size of 32.5 nm (standard deviation, SD, of 0.1 nm [46].
Reproduced with permission from MDPI.

Figure 3D illustrates the particle size distribution plots of the poly (ethylene glycol) functional gold nanoparticles obtained by Image J software showing a uniform symmetrical gold nanoparticle distribution and average size of around 32.5 nm. These results indicated the success of the green plasma-based technique applied to form the green poly (ethylene glycol)/gold nanoparticle hybrids. Similarly, countless reports have been observed on the poly (ethylene glycol) hybrids, e.g., the poly (ethylene glycol)/halloysite nanotubes [47], poly (ethylene glycol)/turmeric nanofibers [48], poly (ethylene oxide)/silver nanoparticles [49], poly (ethylene oxide)/silica nanoparticles [50] for applications in devices, packaging, antimicrobials, and biomedical fields [51].

Among other metal (gold/silver nanoparticles) or inorganic nanoparticles (nanoclays) filled green hybrids, poly (vinyl alcohol) [52–54] and poly (lactic acid) [55–57] based nanomaterials have been reported for low cost, fine biodegradability, non-lethality, and environmentally friendliness for wide ranging applications as antibacterial, wound healing, biomedical, and technical relevance.

Besides, various nanocarbons including carbon nanotube, graphene, graphene oxide, and other modified graphene forms have been applied as beneficial nanofillers for the formation of the green polymers and nanocomposites.

3. Green nanocomposites for energy systems

Concept of using green or ecological materials can be related to the ancient development of wind turbine blades using natural composites, instead of heavy metal-based structures [58]. Further research efforts on ecological composites exposed uses in sophisticated devices, like optoelectronics [59]. Similarly, numerous environmental materials, e.g., natural polymer, have been recognized with the potential for energy conversion systems, like batteries [60]. Consequently, natural/green polymers and related materials have been explored for light emitting diodes [61], solar cell devices [62], thermoelectric generators [63], and related thermoelectric devices [64]. In these systems, green polymers have been suggested to develop donor-acceptor type associations for energy conversion purposes [65]. Incidentally, the optical, electron conduction, and energy conversion features of these ecological materials depicted their demand in today's high-tech energy conversion systems, like supercapacitors.

Among efficient energy conversion systems, supercapacitors have been enormously focused by the researchers due to high energy outputs [66]. Advancements in the field of supercapacitors have devised the use of effective green materials, such as polymers, composites, and nanocomposites [67]. Consequently, green or ecological polymers, natural fillers, green or green derived nanoparticles have been investigated to form the ecological composites and nanocomposite designs for energy storage devices [68]. In this concern, ecofriendly/green synthesis methods have also been studied for the formation of environmentally safe materials or nanomaterials [69].

Out of huge variety of polymers, naturally occurring and synthetic polymers having ecofriendly, biodegradability, and sustainability properties have been focused for green energy applications [70]. Few examples may include cellulose, chitosan, chitin, lignin, starch, and countless other eco polymers [71]. Particularly, for supercapacitor electrodes, natural/green polymers offer the advantages of facile processing and superior performance, in addition to sustainability aspects [72]. Despite of using green polymers, several non-green materials have been processed using ecological routes to attain environmentally safe materials for supercapacitors or energy devices [73].

For superior supercapacitor device performance, green polymers have been converted to green nanocomposite by adopting several inorganic (metal nanoparticles or metal oxide nanoparticles) and carbon nanomaterials [74,75]. Amidst carbon nanoparticles, carbon nanotube, graphene, and modified carbon nanotube or graphene nanostructures have been investigated [76]. Additionally, use of green methods with safe chemical and reagents have been practiced to form the desired ecological nanocomposite for energy storage [77].

4. Green energy devices—Supercapacitors

For energy devices, carbon nanoparticles have been processed with polymers or inorganic matrices via environmentally safe chemicals and methods to attain the desired ecological device materials [76]. In this way, use of hazardous organic solvents and reagents can be avoided to form green nanocomposites [78]. Subsequently, researchers are continuously struggling to fabricated advanced supercapacitor devices with high capacitance, power density, and cyclic performance using green polymers, green nanocarbons, and green synthesis routes [79].

Carbon nanotube based green nanocomposites have been reported for supercapacitor assemblies [80]. Here, Jyothibasu et al. [81] used modest low cost in situ chemical polymerization, sonication, and filtration routes to form green polypyrrole/kapok fiber/carbon nanotube nanocomposite. **Figure 4A** shows the cyclic voltametric curves of the polypyrrole/kapok fiber/carbon nanotube nanocomposite, which was bent at several angles of 0° to 180° (40 mV s^{-1}). The obtained nanocomposite based flexible supercapacitor is also shown as an inset with digital photograph in bent form. The nanocomposite-based supercapacitor electrode had symmetric cyclic performance in cyclic voltametric curves. **Figure 4B** displays electrochemical impedance spectroscopy spectra of the polypyrrole/kapok fiber/carbon nanotube nanocomposite based flexible supercapacitor at various bending angles. The results showed an increase in the areal capacitance from 128.4 mF cm^{-2} (0°) to 139.4 mF cm^{-2} (180°). Ultimately, the polypyrrole/kapok fiber/carbon nanotube nanocomposites connected in series were used to light the red-light emitting diode, as given in **Figure 4C**. Moreover, the polypyrrole/kapok fiber/carbon nanotube nanocomposite based flexible solid state symmetric supercapacitor had constant cycling stability over 2500 cycles (25 mA cm^{-2}) and capacitance retention of 97.4% (**Figure 4D**). Hence, low price, green and sustainable high performance flexible polypyrrole/kapok fiber/carbon nanotube nanocomposite-based supercapacitor has been developed.

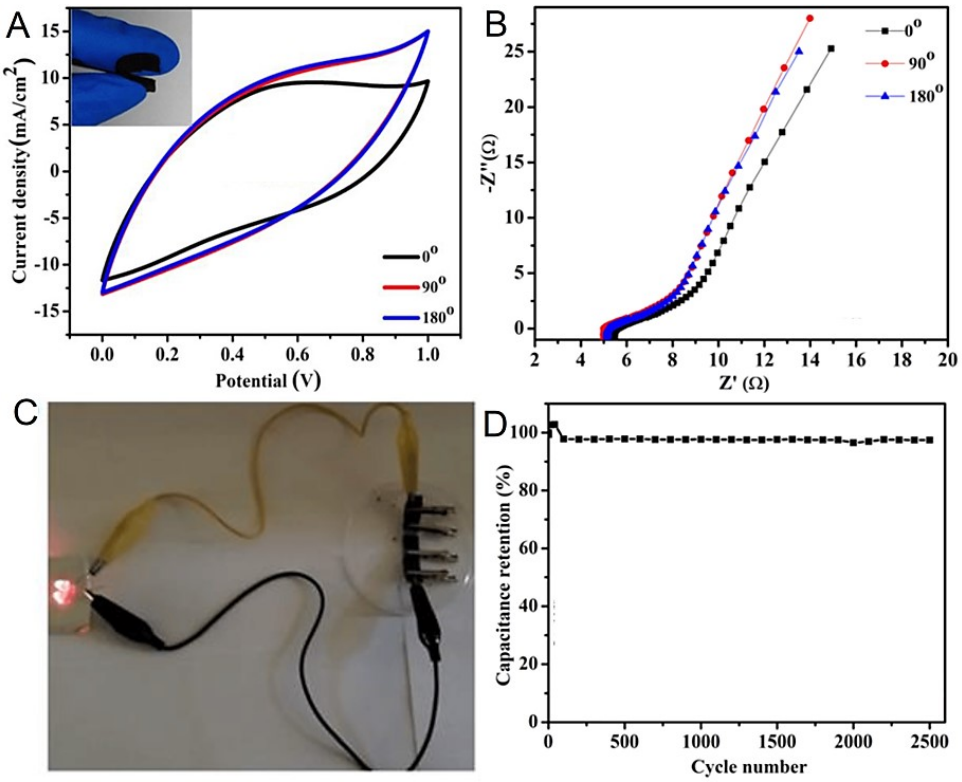

Figure 4. (A) Cyclic voltametric curves of the polypyrrole/kapok fiber/carbon nanotube nanocomposite bent at various angles (40 mV s^{-1}), inset is digital photograph of flexible supercapacitor in a bending state; **(B)** electrochemical impedance spectroscopy spectra of the polypyrrole/kapok fiber/carbon nanotube nanocomposite based flexible supercapacitor at various bending angles; **(C)** digital photograph of red light emitting diode powered by three polypyrrole/kapok fiber/carbon nanotube nanocomposites based supercapacitors connected in series; **(D)** cycling stability (2500 cycles, 25 mA cm^{-2}) of the assembled polypyrrole/kapok fiber/carbon nanotube nanocomposite based flexible all-solid-state symmetric supercapacitor [81].

Reproduced with permission from MDPI.

Recently, graphene has been a hot focus of research for technical applications, due to its inherent nanocarbon nanostructure [82]. Predominantly, nanocomposite forms of graphene have been reported efficient for energy conversion device applications [83]. Here, adding minute graphene contents have shown remarkable increase in the physical properties of the nanocomposites [84]. For supercapacitors, graphene or modified graphene has been combined with inorganic metal or metal oxide nanoparticles to form the supercapacitor electrodes [85]. For example, Ezeigwe et al. [86] fabricated a supercapacitor electrode based on the graphene and zinc oxide-based nanomaterial. They used green liquid phase exfoliation and solvothermal_techniques to synthesize the graphene/zinc oxide hybrid. In these methods water and ethanol solvents were used as environmentally safe reagents. The resulting graphene/zinc oxide hybrid had reasonable specific capacitance of about 236 Fg^{-1} for supercapacitor electrode application. Additionally, non-conjugated polymers, like poly (vinyl alcohol) and poly (ethylene glycol) have been used for supercapacitor electrodes [87]. In this regard, Nayak et al. [88] used poly (vinyl alcohol) as a green

polymer with graphene for supercapacitor electrodes. Consequently, they designed the poly (vinyl alcohol)/graphene/WO_3 hybrid as a green electrode nanomaterial for solid state asymmetric supercapacitor application. This device had energy density of 6–25 W h kg^{-1} over 4000 charge-discharge cyclic recital. The solid-state asymmetric supercapacitor was capable of lighting the red-light emitting diode, as shown in **Figure 5**.

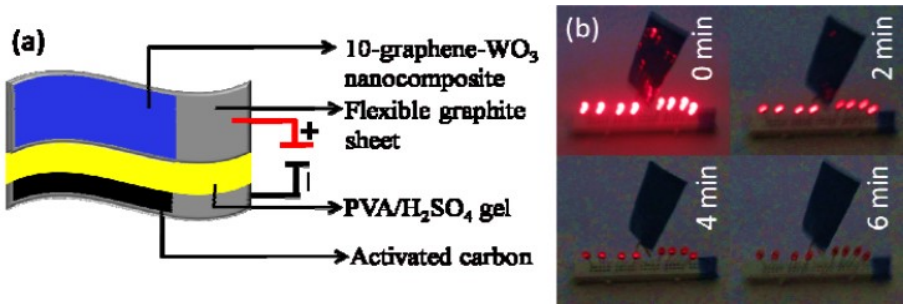

Figure 5. (a) Diagram of a flexible solid state asymmetric supercapacitor device set-up of poly (vinyl alcohol)/graphene/WO_3 hybrid; **(b)** picture of real asymmetric supercapacitor device of poly (vinyl alcohol)/graphene/WO_3 hybrid applied to light red light emitting diodes after charging [88].
Reproduced with permission from ACS.

Majority of the research attempts on polymer/nanocarbon nanomaterials for supercapacitor electrodes have reported the use of conjugated polymers [89]. According, conducting polymer/graphene nanocomposites have been prepared having superior electrochemical performance for supercapacitors [90]. For this purpose, the conducting polymer/graphene nanocomposites have been fabricated through facile green methods [91]. Consequently, conducting polymer/graphene nanocomposite-based electrodes were found to have low cost, durability, superior surface area, specific capacitance, energy/power density, and cyclic performance [92]. A number of conductive polymers have been used with graphene to form supercapacitor electrodes, namely polyindole, polyaniline, polypyrrole, polythiophene, and their derived forms [93]. Ramesh et al. [94] used a green hydrothermal route for the formation of the polyindole/cobalt (II, III)/nitrogen doped graphene oxide hybrids aiming for ecological supercapacitor electrodes. **Figure 6A** shows the process for the formation of cobalt (II, III)/nitrogen doped graphene oxide and polyindole/cobalt (II, III)/nitrogen doped graphene oxide hybrids involving oxidative polymerization and hydrothermal routes. **Figure 6B,C** shows the scanning electron microscopy images of polyindole/cobalt (II, III)/nitrogen doped graphene oxide. A homogeneously dispersed microstructure with cobalt oxides nanoparticles of about 10–20 nm were seemed to be distributed on the hexagonal nanosheets of nitrogen doped graphene oxide. **Figure 6D** depicts the specific capacitance vs. current density of the polyindole/cobalt (II, III)/nitrogen doped graphene oxide hybrid. Here, highest specific capacitance of around 680 F g^{-1} was attained at the current density of 0.5 Ag^{-1} in 5000 cyclic durations. Hence, the green synthesized polyindole/cobalt (II, III)/nitrogen doped graphene oxide hybrids had fine potential for supercapacitor electrode utilization.

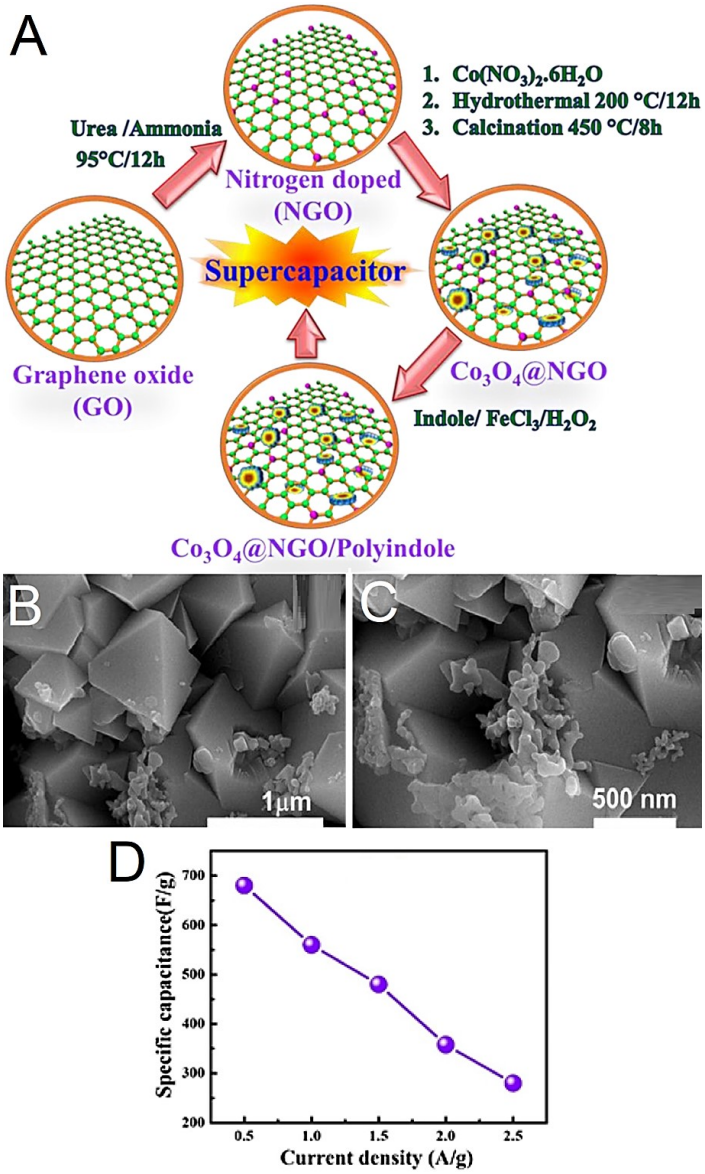

Figure 6. (A) Schematic for the formation of cobalt (II, III)/nitrogen doped graphene oxide (Co_3O_4@NGO) and polyindole/cobalt (II, III)/nitrogen doped graphene oxide (PIN/Co_3O_4@NGO) hybrid; **(B** and **C)** scanning electron microscopy images of PIN/Co_3O_4@NGO hybrid; **(D)** specific capacitance vs. current density of the PIN/Co_3O_4@NGO hybrid [94].

Reproduced with permission from Elsevier (Open access).

Gul et al. [95] devised green nanocomposites of the polyaniline/graphene oxide co-doped dodecyl benzene sulfonic acid hybrid and the polyaniline/graphene oxide co-doped camphor sulfonic acid hybrid via in situ and doping processes for the supercapacitor electrodes. **Figure 7A** shows the scanning electron microscopy micrographs of the polyaniline/graphene oxide co-doped dodecyl benzene sulfonic acid hybrid with fine nanoparticle dispersion and porous morphology. **Figure 7B** displays the scanning electron microscopy micrographs of the polyaniline/graphene oxide co-doped camphor sulfonic acid hybrid having similar nanoparticle distribution and porous morphology.

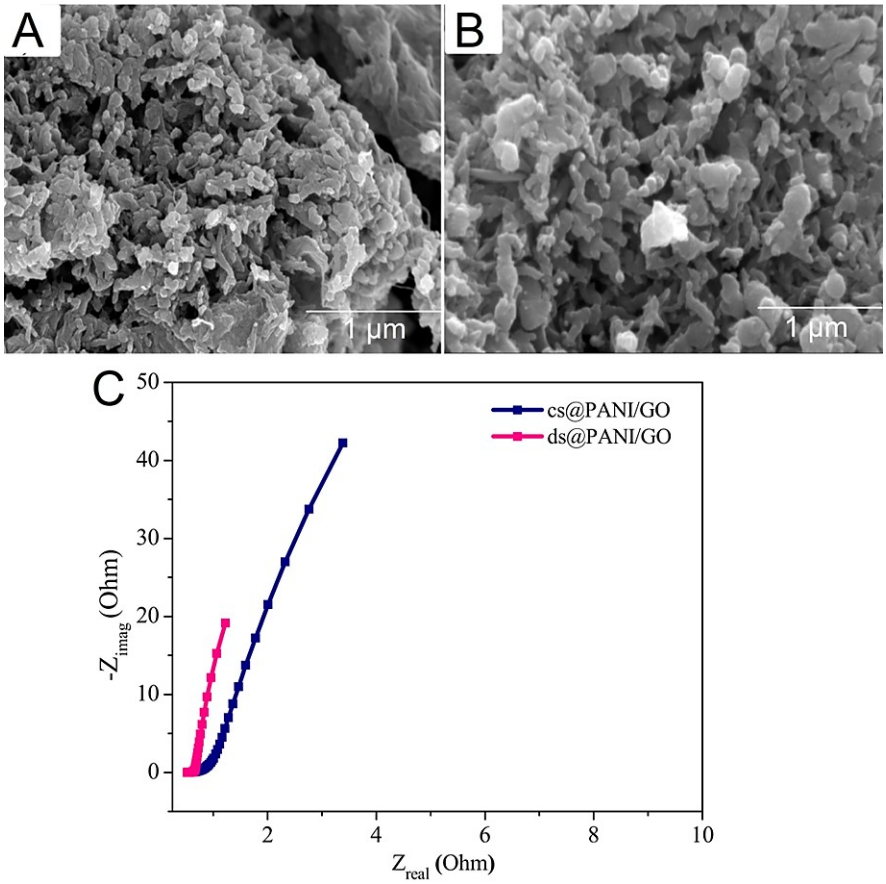

Figure 7. Scanning electron microscopy micrographs of **(A)** polyaniline/graphene oxide co-doped dodecyl benzene sulfonic acid (ds@PANI/GO) hybrid; **(B)** polyaniline/graphene oxide co-doped camphor sulfonic acid (cs@PANI) hybrid; **(C)** Nyquist plots of ds@PANI/GO and cs@PANI/GO hybrids [95].
Reproduced with permission from MDPI.

Figure 7C expresses the Nyquist plots of the hybrids with a compressed semicircle behavior in high frequency region by both the polyaniline/graphene oxide co-doped dodecyl benzene sulfonic acid and polyaniline/graphene oxide co-doped camphor sulfonic acid hybrids showing low resistance electrical conductivity properties, Consequently, the green supercapacitor device had high power density of > 1700 Wkg^{-1}, specific capacitance of 97–150 Fg^{-1}, and capacitance retention of 93–97 %. Li et al. [96] fabricated the cellulose/polyaniline blend and cellulose/polyaniline/graphene oxide hybrid via facile green in situ polymerization, as shows in **Figure 8a**.

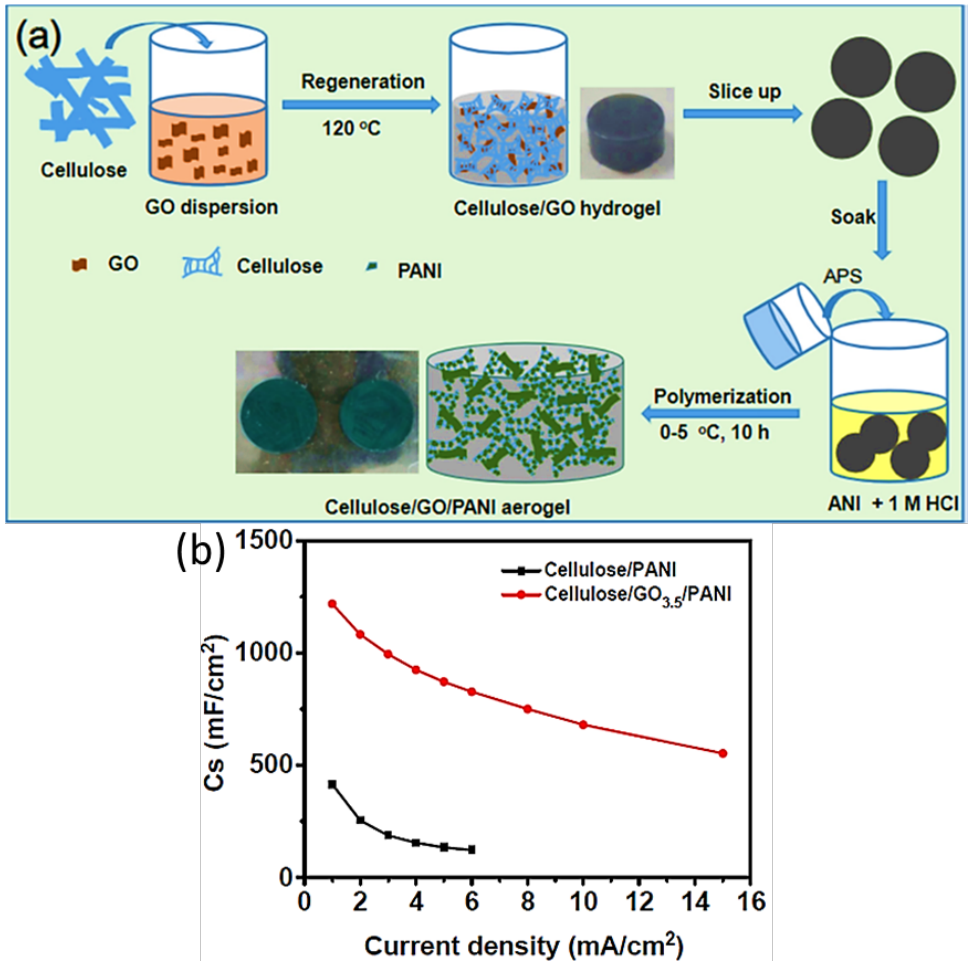

Figure 8. (a) Synthetic route for the cellulose/polyaniline/graphene oxide; **(b)** plots of areal specific capacitance vs. current for the cellulose/polyaniline and cellulose/polyaniline/graphene oxide [96].

GO = graphene oxide; PANI = polyaniline; ANI = aniline Reproduced with permission from MDPI.

Figure 8b presents the areal specific capacitance of the cellulose/polyaniline blend and cellulose/polyaniline/graphene oxide hybrid. As compared to the blend sample, the cellulose/polyaniline/graphene oxide hybrid with 5 wt.% nanofiller had superior areal specific capacitance, power density, and electrical conductivity of around 1218 $mFcm^{-2}$, 1201 μWcm^{-2}, and 1.15 Scm^{-1}, respectively. Thus, the green cellulose/polyaniline/graphene oxide hybrid revealed high performance for practical ecological supercapacitor applications.

Henceforth, several successful design combinations have been proposed for green energy storage devices, like supercapacitors, employing suitable green materials and methods [97–99]. In this concern, environmentally friendly supercapacitor electrodes based on conjugated polymers, such as polyaniline, polypyrrole, etc., and green polymers like cellulose, chitosan, etc., have been developed [100–102]. Moreover, carbon nanotube and graphene have been used as green nanocarbons for the ecological supercapacitor electrodes [103,104]. Moreover, facile green processing techniques, such as in situ method, sonication, solution mixing, hydrothermal method, etc., have been adopted to form the ecological polymer/nanocarbon nanomaterials for energy maneuvers [105]. Consequently, the ensuing supercapacitor electrodes had fine

electron conduction and charge transport features for high end green energy devices [106–108]. In this way, superior surface area, electrochemical features, electrical conductivity, specific capacitance, and power/charge density have been attained for the ecological supercapacitor devices [109].

5. Perspectives and encounters

Conventionally, industrial level energy systems have been designed using expensive materials and high-priced sophisticated techniques to attain desired high energy outputs. For example, commercially employed supercapacitor devices usually comprise of high cost electrodes and catalysts prepared via non-environmental techniques. Moreover, commercial supercapacitors lack sustainability and biodegradability properties, in turn causing green house effects. In this concern, recent research has been continuously turned toward the development of low cost, sustainable, biodegradable, non-toxic, and environmentally friendly materials for supercapacitor assemblies. Use of green techniques may further enhance the potential of green nanomaterials towards supercapacitors. Additionally, green materials derived supercapacitors must have the advantages of superior mechanical/thermal stability, electron conduction, specific capacitance, capacitance retention, energy/power density, charge-discharge, durability over repeated cyclic life, and other desirable electrochemical features. For this purpose, choice of green polymer, green nanofiller, as well as green processing route have found indispensable to fabricate high-tech energy device materials. **Table 1** presents essential comparison of important design, properties and application of various past and present green nanomaterials used for supercapacitors.

According to the literature presented in above sections, it is important to highlight the specific performance metrics (such as specific capacitance, capacitance retention, energy density, power density, charge-discharge, etc.) of green nanocomposites needed for high performance supercapacitor devices. Specifically, Pawar et al. [110] recently used a green chemical bath deposition method for the formation of polyaniline and reduced graphene oxide derived nanocomposite for supercapacitor electrodes. The subsequent polyaniline/reduced graphene oxide nanocomposites showed considerable high specific capacitance and capacitance retention of > 1130 Fg^{-1} and > 80 %, respectively, in 5000 charge-discharge cyclic route. In addition, polyaniline/reduced graphene oxide had superior power density and energy density around 732 W kg^{-1} and 23 Wh kg^{-1}, respectively. Thus, supercapacitor performance matrices were analyzed via specific capacitance, capacitance retention, charge-discharge, energy density, and power density features. Very recently, Mupit et al. [111] used green chemical exfoliation and in situ methods for the formation of environmental friendly polyaniline/graphene nanocomposites. These supercapacitor electrodes had high specific capacitance of > 300 F g^{-1}. Also, in a recent attempt by Tale et al. [112], nanocarbons and manganese dioxide based green nanomaterials were prepared for supercapacitor electrodes. The ensuing electrodes showed superior specific capacitance and capacitance retention of about 1900 Fg^{-1} and 98 %, relatively, over 6000 charge/discharge cycles.

Presently used environmentally friendly methods for green nanomaterials include in situ polymerization, solution mixing, and similar simple techniques [113,114]. These lab-scale synthesis practices for green nanomaterials have advantages of inexpensiveness, non-toxic fabrication, and easy processing. However, large scale or industrial level production of green nanomaterials using solution or in situ methods face countless challenges [115]. Most importantly, these methods may result in poor material compatibility, dispersion, and homogeneity issues, so hindering the scalability, high performance, and applicability of these nanomaterials on commercial level [116]. Here, it is suggested to use advanced sophisticated techniques like spinning, coating, three dimensional printing, etc., to overcome the potential barriers towards scalability or commercial adoption of green nanocomposites. Use of advanced processing techniques for green nanomaterial ensure well-controlled and optimized conditions for industrial scale production of energy systems [117].

In real world, field researchers are constantly striving to integrate green nanohybrids into supercapacitor electrodes (especially as anodes) to gain superior charge storage, cyclic rate, and performance endurance [118]. For practical industrial applications, recent designs of green derived supercapacitor components had sustainability, long life, and potential to store larger amount of electricity for rapid charging, compared with out-of-date traditional commercial supercapacitors [119]. Continuing research on conducting polymers based green or environmentally friendly nanomaterials showed important real life uses in micro-supercapacitors. Presently, these green micro-supercapacitors have been found commercially beneficial for applications in modern smartphones, portable computers or laptops, electric vehicles, and other sustainable energy/electronic devices [120,121]. It is important to mention that restricted attempts have been reported to deal with the current market trends of green nanomaterials based energy systems so far [122]. Nevertheless, the available literature up till now specified future potential estimates of green nanomaterials for forthcoming breakthroughs of their possible marketplace [123].

Table 1. Comparison of past and present green nanomaterials for supercapacitors.

Matrix	Nanoadditive	Green method	Property/Application	Ref.
Polyaniline/graphene oxide/gold nanoparticles and polyaniline/	Reduced graphene oxide/gold nanoparticles	Green in situ synthesis; Cetraria Islandica L. Ach lichen	Supercapacitor electrode has scan rate of 5–200 mV s^{-1}; specific capacitance and capacitance retention 212.8 F g^{-1} and 86.9%, correspondingly	[19]
Polyacrylonitrile/polyaniline/	Graphene	Drop casting; screen printing	Electron conductivity 2.362×10^{-6} S m^{-1}	[20]
Cellulose/polyaniline	Graphene oxide	In situ technique	Electron conductivity and areal specific capacitance of 1.15 S cm^{-1} and 1218 mF cm^{-2}, respectively; energy density of 1201 μW/cm^2	[96]
Polyaniline	Reduced graphene oxide	Chemical bath deposition	Supercapacitor electrodes; specific capacitance 1130 F g^{-1}; capacitance retention 82 %; 5000 cycles	[110]

Table 1. (*Continued*).

Matrix	Nanoadditive	Green method	Property/Application	Ref.
Polyaniline	Graphene oxide	Chemical exfoliation; in situ technique	Supercapacitor electrode; specific capacitance > 300 F g^{-1}	[111]
Polyaniline	Graphene; graphene oxide; manganese dioxide	In situ method	Supercapacitor electrode; specific capacitance > 1882 F g^{-1}; capacitance retention ~ 98 %; 6063 cycles	[112]
Polyaniline	Reduced graphene oxide; amine functional graphene	In situ process	Electrical conductivity 8.66 S cm^{-1}; specific capacitance 250 F g^{-1}	[124]
Polyaniline	Sulfonated graphene	In situ polymerization	Specific capacitance 478 F g^{-1}	[125]
Polyaniline	Aniline-functional-graphene	In situ method	Supercapacitor electrodes; specific capacitance 100–440 F g^{-1}; capacitance retention 73–80%	[126]
Bacterial cellulose	Carbonization	Solution process	Supercapacitor electrodes; specific capacitance and capacitance retention 216 F g^{-1} and 97.6 %, respectively	[127]
Bacterial cellulose	Carbon nanotube	Solution process	Supercapacitor electrodes; specific capacitance and capacitance retention 50.5 F g^{-1} and 99.5%, respectively	[128]
Bacterial cellulose	Polypyrrole	In situ Method	Supercapacitor electrodes; specific capacitance and capacitance retention153 F g^{-1} and 93.0 %, respectively	[129]
Bacterial cellulose	Polypyrrole; Carbon nanotube	In situ Method	Supercapacitor electrodes; specific capacitance and capacitance retention 228 F g^{-1} and 88.0%, respectively	[130]
Bacterial cellulose	Polypyrrole; Graphene	In situ Method	Supercapacitor electrodes; specific capacitance and capacitance retention 4.16 F cm^{-2} and 91.5%, respectively	[131]
Bacterial cellulose	Polypyrrole; reduced graphene oxide	In situ Method	Supercapacitor electrodes; specific capacitance and capacitance retention 3.66 F cm^{-2} and 73.5%, respectively	[132]
Bacterial cellulose	Reduced graphene oxide	Solution process	Supercapacitor electrodes; specific capacitance and capacitance retention 2106–2544 mF cm^{-2} and 100%, respectively	[133]
Poly (vinylpyrrolidone)/recycled poly (ethyelene terephthalate)	Graphene	Screen printing technique	Specific capacitance and capacitance retention of 201 F g^{-1} and 97%, respectively	[134]
Polyaniline	Olive stones functional reduced graphene oxide	In situ self assembly	Specific capacitance 582.6 F g^{-1}; capacity retention 97 %; 3000 cycles	[135]

For future high performance and applicability of green nanomaterials in advance energy storage systems, it is suggested to define precise research directions by intensive repeated research efforts on the synthesis and analysis of these materials. In this regard, wide-ranging experimental as well as theoretical studies need to be performed on nontoxic, ecofriendly, sustainable, and biocompatible nanocomposites

with predefined property improvement phenomenon for progresses in this field. According to literature analysis, it can also be suggested that future of green nanocomposites relies on scalability and large scale production of these materials for real world applications by considering the necessary environmental and economic concerns. Moreover, future research on green nanomaterials have been found essential to reveal further utilizations towards the green/sustainable microelectronics, solar cells, light emitting diodes, and related high end devices.

6. Conclusions

In brief, this review manuscript argues ecologically essential polymers, nanofillers, and nanocomposites viable for applications in significant energy devices, particularly the supercapacitor components. For this application, conducting and synthetic green polymers have been filled with carbon nanoparticles like carbon nanotube and graphene. In this regard, ecological and low cost method have been applied to attain high performance environmental friendly energy materials for supercapacitor related systems. Typically, in situ polymerization, electrochemical polymerization, solution processing, and similar facile synthesis techniques have been used for the synthesis of green nanomaterials for energy devices. Mixing of polymers with nanomaterials through green methods considerably improved the processability, structural stability, ecofriendliness, and life-long performance of the resulting components for energy devices. In this regard, electrical conductivity, mechanical stability, heat conduction, capacitance, and cyclic performances of green nanomaterials have been investigated. Potential of green nanomaterials for energy devices points towards essential future industrial level utilizations, nevertheless continuous research efforts must be performed to introduce new design varieties and to overcome the fabrication and performance hindering challenges. After considering the literature surveys presented in the above sections of this novel review, it can be suggested that future research on new design combinations, property/performance investigation, and minimization of challenges for green nanocomposites can lead to promising commercial level energy devices. In this way, advanced potentials of high performance green nanomaterials based energy storing systems can be explored for utilizations in modern electronics, space/defence structures, and biomedical equipment.

Conflict of interest: The author declares no conflict of interest.

References

1. Kumar M, Sharma P, Chakravarty A, et al. How Eco-friendly Nanomaterials are Effective for the Sustainability of the Environment. Green Synthesis of Nanomaterials. 2024; 169–186. doi: 10.1002/9781119900931.ch8
2. Kausar A. Progressive Green Nanocomposites for Microbial Fuel Cells—State-of-the-Art and Technical Advancements. Polymer-Plastics Technology and Materials. 2024; 63(15): 2151–2169. doi: 10.1080/25740881.2024.2367000
3. Fertier L, Koleilat H, Stemmelen M, et al. The use of renewable feedstock in UV-curable materials – A new age for polymers and green chemistry. Progress in Polymer Science. 2013; 38(6): 932–962. doi: 10.1016/j.progpolymsci.2012.12.002
4. Tan N, Lee C, Li P. Green Synthesis of Smart Metal/Polymer Nanocomposite Particles and Their Tuneable Catalytic Activities. Polymers. 2016; 8(4): 105. doi: 10.3390/polym8040105
5. Kapoor A, Raghunathan M, Lal B, et al. Sustainable valorization of waste plastic into nanostructured materials for

environmental, energy, catalytic and biomedical applications: A review. Chemosphere. 2024; 364: 143279. doi: 10.1016/j.chemosphere.2024.143279
6. Kausar A. Progress in green nanocomposites for high-performance applications. Materials Research Innovations. 2020; 25(1): 53–65. doi: 10.1080/14328917.2020.1728489
7. Bakhoum E, Garas G, Allam M. Sustainability analysis of conventional and eco-friendly materials: A step towards green building. ARPN Journal of Engineering and Applied Sciences. 2015; 10 (2): 788–796
8. Liu Y, Biswas B, Hassan M, et al. Green Adsorbents for Environmental Remediation: Synthesis Methods, Ecotoxicity, and Reusability Prospects. Processes. 2024; 12(6): 1195. doi: 10.3390/pr12061195
9. Bhattacharjee J, Roy S. Smart materials for sustainable energy. Natural Resources Conservation and Research. 2024; 7(1): 5536. doi: 10.24294/nrcr.v7i1.5536
10. Wang R, Feng Y, Li D, et al. Towards the sustainable production of biomass-derived materials with smart functionality: a tutorial review. Green Chemistry. 2024; 26(16): 9075–9103. doi: 10.1039/d4gc01771d
11. Ahmadi Y, Ahmad S. Surface-active antimicrobial and anticorrosive Oleo-Polyurethane/graphene oxide nanocomposite coatings: Synergistic effects of in-situ polymerization and π-π interaction. Progress in Organic Coatings. 2019; 127: 168–180. doi: 10.1016/j.porgcoat.2018.11.019
12. Dell RM, Rand DAJ. Energy storage-a key technology for global energy sustainability. Journal of power sources. 2001; 100(1–2): 2–17. doi: 10.1016/S0378-7753(01)00894-1
13. Mohan T, Kanny K. Green Nanofillers for Polymeric Materials. Springer, Singapore; 2020. pp. 99–138.
14. Siwal SS, Zhang Q, Devi N, et al. Carbon-Based Polymer Nanocomposite for High-Performance Energy Storage Applications. Polymers. 2020; 12(3): 505. doi: 10.3390/polym12030505
15. Kausar A, Ahmad I, Zhao T, et al. Polymer/Graphene Nanocomposites via 3D and 4D Printing—Design and Technical Potential. Processes. 2023; 11(3): 868. doi: 10.3390/pr11030868
16. Matinise N, Botha N, Madiba IG, et al. Mixed-phase bismuth ferrite oxide (BiFeO3) nanocomposites by green approach as an efficient electrode material for supercapacitor application. MRS Advances. 2023; 8(12): 703–707. doi: 10.1557/s43580-023-00603-4
17. Başlak C, Öztürk G, Demirel S, et al. Green synthesis of carbon quantum dots from Sideritis vuralii and its application in supercapacitors. Inorganic Chemistry Communications. 2023; 153: 110845. doi: 10.1016/j.inoche.2023.110845
18. Xiong C, Zheng C, Jiang X, et al. Recent progress of green biomass based composite materials applied in supercapacitors, sensors, and electrocatalysis. Journal of Energy Storage. 2023; 72: 108633. doi: 10.1016/j.est.2023.108633
19. Çıplak Z, Yıldız A, Yıldız N. Green preparation of ternary reduced graphene oxide-au@polyaniline nanocomposite for supercapacitor application. Journal of Energy Storage. 2020; 32: 101846. doi: 10.1016/j.est.2020.101846
20. Arthisree D, Madhuri W. Optically active polymer nanocomposite composed of polyaniline, polyacrylonitrile and green-synthesized graphene quantum dot for supercapacitor application. International Journal of Hydrogen Energy. 2020; 45(16): 9317–9327. doi: 10.1016/j.ijhydene.2020.01.179
21. Zhao Y, He J, Hu L, et al. Carboxyl-Substituted Organic Molecule Assembled with MXene Nanosheets for Boosting Aqueous Na+ Storage. Small. 2023; 19(47). doi: 10.1002/smll.202304182
22. Chakraborty S, M AR, Mary NL. Biocompatible supercapacitor electrodes using green synthesised ZnO/Polymer nanocomposites for efficient energy storage applications. Journal of Energy Storage. 2020; 28: 101275. doi: 10.1016/j.est.2020.101275
23. Roy A, Rajkuma, K, Kapgate B. Prospects of Green Materials in Rubber Technology. Springer; 2024. pp. 1–9.
24. Olatunji O. Re-Envisioning Plastics Role in the Global Society. Springer Nature Switzerland; 2024. doi: 10.1007/978-3-031-48945-7
25. Tabone MD, Cregg JJ, Beckman EJ, et al. Sustainability Metrics: Life Cycle Assessment and Green Design in Polymers. Environmental Science & Technology. 2010; 44(21): 8264–8269. doi: 10.1021/es101640n
26. Zhao Y, Zhou Y, Wu X, et al. A facile method for electrospinning of Ag nanoparticles/poly (vinyl alcohol)/carboxymethyl-chitosan nanofibers. Applied Surface Science. 2012; 258(22): 8867–8873. doi: 10.1016/j.apsusc.2012.05.106
27. Fauzi B, Mohd Nawawi MG, Fauzi R, et al. Physicochemical characteristics of sago starch-chitosan nanofillers film. BioResources. 2019; 14(4): 8324–8330. doi: 10.15376/biores.14.4.8324-8330
28. Mallakpour S, Dinari M. Synthesis and Properties of Biodegradable Poly (vinyl alcohol)/Organo-nanoclay

Bionanocomposites. Journal of Polymers and the Environment. 2012; 20(3): 732–740. doi: 10.1007/s10924-012-0432-7
29. Bagheri AR, Arabi M, Ghaedi M, et al. Dummy molecularly imprinted polymers based on a green synthesis strategy for magnetic solid-phase extraction of acrylamide in food samples. Talanta. 2019; 195: 390–400. doi: 10.1016/j.talanta.2018.11.065
30. Martí M, Molina L, Alemán C, et al. Novel Epoxy Coating Based on DMSO as a Green Solvent, Reducing Drastically the Volatile Organic Compound Content and Using Conducting Polymers As a Nontoxic Anticorrosive Pigment. ACS Sustainable Chemistry & Engineering. 2013; 1(12): 1609–1618. doi: 10.1021/sc400271k
31. Yuan C, Chen M, Luo J, et al. A novel water-based process produces eco-friendly bio-adhesive made from green cross-linked soybean soluble polysaccharide and soy protein. Carbohydrate Polymers. 2017; 169: 417–425. doi: 10.1016/j.carbpol.2017.04.058
32. Kalantari K, Afifi AM, Jahangirian H, et al. Biomedical applications of chitosan electrospun nanofibers as a green polymer – Review. Carbohydrate Polymers. 2019; 207: 588–600. doi: 10.1016/j.carbpol.2018.12.011
33. Patanair B, Saiter-Fourcin A, Thomas S, et al. Promoting Interfacial Interactions with the Addition of Lignin in Poly (Lactic Acid) Hybrid Nanocomposites. Polymers. 2021; 13(2): 272. doi: 10.3390/polym13020272
34. Jayrajsinh S, Shankar G, Agrawal YK, et al. Montmorillonite nanoclay as a multifaceted drug-delivery carrier: A review. Journal of Drug Delivery Science and Technology. 2017; 39: 200–209. doi: 10.1016/j.jddst.2017.03.023
35. Wu YY, Zhang J, Liu C, et al. Effect of Graphene Oxide Nanosheets on Physical Properties of Ultra-High-Performance Concrete with High Volume Supplementary Cementitious Materials. Materials. 2020; 13(8): 1929. doi: 10.3390/ma13081929
36. Lu DR, Xiao CM, Xu SJ. Starch-based completely biodegradable polymer materials. Express Polymer Letters. 2009; 3(6): 366–375. doi: 10.3144/expresspolymlett.2009.46
37. Kaushik A, Singh M, Verma G. Green nanocomposites based on thermoplastic starch and steam exploded cellulose nanofibrils from wheat straw. Carbohydrate Polymers. 2010; 82(2): 337–345. doi: 10.1016/j.carbpol.2010.04.063
38. Cheviron P, Gouanvé F, Espuche E. Green synthesis of colloid silver nanoparticles and resulting biodegradable starch/silver nanocomposites. Carbohydrate Polymers. 2014; 108: 291–298. doi: 10.1016/j.carbpol.2014.02.059
39. Ragauskas AJ, Beckham GT, Biddy MJ, et al. Lignin Valorization: Improving Lignin Processing in the Biorefinery. Science. 2014; 344(6185). doi: 10.1126/science.1246843
40. Norberg I, Nordström Y, Drougge R, et al. A new method for stabilizing softwood kraft lignin fibers for carbon fiber production. Journal of Applied Polymer Science. 2012; 128(6): 3824–3830. doi: 10.1002/app.38588
41. Fila K, Podkościelna B, Szymczyk K. The application of chitosan as an eco-filler of polymeric composites. Adsorption. 2023; 30(2): 157–165. doi: 10.1007/s10450-023-00403-0
42. Hashem AH, Shehabeldine AM, Ali OM, et al. Synthesis of Chitosan-Based Gold Nanoparticles: Antimicrobial and Wound-Healing Activities. Polymers. 2022; 14(11): 2293. doi: 10.3390/polym14112293
43. Di Carlo G, Curulli A, Toro RG, et al. Green Synthesis of Gold–Chitosan Nanocomposites for Caffeic Acid Sensing. Langmuir. 2012; 28(12): 5471–5479. doi: 10.1021/la204924d
44. Rodriguez-Rivera GJ, Green M, Shah V, et al. A user's guide to degradation testing of polyethylene glycol-based hydrogels: From in vitro to in vivo studies. Journal of Biomedical Materials Research Part A. 2023; 112(8): 1200–1212. doi: 10.1002/jbm.a.37609
45. Jayan JS, Deeraj BDS, Saritha A, et al. Theoretical modelling of kinetics of glass transition temperature of PEG toughened epoxy. Plastics, Rubber and Composites. 2020; 49(6): 237–244. doi: 10.1080/14658011.2020.1732124
46. Nguyen L, Lamichhane P, Choi E, et al. Structural and Optical Sensing Properties of Nonthermal Atmospheric Plasma-Synthesized Polyethylene Glycol-Functionalized Gold Nanoparticles. Nanomaterials. 2021; 11(7): 1678. doi: 10.3390/nano11071678
47. Gopi S, Amalraj A, Kalarikkal N, et al. Preparation and characterization of nanocomposite films based on gum arabic, maltodextrin and polyethylene glycol reinforced with turmeric nanofiber isolated from turmeric spent. Materials Science and Engineering: C. 2019; 97: 723–729. doi: 10.1016/j.msec.2018.12.089
48. Cavallaro G, Lazzara G, Milioto S. Sustainable nanocomposites based on halloysite nanotubes and pectin/polyethylene glycol blend. Polymer Degradation and Stability. 2013; 98(12): 2529–2536. doi: 10.1016/j.polymdegradstab.2013.09.012
49. Sganzerla WG, Longo M, de Oliveira JL, et al. Nanocomposite poly (ethylene oxide) films functionalized with silver nanoparticles synthesized with Acca sellowiana extracts. Colloids and Surfaces A: Physicochemical and Engineering Aspects. 2020; 602: 125125. doi: 10.1016/j.colsurfa.2020.125125

50. Hong B, Panagiotopoulos AZ. Molecular Dynamics Simulations of Silica Nanoparticles Grafted with Poly (ethylene oxide) Oligomer Chains. The Journal of Physical Chemistry B. 2012; 116(8): 2385–2395. doi: 10.1021/jp2112582
51. Kirar S, Mohne D, Singh M, et al. Eco-friendly lignin nanocomposite films as advanced UV protective and antimicrobial sustainable packaging materials. Sustainable Materials and Technologies. 2024; 40: e00864. doi: 10.1016/j.susmat.2024.e00864
52. Ibrahim MM, Koschella A, Kadry G, et al. Evaluation of cellulose and carboxymethyl cellulose/poly (vinyl alcohol) membranes. Carbohydrate Polymers. 2013; 95(1): 414–420. doi: 10.1016/j.carbpol.2013.03.012
53. Joorabloo A, Khorasani MT, Adeli H, et al. Fabrication of heparinized nano ZnO/poly (vinylalcohol)/carboxymethyl cellulose bionanocomposite hydrogels using artificial neural network for wound dressing application. Journal of Industrial and Engineering Chemistry. 2019; 70: 253–263. doi: 10.1016/j.jiec.2018.10.022
54. Morsi MA, Oraby AH, Elshahawy AG, et al. Preparation, structural analysis, morphological investigation and electrical properties of gold nanoparticles filled polyvinyl alcohol/carboxymethyl cellulose blend. Journal of Materials Research and Technology. 2019; 8(6): 5996–6010. doi: 10.1016/j.jmrt.2019.09.074
55. Krikorian V, Pochan DJ. Poly (l-Lactic Acid)/Layered Silicate Nanocomposite: Fabrication, Characterization, and Properties. Chemistry of Materials. 2003; 15(22): 4317–4324. doi: 10.1021/cm034369
56. Wang K, Lu J, Tusiime R, et al. Properties of poly (l-lactic acid) reinforced by l-lactic acid grafted nanocellulose crystal. International Journal of Biological Macromolecules. 2020; 156: 314–320. doi: 10.1016/j.ijbiomac.2020.04.025
57. Li L, Bao RY, Gao T, et al. Dopamine-induced functionalization of cellulose nanocrystals with polyethylene glycol towards poly (L-lactic acid) bionanocomposites for green packaging. Carbohydrate Polymers. 2019; 203: 275–284. doi: 10.1016/j.carbpol.2018.09.057
58. Mishnaevsky L, Branner K, Petersen H, et al. Materials for Wind Turbine Blades: An Overview. Materials. 2017; 10(11): 1285. doi: 10.3390/ma10111285
59. Sukumaran NP, Gopi S. Overview of biopolymers. ScienceDirect; 2021. pp. 1–19.
60. Guo J, Xu Y, Jin S, et al. Conjugated organic framework with three-dimensionally ordered stable structure and delocalized π clouds. Nature Communications. 2013; 4(1). doi: 10.1038/ncomms3736
61. Perumal P, Christopher Selvin P, Selvasekarapandian S, et al. Plasticizer incorporated, novel eco-friendly bio-polymer based solid bio-membrane for electrochemical clean energy applications. Polymer Degradation and Stability. 2019; 159: 43–53. doi: 10.1016/j.polymdegradstab.2018.11.013
62. Ghosh SK, Sinha TK, Mahanty B, et al. Porous polymer composite membrane based nanogenerator: A realization of self-powered wireless green energy source for smart electronics applications. Journal of Applied Physics. 2016; 120(17). doi: 10.1063/1.4966652
63. Zhang Q, Sun Y, Xu W, et al. Organic Thermoelectric Materials: Emerging Green Energy Materials Converting Heat to Electricity Directly and Efficiently. Advanced Materials. 2014; 26(40): 6829–6851. doi: 10.1002/adma.201305371
64. Feng W, Long P, Feng Y, et al. Two-Dimensional Fluorinated Graphene: Synthesis, Structures, Properties and Applications. Advanced Science. 2016; 3(7). doi: 10.1002/advs.201500413
65. Zhao W, Jiao Y, Li J, et al. One-pot synthesis of conjugated microporous polymers loaded with superfine nano-palladium and their micropore-confinement effect on heterogeneously catalytic reduction. Journal of Catalysis. 2019; 378: 42–50. doi: 10.1016/j.jcat.2019.07.056
66. Gaikwad P, Tiwari N, Kamat R, et al. A comprehensive review on the progress of transition metal oxides materials as a supercapacitor electrode. Materials Science and Engineering: B. 2024; 307: 117544. doi: 10.1016/j.mseb.2024.117544
67. Shah SS, Niaz F, Ehsan MA, et al. Advanced strategies in electrode engineering and nanomaterial modifications for supercapacitor performance enhancement: A comprehensive review. Journal of Energy Storage. 2024; 79: 110152. doi: 10.1016/j.est.2023.110152
68. Wang Y, Xu T, Liu K, et al. Inside Back Cover: Biomass-based materials for advanced supercapacitor: principles, progress, and perspectives. Aggregate. 2024; 5(1). doi: 10.1002/agt2.510
69. Muzaffar A, Ahamed MB, Hussain CM. Green supercapacitors: Latest developments and perspectives in the pursuit of sustainability. Renewable and Sustainable Energy Reviews. 2024; 195: 114324. doi: 10.1016/j.rser.2024.114324
70. Liu S, Yu T, Wu Y, et al. Evolution of cellulose into flexible conductive green electronics: a smart strategy to fabricate sustainable electrodes for supercapacitors. RSC Adv. 2014; 4(64): 34134–34143. doi: 10.1039/c4ra07017h
71. Satchanska G, Davidova S, Petrov PD. Natural and Synthetic Polymers for Biomedical and Environmental Applications.

Polymers. 2024; 16(8): 1159. doi: 10.3390/polym16081159
72. Ma H, Zhao Q, Cheng P, et al. Wood-derived flexible supercapacitors for anti-freezing green power sources. Journal of Materials Chemistry A. 2024; 12(31): 20088–20096. doi: 10.1039/d4ta02190h
73. Suman, Rani G, Ahlawat R, and Kumar H. Green source-based carbon quantum dots, composites, and key factors for high-performance of supercapacitors. Journal of Power Sources. 2024; 617: 235170
74. Alsaad AM, Aljarrah IA, Ahmad AhmadA, et al. The structural, optical, thermal, and electrical properties of synthesized PEO/GO thin films. Applied Physics A. 2022; 128(8). doi: 10.1007/s00339-022-05829-x
75. Albarqouni YMY, Lee SP, Ali GAM, et al. Facile synthesis of reduced graphene oxide aerogel in soft drink as supercapacitor electrode. Journal of Nanostructure in Chemistry. 2021; 12(3): 417–427. doi: 10.1007/s40097-021-00424-7
76. Jafari M, Botte GG. Sustainable Green Route for Activated Carbon Synthesis from Biomass Waste for High-Performance Supercapacitors. ACS Omega. Published online March 8, 2024. doi: 10.1021/acsomega.3c09438
77. Sun K, Li J, Wu D, et al. Green Synthesis of Porous Honeycomblike Carbon Materials for Supercapacitor Electrodes. Industrial & Engineering Chemistry Research. 2020; 59(32): 14288–14295. doi: 10.1021/acs.iecr.0c00828
78. Kim YR, Nam HK, Lee Y, et al. Green supercapacitor patterned by synthesizing MnO/laser-induced-graphene hetero-nanostructures on wood via femtosecond laser pulses. Biochar. 2024; 6(1). doi: 10.1007/s42773-024-00320-7
79. Borenstein A, Hanna O, Attias R, et al. Carbon-based composite materials for supercapacitor electrodes: a review. Journal of Materials Chemistry A. 2017; 5(25): 12653–12672. doi: 10.1039/c7ta00863e
80. Costa HPS, Duarte EDV, da Silva FV, et al. Green synthesis of carbon nanotubes functionalized with iron nanoparticles and coffee husk biomass for efficient removal of losartan and diclofenac: Adsorption kinetics and ANN modeling studies. Environmental Research. 2024; 251: 118733. doi: 10.1016/j.envres.2024.118733
81. Jyothibasu JP, Lee RH. Facile, Scalable, Eco-Friendly Fabrication of High-Performance Flexible All-Solid-State Supercapacitors. Polymers. 2018; 10(11): 1247. doi: 10.3390/polym10111247
82. Kausar A. N-Doped Graphene and Polymer Sequent Nanocomposite—Nitty-Gritties and Scoping Insights. Polymer-Plastics Technology and Materials. 2023; 62(11): 1347–1363. doi: 10.1080/25740881.2023.2207112
83. Kausar A, Ahmad I, Zhao T, et al. Graphene in Polymeric Nanocomposite Membranes—Current State and Progress. Processes. 2023; 11(3): 927. doi: 10.3390/pr11030927
84. Xu F, Gao M, Wang H, et al. Polymer-based graphene composite molding: a review. RSC Advances. 2023; 13(4): 2538–2551. doi: 10.1039/d2ra07744b
85. Sharifi J, Rizvi G, Fayazfar H. Sustainable 3D printing of enhanced carbon nanotube-based polymeric nanocomposites: green solvent-based casting for eco-friendly electrochemical sensing applications. The International Journal of Advanced Manufacturing Technology. 2024; 131(9–10): 4825–4837. doi: 10.1007/s00170-024-13337-w
86. Ezeigwe ER, Tan MTT, Khiew PS, et al. One-step green synthesis of graphene/ZnO nanocomposites for electrochemical capacitors. Ceramics International. 2015; 41(1): 715–724. doi: 10.1016/j.ceramint.2014.08.128
87. Refaat D, Mosa E, Fikry M, Omar M. A novel polyvinyl alcohol/polyethylene glycol (PVA/PEG) polymeric blend doped with graphene oxide for energy storage devices. ERU Research Journal. 2024; 3(1): 770–771. doi: 10.21608/erurj.2024.214106.1036
88. Nayak AK, Das AK, Pradhan D. High Performance Solid-State Asymmetric Supercapacitor using Green Synthesized Graphene–WO3 Nanowires Nanocomposite. ACS Sustainable Chemistry & Engineering. 2017; 5(11): 10128–10138. doi: 10.1021/acssuschemeng.7b02135
89. Zhu X, Yu S, Xu K, et al. Sustainable activated carbons from dead ginkgo leaves for supercapacitor electrode active materials. Chemical Engineering Science. 2018; 181: 36–45. doi: 10.1016/j.ces.2018.02.004
90. Cai X, Sun K, Qiu Y, et al. Recent Advances in Graphene and Conductive Polymer Composites for Supercapacitor Electrodes: A Review. Crystals. 2021; 11(8): 947. doi: 10.3390/cryst11080947
91. Okhay O, Tkach A. Synergetic Effect of Polyaniline and Graphene in Their Composite Supercapacitor Electrodes: Impact of Components and Parameters of Chemical Oxidative Polymerization. Nanomaterials. 2022; 12(15): 2531. doi: 10.3390/nano12152531
92. Chaluvachar P, Mahesha GT, Sudhakar YN, et al. A Review on Graphitic Carbon Nitride and Conducting Polymer Nanocomposite Electrodes for Supercapacitors. RAiSE-2023. Published online January 12, 2024: 154. doi: 10.3390/engproc2023059154
93. Selvaganesh SV, Mathiyarasu J, Phani K, et al. Chemical Synthesis of PEDOT–Au Nanocomposite. Nanoscale Research

Letters. 2007; 2(11). doi: 10.1007/s11671-007-9100-6
94. Ramesh S, Yadav H, Bathula C, et al. Cubic nanostructure of Co3O4@nitrogen doped graphene oxide/polyindole composite efficient electrodes for high performance energy storage applications. Journal of Materials Research and Technology. 2020; 9(5): 11464–11475. doi: 10.1016/j.jmrt.2020.08.037
95. Gul H, Shah A ul HA, Bilal S. Fabrication of Eco-Friendly Solid-State Symmetric Ultracapacitor Device Based on Co-Doped PANI/GO Composite. Polymers. 2019; 11(8): 1315. doi: 10.3390/polym11081315
96. Li Y, Xia Z, Gong Q, et al. Green Synthesis of Free Standing Cellulose/Graphene Oxide/Polyaniline Aerogel Electrode for High-Performance Flexible All-Solid-State Supercapacitors. Nanomaterials. 2020; 10(8): 1546. doi: 10.3390/nano10081546
97. Tian J, Peng D, Wu X, et al. Electrodeposition of Ag nanoparticles on conductive polyaniline/cellulose aerogels with increased synergistic effect for energy storage. Carbohydrate Polymers. 2017; 156: 19–25. doi: 10.1016/j.carbpol.2016.09.005
98. Wan C, Jiao Y, Liang D, et al. A Geologic Architecture System-Inspired Micro-/Nano-Heterostructure Design for High-Performance Energy Storage. Advanced Energy Materials. 2018; 8(33). doi: 10.1002/aenm.201802388
99. Mohammadi S, Mousavi-Khoshdel SM. Preparation of a Cu-Doped Graphene Oxide–Glutamine Nanocomposite for Supercapacitor Electrode Applications: An Experimental and Theoretical Study. ACS Applied Electronic Materials. 2024; 6(6): 4108–4119. doi: 10.1021/acsaelm.4c00224
100. Ren F, Li Z, Tan WZ, et al. Facile preparation of 3D regenerated cellulose/graphene oxide composite aerogel with high-efficiency adsorption towards methylene blue. Journal of Colloid and Interface Science. 2018; 532: 58–67. doi: 10.1016/j.jcis.2018.07.101
101. Zhong C, Deng Y, Hu W, et al. A review of electrolyte materials and compositions for electrochemical supercapacitors. Chemical Society Reviews. 2015; 44(21): 7484–7539. doi: 10.1039/c5cs00303b
102. Mousavi SM, Hashemi SA, Kalashgrani MY, et al. Bioresource Polymer Composite for Energy Generation and Storage: Developments and Trends. The Chemical Record. 2023; 24(1). doi: 10.1002/tcr.202200266
103. Sahoo PK, Kumar N, Jena A, et al. Recent progress in graphene and its derived hybrid materials for high-performance supercapacitor electrode applications. RSC Advances. 2024; 14(2): 1284–1303. doi: 10.1039/d3ra06904d
104. Siwach P, Gaba L, Aggarwal K, et al. Novel three-dimensional architectured ZnMgAl ternary layered double hydroxide@reduced graphene oxide nanocomposites as electrode material for high-performance supercapacitor. Journal of Energy Storage. 2024; 98: 113055. doi: 10.1016/j.est.2024.113055
105. Ul Hoque MdI, Donne SW, Holze R. Graphene Nanocomposite Materials for Supercapacitor Electrodes. Encyclopedia. 2024; 4(1): 101–116. doi: 10.3390/encyclopedia4010009
106. Ouyang W, Sun J, Memon J, et al. Scalable preparation of three-dimensional porous structures of reduced graphene oxide/cellulose composites and their application in supercapacitors. Carbon. 2013; 62: 501–509. doi: 10.1016/j.carbon.2013.06.049
107. Yang X, Fei B, Ma J, et al. Porous nanoplatelets wrapped carbon aerogels by pyrolysis of regenerated bamboo cellulose aerogels as supercapacitor electrodes. Carbohydrate Polymers. 2018; 180: 385–392. doi: 10.1016/j.carbpol.2017.10.013
108. Xavier JR. Graphene Oxide/Metal Sulfide and Oxide Nanocomposite Electrodes for High Electrochemical Performance Supercapacitor Applications. Journal of Materials Engineering and Performance. 2023; 33(4): 1772–1785. doi: 10.1007/s11665-023-08120-z
109. Mensah-Darkwa K, Zequine C, Kahol PK, et al. Supercapacitor Energy Storage Device Using Biowastes: A Sustainable Approach to Green Energy. Sustainability. 2019; 11(2): 414. doi: 10.3390/su11020414
110. Pawar DC, Bagde AG, Thorat JP, et al. Synthesis of reduced graphene oxide (rGO)/polyaniline (PANI) composite electrode for energy storage: Aqueous asymmetric supercapacitor. European Polymer Journal. 2024; 218: 113366. doi: 10.1016/j.eurpolymj.2024.113366
111. Mupit M, Islam MR, Azam MA, et al. Magnetic particle-filled polyaniline-doped graphene oxide nanocomposite-based electrode in application of supercapacitor. Energy & Environment. 2022; 35(4): 1987–2007. doi: 10.1177/0958305x221145185
112. Tale BU, Nemade KR, Tekade PV. Novel graphene based MnO2/polyaniline nanohybrid material for efficient supercapacitor application. Journal of Porous Materials. 2024; 31(6): 2053–2065. doi: 10.1007/s10934-024-01656-y
113. Itapu B, Jayatissa A. A Review in Graphene/Polymer Composites. Chemical Science International Journal. 2018; 23(3): 1–16. doi: 10.9734/csji/2018/41031

114. Chen W, Weimin H, Li D, et al. A critical review on the development and performance of polymer/graphene nanocomposites. Science and Engineering of Composite Materials. 2018; 25(6): 1059–1073. doi: 10.1515/secm-2017-0199
115. Abbas Q, Shinde PA, Abdelkareem MA, et al. Graphene Synthesis Techniques and Environmental Applications. Materials. 2022; 15(21): 7804. doi: 10.3390/ma15217804
116. Lobato-Peralta DR, Ayala-Cortés A, Duque-Brito, E, and Okoye PU. Synthesis and Characterizations of Nanocarbon. In: NanoCarbon: A Wonder Material for Energy Applications. Springer; 2024. pp. 17–34
117. Kostaras C, Pavlou C, Galiotis C, et al. Nanocarbon-based sheets: Advances in processing methods and applications. Carbon. 2024; 221: 118909. doi: 10.1016/j.carbon.2024.118909
118. Elsehsah KAAA, Noorden ZA, Saman NM. Current insights and future prospects of graphene aerogel-enhanced supercapacitors: A systematic review. Heliyon. 2024; 10(17): e37071.
119. Shalini S, Naveen TB, Durgalakshmi D, et al. Progress in flexible supercapacitors for wearable electronics using graphene-based organic frameworks. Journal of Energy Storage. 2024; 86: 111260. doi: 10.1016/j.est.2024.111260
120. Rani S, Kumar N, Sharma Y. Recent progress and future perspectives for the development of micro-supercapacitors for portable/wearable electronics applications. Journal of Physics: Energy. 2021; 3(3): 032017. doi: 10.1088/2515-7655/ac01c0
121. Gopakumar G, Sujith KV, Jayadevan S, et al. Portable Electronics and Microsupercapacitors. Supercapacitors and Their Applications. Published online February 10, 2023: 137–146. doi: 10.1201/9781003258384-9
122. Inshakova E, Inshakova A, Goncharov A. Engineered nanomaterials for energy sector: market trends, modern applications and future prospects. IOP Conference Series: Materials Science and Engineering. 2020; 971(3): 032031. doi: 10.1088/1757-899x/971/3/032031
123. Tusher MMH, Imam A, Shuvo MSI. Future and Challenges of Coating Materials. In: Coating Materials. Springer; 2023. pp. 229–251.
124. Kumar NA, Choi HJ, Shin YR, et al. Polyaniline-Grafted Reduced Graphene Oxide for Efficient Electrochemical Supercapacitors. ACS Nano. 2012; 6(2): 1715–1723. doi: 10.1021/nn204688c
125. Fan T, Tong S, Zeng W, et al. Self-assembling sulfonated graphene/polyaniline nanocomposite paper for high performance supercapacitor. Synthetic Metals. 2015; 199: 79–86. doi: 10.1016/j.synthmet.2014.11.017
126. Gao Z, Wang F, Chang J, et al. Chemically grafted graphene-polyaniline composite for application in supercapacitor. Electrochimica Acta. 2014; 133: 325–334. doi: 10.1016/j.electacta.2014.04.033
127. Jiang Y, Yan J, Wu X, et al. Facile synthesis of carbon nanofibers-bridged porous carbon nanosheets for high-performance supercapacitors. Journal of Power Sources. 2016; 307: 190–198. doi: 10.1016/j.jpowsour.2015.12.081
128. Kang YJ, Chun SJ, Lee SS, et al. All-Solid-State Flexible Supercapacitors Fabricated with Bacterial Nanocellulose Papers, Carbon Nanotubes, and Triblock-Copolymer Ion Gels. ACS Nano. 2012; 6(7): 6400–6406. doi: 10.1021/nn301971r
129. Wang F, Kim HJ, Park S, et al. Bendable and flexible supercapacitor based on polypyrrole-coated bacterial cellulose core-shell composite network. Composites Science and Technology. 2016; 128: 33–40. doi: 10.1016/j.compscitech.2016.03.012
130. Yao J, Ji P, Sheng N, et al. Hierarchical core-sheath polypyrrole@carbon nanotube/bacterial cellulose macrofibers with high electrochemical performance for all-solid-state supercapacitors. Electrochimica Acta. 2018; 283: 1578–1588. doi: 10.1016/j.electacta.2018.07.086
131. Walton IM, Cox JM, Benson CA, et al. The role of atropisomers on the photo-reactivity and fatigue of diarylethene-based metal–organic frameworks. New Journal of Chemistry. 2016; 40(1): 101–106. doi: 10.1039/c5nj01718a
132. Ma L, Liu R, Niu H, et al. Freestanding conductive film based on polypyrrole/bacterial cellulose/graphene paper for flexible supercapacitor: large areal mass exhibits excellent areal capacitance. Electrochimica Acta. 2016; 222: 429–437. doi: 10.1016/j.electacta.2016.10.195
133. Ma L, Liu R, Niu H, et al. Flexible and Freestanding Supercapacitor Electrodes Based on Nitrogen-Doped Carbon Networks/Graphene/Bacterial Cellulose with Ultrahigh Areal Capacitance. ACS Applied Materials & Interfaces. 2016; 8(49): 33608–33618. doi: 10.1021/acsami.6b11034
134. Sudhakar YN, Selvakumar M, Bhat DK, et al. Reduced graphene oxide derived from used cell graphite and its green fabrication as an eco-friendly supercapacitor. RSC Adv. 2014; 4(104): 60039–60051. doi: 10.1039/c4ra08347d
135. Benchikh I, Ezzat AO, Sabantina L, et al. Investigation of Hybrid Electrodes of Polyaniline and Reduced Graphene Oxide with Bio-Waste-Derived Activated Carbon for Supercapacitor Applications. Polymers. 2024; 16(3): 421. doi: 10.3390/polym16030421

Materials Technology Reports 2024, 2(2), 1518.
https://doi.org/10.59400/mtr1518

Review

Current research status of high-performance UHMWPE fiber: A review

Lei Li, Fanmin Kong, Ang Xiao, Hao Su, Xiaolian Wu, Ziling Zhang, Yutian Duan*

SINOPEC Nanjing Research Institute of Chemical Industry Co., Ltd., Nanjing 210048, China
*** Corresponding author:** Yutian Duan, duanyt9402.nhgs@sinopec.com

CITATION

Li L, Kong F, Xiao A, et al. Current research status of high-performance UHMWPE fiber: A review. Materials Technology Reports. 2024; 2(2): 1518. https://doi.org/10.59400/mtr1518

ARTICLE INFO

Received: 8 July 2024
Accepted: 6 September 2024
Available online: 4 October 2024

Abstract: In the relentless evolution of technological innovation, the incorporation of engineered materials across numerous sectors is becoming increasingly widespread. Among them, ultra-high molecular weight polyethylene (UHMWPE) fiber, as a novel type of engineered material, has emerged as a critical hot topic in industries such as aerospace, national defense, and new energy due to its exceptional physical and chemical properties. This article attempts to introduce the characteristics of UHMWPE fibers, including their advantages and areas for enhancement, to provide researchers with a comprehensive overview and research trajectory of UHMWPE. Moreover, this article succinctly elucidates the preparation methodologies and advances of UHMWPE fibers, encompassing mainstream dry and wet spinning methods, revealing their research trajectories, pivotal positions, and practical significance in the realm of engineered materials. In summary, this review briefly discusses the research overview and recent advances in UHMWPE fibers, which contribute to accelerating comprehensive and sustainable progress in this field.

Keywords: UHMWPE fiber; high strength; high modulus; gel-spinning; dry method; wet method

1. Introduction

With the deepening development of high-tech fiber preparation and application worldwide, high-performance fibers have achieved continuous innovation and breakthroughs, and have now entered a prosperous and rapid development period [1]. One of the world high-performance fibers is UHMWPE fiber, which is refined from UHMWPE through gel-spinning and high-ratio stretching processes [2,3]. The molecular weight (MW) of UHMWPE fiber ranges from 1×10^6 Da to 9×10^6 Da, combined with a high degree of orientation and a high degree of carbon-carbon bond strength, making UHMWPE fiber a material with high specific strength, high specific modulus, and low break elongation when compared to other conventional commercial fibers [2,4]. Since the successful development of the world's first UHMWPE fiber, Dyneema series fiber, by Dutch company DSM in 1979, researchers have innovated many excellent products, such as Allied Signal's Spectra series fiber and Mitsui's Tekmilon series fiber [5].

The preparation process of UHMWPE fiber is complex and diverse, mainly including high pressure solid extrusion, plastic melt spinning, surface crystal growth, super stretching or local super stretching, gel-spinning with hot stretching and other processes [6,7]. This type of fiber has extremely high strength and modulus, as well as characteristics such as low density (only 0.97 g/cm^3), excellent energy absorption performance, chemical corrosion resistance, impact resistance, non-water absorption, and high compatibility with living organisms [8]. Therefore, it has shown broad application prospects in the field of special materials and composite materials. In

particular, the emergence of UHMWPE fibers has successfully broken the monopoly of aramid fibers in the field of bulletproof materials and presented a trend of gradually replacing aramid bulletproof fibers [9]. Currently, UHMWPE fibers have been widely used in key fields such as marine industries, mooring ropes, fishing lines, medical equipment, engineering materials, daily necessities, aerospace, military industry and so on [10,11]. This article endeavors to elucidate the properties of UHMWPE fibers and the preparation techniques and advances of UHMWPE fibers, to equip researchers with a comprehensive overview and investigative trajectory of UHMWPE. We believe that these efforts will help accelerate innovative and sustainable progress in this area.

2. Advantages of UHMWPE fibers

The focus on UHMWPE fibers highlights their superior strength, modulus, wear resistance, low friction coefficient, chemical inertness and so on (**Figure 1**). These unique features contribute to their wide range of applications across various industries such as engineering, manufacturing, medical science, military equipment, fishing and rope, etc.

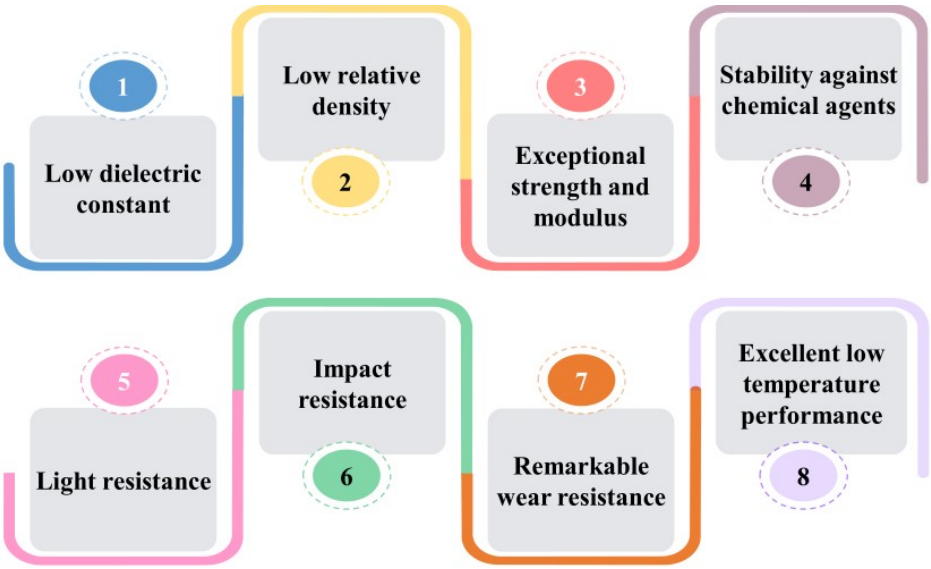

Figure 1. Schematic illustration of the advantages of UHMWPE fibers.

2.1. Low dielectric constant

The dielectric constant is a measurable property that quantifies a material response to an electric field. The dielectric constant of UHMWPE fibers falls in the range of 2.3–2.4 with the low loss tangent (0.003–0.02), rendering them particularly suitable for applications in high frequency radio waves [12]. When utilized as a radar cover, it exhibits superior radio wave transmittance (85%–99%). This indicates that when UHMWPE interacts with an electric field, its internal molecular architecture is less susceptible to polarity alterations. This trait of low dielectric constant renders UHMWPE proficient in electrical insulation, which confers significant application value in electronic devices [13]. For instance, in high-frequency circuits, UHMWPE can serve as a dielectric material to produce components such as microwave

waveguide tubes and capacitors. Moderate dielectric constant can mitigate transmission losses of electrical signals and enhance signal transmission quality. Concurrently, UHMWPE can also be employed to manufacture cable insulation layers and electrical insulation films, ensuring reliable electrical insulation performance.

2.2. Low relative density

Currently, a multitude of commercial UHMWPE fibers are available on the market with a specific gravity of 0.97 g/cm^3, making it the lightest of all high-performance fibers [8,14]. This value is notably lower than aluminum (2.7 g/cm^3) and steel (7.86 g/cm^3), two common metals used in engineering applications. Moreover, it is ~2/3 of aramid fibers (1.44 g/cm^3) and ~1/2 of carbon fibers (1.78 g/cm^3). The lightweight nature of UHMWPE fibers makes them an ideal candidate for use in various applications where weight reduction is critical. For example, they can be incorporated into sports equipment like tennis rackets and golf clubs to improve swing speed and reduce fatigue during long games. Similarly, UHMWPE fibers, due to their low density, are expected to be used as composite materials in fields such as automotive and component manufacturing [15], effectively reducing vehicle weight and contributing to energy conservation and emissions reduction.

2.3. Exceptional specific modulus and specific strength

UHMWPE fibers possess a substantial bond strength within the main chain. Moreover, its highly crystalline orientation confers the fibers high stiffness and strength. Meanwhile, UHMWPE fiber presently exhibits the highest specific strength among high-performance fibers, which is 15 times that of high-grade steel, 4 times that of glass and nylon 66, 2.6 times that of carbon fiber, and 1.7 times that of aramid fiber [16]. The fiber with an exceptional specific modulus (slightly lower than carbon fiber, but greater than any other fiber) is 2.5 times that of aramid [17]. Due to the elevated stiffness under conventional quasi-static conditions, it can induce high sound velocity propagation, rendering it superior to other fibers in energy absorption and stress wave transmission during bullet impact protection. Therefore, UHMWPE fiber is currently recognized as the fiber possessing the highest bulletproof performance.

2.4. Stability against chemical agents

UHMWPE fiber has a relatively simple chemical structure and is chemically inert, demonstrating excellent resistance to chemical corrosion and even higher resistance to chemical reagents when compared to other fibers such as aramids [18]. It exhibits robust resistance to a variety of chemical substances including acids, alkalis, salts and water, which exerts negligible influence on properties, structure and strength. Only a very limited number of organic solutions can slightly swell them with a mechanical performance loss of less than 10% [2]. The corrosion resistance of UHMWPE fibers is notably higher than that of aramid fibers when the strength retention rates of UHMWPE fibers and aramid fibers are compared in diverse chemical media. Note that its strength is only lost in sodium hypochlorite solution.

2.5. Light resistance

Owing to the robust chemical structure of UHMWPE fibers, their light resistance is also the utmost superiority among high-performance fibers [8]. After 1500 h of UV radiation, the strength retention rate remains at 90%. Notably, the strength retention rate of UHMWPE fibers is significantly higher than other fibers when compared to nylon and aromatic amides fibers [19]. Aramid fibers are not resistant to UV rays and can only be utilized when avoiding direct sunlight exposure [20,21].

2.6. Impact resistance

UHMWPE fibers exhibit excellent impact resistance, and their capacity to absorb energy and resist impact during deformation and shaping is higher than that of aramid fibers and carbon fibers [22,23]. In terms of impact resistance, the total absorption energy of UHMWPE fiber composite material is 1.8 times that of carbon fiber and 2.6 times that of aramid, and its bulletproof ability is 3.6 times that of aramid armor structure.

2.7. Remarkable wear resistance

The most important characteristic of UHMWPE is its remarkable wear resistance [24]. Notably, UHMWPE exhibits a low coefficient of friction, even in the absence of lubrication [25]. Its high MW and extensive polymer chains offer significant abrasion resistance, surpassing even polytetrafluoroethylene (PTFE), rendering it ideal for applications involving sliding or high friction elements [26]. This makes it an optimal material for applications where reduced friction is imperative, such as conveyor belts, bushings, and bearings [27].

2.8. Excellent low temperature performance

UHMWPE exhibits excellent low-temperature characteristics and can maintain its mechanical properties at temperatures below −80 °C [28]. This renders it an ideal material for use in extremely cold environments, such as cold regions or deep seas. For example, in the realm of construction, UHMWPE can serve as an effective ground and wall material in cold storage facilities. The material's ability to resist frost heave and maintain structural integrity in freezing conditions ensures optimal performance and durability.

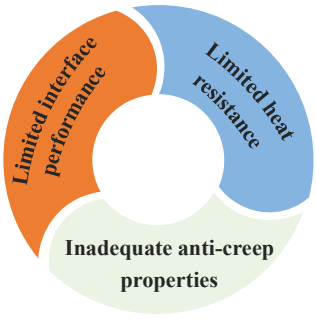

Figure 2. Schematic illustration of the issues that need to be improved in UHMWPE fibers.

3. Areas for improvement of UHMWPE fibers

UHMWPE fibers have certain drawbacks in terms of heat resistance, creep resistance, surface properties, etc. (**Figure 2**). However, these drawbacks do not hinder the unique advantages of UHMWPE fibers in multiple fields, such as protective materials, aerospace, industrial applications, etc. With the continuous progress of technology and the deepening of modification research, it is believed that these shortcomings will gradually be overcome and improved.

3.1. Limited interface performance

The exceptional hydrophobicity and lack of polarity exhibited by UHMWPE fiber renders it highly impervious to wetting [29]. Furthermore, the molecular structure of the surface of the UHMWPE fiber consists solely of methylene groups, which exhibit minimal reactivity with the surrounding matrix. The absence of reactive functional sites on the fiber surface effectively prevents it from forming covalent bonds with the resin [30]. As a result, the surface energy remains relatively low, preventing the resin from adhering easily; coupled with the absence of a roughened surface to facilitate mechanical interlocking, this significantly restricts its potential use in resin-based composite materials [31]. Owing to the inertness and non-polarity of UHMWPE fiber molecular chains, the interfacial viscosity strength between the fibers and the resin matrix is low, affecting the mechanical properties of UHMWPE fiber composites, particularly interlayer shear, transverse tension, and fracture toughness, thereby restricting their application to structural materials. Besides, there is such a class of self-reinforced composite materials, but it has been poorly studied, so it is rarely used.

Notably, in composite materials, resin serves solely as a connecting agent, whereas fibers are the primary force-bearing entity. A series of effects occur at the interface between fibers and the matrix, such as stress transfer effect and crack blocking effect in composite materials [32]. If the interface bonding force between the fibers and the matrix is not robust, cracks are prone to form at the interface and propagate in the direction of the fibers, resulting in debonding between the fibers and the matrix when the composite material sustains damage. Conversely, the adhesion between the fibers and the matrix is strong, and the diffusion of cracks is confined to a local range, resulting in a synergistic effect between the fibers and the matrix in the composite material, substantially enhancing the performance of the composite material [33]. Hence, interfaces with strong adhesion can effectively transfer stress from the matrix to the fibers. Consequently, when employing UHMWPE fibers for the production of armor proofing materials or integral structures, it is often necessary to apply surface treatments to augment their interfacial efficiency. However, surface modification can affect the strength of UHMWPE fibers, and careful consideration should be given when employing it. In current research, commonly utilized surface treatment methods encompass plasma treatment [34], corona discharge treatment [35], chemical oxidation (e.g., oxidative etching) [36], radiation-induced oxidation [37], radiation grafting [38], photo-induced crosslinking , etc. Occasionally, several methods are employed in combination to achieve superior results.

To improve the interfacial properties of UHMWPE fibers, Wu et al.

substantiated [39] the synergistic improvement in interfacial characteristics and resilience of UHMWPE fiber-reinforced polymer matrix composites (PMC) when subjected to oxygen plasma treatment. The oxygen plasma-treated UHMWPE/vinyl ester composites displayed a superior interface shear efficiency of 90.99%, significantly influencing the composite mechanical attributes. Optimal conditions were identified as an input power of 150–180 W, a duration of 120–150 s, and a gas flow rate of 8 sccm, resulting in a 10.67% increase in tensile strength, a 51.93% reduction in impact damage projection area, and a 24% decrease in dent depth. Concurrently, a gradual shift towards energy dissipation dominated by fiber fracture has been observed, optimizing fiber reinforcement and enhancing impact resistance. Yang et al. [40] introduced a novel physio-chemical alteration technique for enhancing interface compatibility between UHMWPE fibers and epoxy resins. The outcome revealed a significant increase in interfacial shear strength (IFSS), reaching up to 15.75 MPa, a 357% improvement over untreated UHMWPE fibers. Interestingly, the tensile strength of treated UHMWPE fibers decreased marginally by 7.3%, which was further validated by Weibull distribution analysis. Further findings indicated that the improved interface performance was due to roughened fiber surfaces and in situ grown groups, thereby improving the wettability between UHMWPE fibers and epoxy resins. Besides, Chen et al. [41] pioneered an innovative approach utilizing tannic acid (TA) to enhance the interface interaction between UHMWPE fibers and epoxy resins, yielding superior mechanical performance and enhanced hydrophilicity compared to virgin fibers. The IFSS of the modified micro-composite material escalated to 1.055 MPa, representing a significant 43.3% enhancement over the original UHMWPE fiber, while the tensile fracture strength and modulus rose by 28.0% and 49.4%, respectively. SEM images of the composite tensile fracture revealed substantial improvements in the interface characteristics of the TA-coated UHMWPE fiber and matrix. Notably, the doping of some inorganic compounds can also improve the interfacial properties of UHMWPE fibers, which helps to enhance their application in the field of composite materials. For example, Wang et al. [42] presented an innovative one-step, mild approach to fortifying the interfacial qualities of UHMWPE fiber-reinforced plastics. The resultant fibers exhibited enhanced surface roughness, polarity, and wettability due to their unique three-dimensional architecture and ample polar groups. Consequently, IFSS of these fibers increased 407.8%, reaching 8.36 MPa compared to untreated UHMWPE of 2.05 MPa. Analysis indicated that the failure mode shifted from adhesive to cohesive and substrate failure in the most robustly strengthened fibers. Moreover, in an effort to enhance the interfacial performance of UHMWPE fibers, Liu et al. [43] investigated the enhancement of interface stability in rigid polyurethane (RPU)/UHMWPE fiber composites through surface modification. They synthesized donut-shaped zinc oxide (D-ZnO) crystals on UHMWPE fibers, exploring their formation mechanism (**Figure 3**). The tensile strength of the D-ZnO-UHMWPE/RPU composite increased significantly by 127.9%, while impact toughness escalated by 155.2%. These results indicated that D-ZnO decoration can substantially improve the mechanical performance of these composites. Furthermore, it is suggested that the incorporation of D-ZnO-UHMWPE fibers into the RPU matrix creates additional crack propagation routes, thereby enhancing the toughness

of composites.

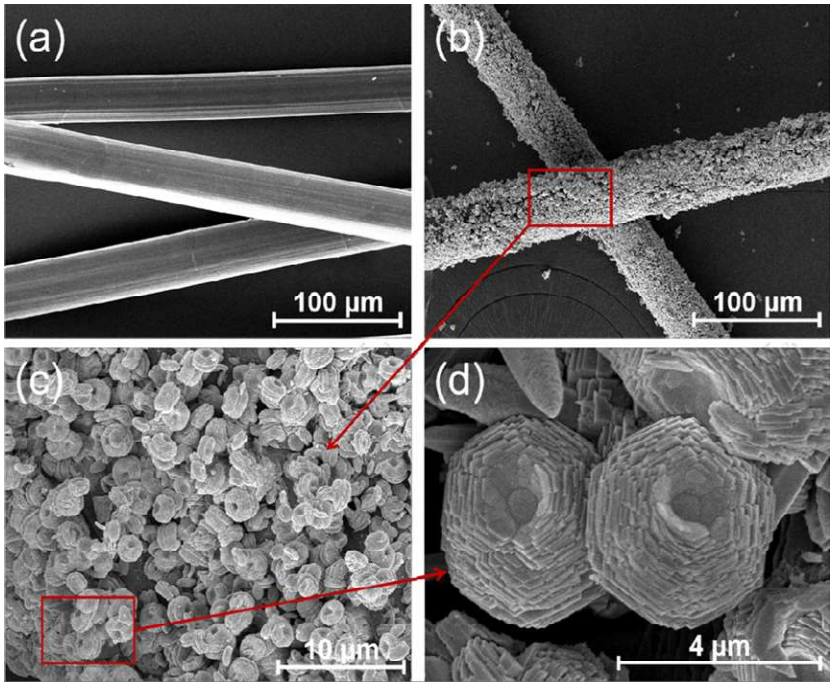

Figure 3. SEM images of the **(a)** untreated UHMWPE fibers; **(b)** D-ZnO-UHMWPE fibers; **(c)** Zoom-in views of (b); **(d)** Zoom-in views of (c). Reprinted with permission from reference [43], copyright American Chemical Society 2022.

3.2. Limited heat resistance

UHMWPE fibers demonstrate high crystallinity and orientation, small cross-sectional area of macromolecular chain, minimal melting point (T_m), and resulting restrained heat resistance [44]. In contrast to aramid fiber, this fiber is not resistant to high temperatures and melts at ~150 ℃, and application temperature is limited to 80–90 ℃ [45]. When employed at elevated temperatures, the strength diminishes and the creep resistance significantly escalates. When fabricating bulletproof backs and helmets, protection against blunt injuries may be compromised. Therefore, it is necessary to modify the heat resistance of UHMWPE fibers and significant progress has been made [46].

Recently, Liu et al. [44] have established an extensive fabrication procedure for elevated, through-plane thermal conductivity in UHMWPE fibers/PDMS unidirectional (UD) composites employing aligned UHMWPE fibers as filler and PDMS as matrix. At 400 ℃, the pure PDMS exhibited a weight loss ratio of ~2%, signifying excellent thermal stability. Up to 300 ℃, the weight loss ratio remained below 2%. Thus, the thermal stability of UHMWPE fibers/PDMS composites could fulfill the needs for practical application. Notably, with innovations in UHMWPE fiber via ultraviolet (UV) crosslinking, significant focus must be placed on its thermal aging characteristics and heat tolerance mechanism. Dong et al. [47] used UHMWPE fibers in varied forms, including full drawn yarn (FDY) and UV crosslinked FDY (UVFDY), and then subjected them to isothermal aging at 135 ℃. The impacts of thermal aging on their surface structure and mechanical attributes were initially examined and the findings affirmed that UVFDY is a heat-resistant

fiber. During an aging period of 10 h, numerous grooves appeared on the FDY surface, while the UVFDY surface remained free of patterns, showcasing its exceptional mechanical characteristics. This validates UVFDY as a heat-resistant fiber. Moreover, Yu et al. [48] employed air plasma and ZnO coating for modification of UHMWPE fibers. Results suggested that a dense, net-like nano-ZnO coating was observed on the treated fiber, and the fiber surface was activated via O-C = O group adsorption, enhancing the bonding strength between the nano-ZnO coating and the fiber. The plasma-treated fiber exhibited improved plating efficiency, a 19.7% enhancement in thermal stability post 120 s treatment, and a significant 177% increase in impact resistance following 90 s treatment.

3.3. Inadequate anti-creep properties

Considering that UHMWPE possesses a simplified macromolecular structure, with only van der Waals interactions between molecules, resulting in inadequate creep resistance and vulnerability to deformation under stress [49,50]. All these shortcomings significantly reduce its service lifespan and restrict its application range, such as in scenarios where continuous stress prevails in ropes and cables. Consequently, modifying UHMWPE fibers is a highly significant and meaningful research endeavor, particularly in the context of preserving their inherent superior performance [51]. The exploration of strategies to enhance the creep resistance of UHMWPE fibers and their continuous production holds significant theoretical and practical implications.

Notably, highly creep resistant UHMWPE fibers are predominantly utilized in ocean mooring cables, ship cables, and marine fisheries due to their exceptional creep resistance, yet traditional fabrication approaches of UHMWPE fibers emphasize post modification, severely restricting application in complex environments. Yuan et al. [52] synthesized granulated hydroxylated UHMWPE via ethylene/10-undecenoic acid triisobutylaluminum copolymerization under a titanium catalyst, i.e., [^{t}BuNSiMe$_2$(2,7-^{t}Bu$_2$Flu)]TiMe$_2$. The resulting polymer powders underwent gel-spinning and heat-drawing to form hydroxylated UHMWPE fibers, exhibiting enhanced creep resistance and hydrophilicity with preserved tensile strength. Notably, the fiber creep rate decreased significantly from 0.52% of regular UHMWPE to 0.32% of UHMWPE-OH. Hence, minimal incorporation of hydroxyl moieties in UHMWPE contributes significantly to fiber creep resistance due to the high bond energy (21 kJ/mol) of hydrogen bonds within the polymer chain, surpassing the intermolecular slip force (0.4 kJ/mol–4.0 kJ/mol). The blend fiber showed a reduced creep rate (0.48%) and improved tensile strength (17.5 cN/dtex) over commercial UHMWPE fiber (1.01%, 14.2 cN/dtex), indicating potential for UHMWPE-OH powder as a blend modifier. Besides, Li et al. [53] employed wet spinning to produce UHMWPE fibers, subsequently modifying their surface via hydrolysis and condensation reactions. Examination of the chemical structure, thermal stability, and micromorphology revealed an interlaced network on the fiber surface, accompanied by reduced crystallinity, minimal thermal stability, and diminished molecular chain mobility. This unique methodology increased creep resistance in modified fibers by over 50% compared to untreated UHMWPE fibers.

This study successfully amalgamated UHMWPE spinning and surface modification techniques, thus substantially enhancing the creep resistance of UHMWPE fibers.

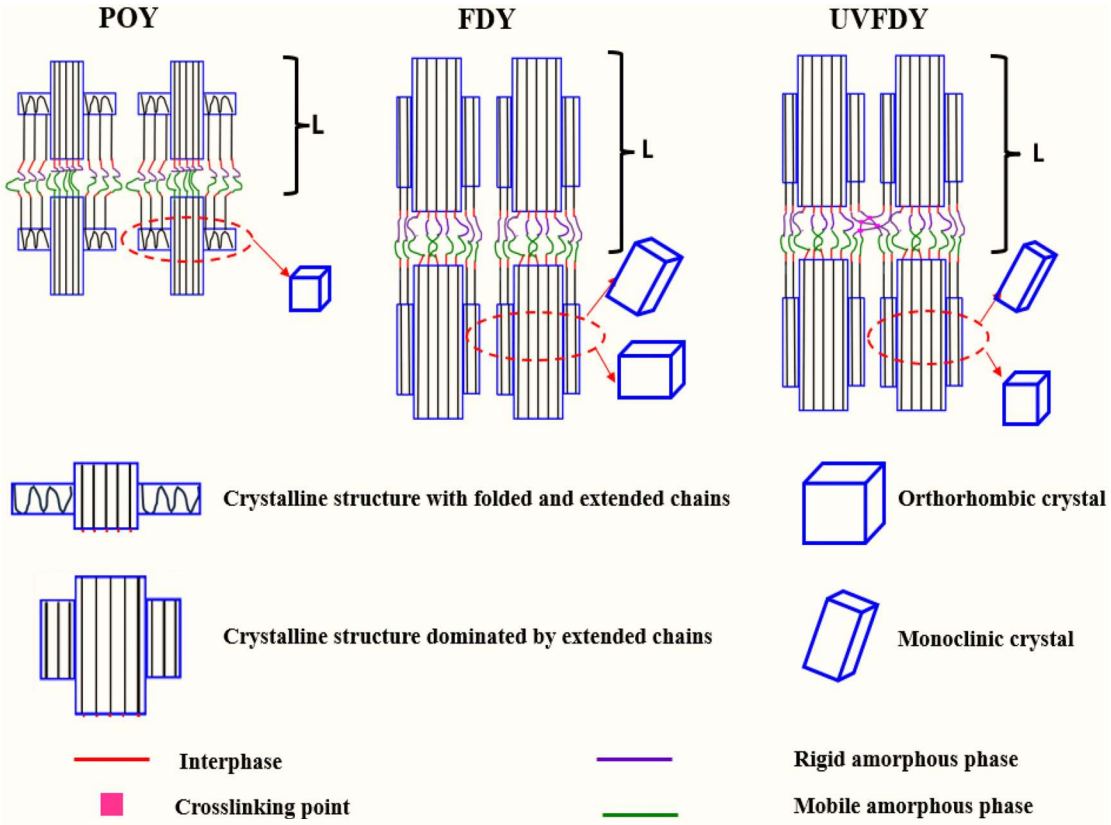

Figure 4. Schematic illustration for the structure evolution model of UV crosslinked UHMWPE fiber during processing. Reprinted with permission from reference [54], copyright John Wiley and Sons 2024.

Despite improvements in UHMWPE fiber for heat and creep resistance via UV cross-linkage, the impact on fiber structure during processing is crucial. Dong et al. [54] inspected UHMWPE fiber in varied states including pre-oriented yarn (POY), FDY, and UVFDY using differential characterization methods (**Figure 4**). They further assessed the heat and creep resistance of UVFDY through temperature at break (T_b), glass transition temperature (T_g), time at break (t_b) under specific aging conditions, and creep elongation (L_c). Their findings revealed UVFDY with high gel content (89.0%), crystallinity (84.2%) and orientation (91.7%). These attributes endowed UVFDY with exceptional mechanical strength and heat/creep resistance, particularly evident in its elevated T_b (220 °C), T_g (−75.7 °C) and t_b (20 h) along with decreased L_c (7.8%). This study sheds light on the structural-functional correlation of UVFDY, aiding future developments of UV crosslinked UHMWPE fibers with enhanced heat and creep resistance. Besides, using electron beam (EB) radiation crosslinking, Wen et al. [55] developed a high creep resistance UHMWPE fiber, demonstrating increased thermo-stability, reduced crystallinity, and substantial cross-linkages as compared to the initial sample. Note that the gel content of the crosslinked fiber ascended to 88%, indicating enhanced cross-linking in the amorphous phase, thereby minimizing molecular slip. Notably, the room temperature creep extension of radiatively treated fibers dwindled by over 30%. When compared with untreated UHMWPE fibers, cross-linked UHMWPE fibers exhibited superior

creep resistance under diverse ambient conditions (60 ℃, 90 ℃ and 120 ℃), with negligible creep expansion observed during irradiation with 100 kGy. This study introduced a streamlined methodology for fabricating and evaluating high creep resistance UHMWPE fiber, paving the way for its broader utilization, especially in military protective gear.

4. Gel-spinning of UHMWPE fibers

4.1. Gel-spinning and its mechanism

The mainstream manufacturing process of UHMWPE in industry is called gel-spinning, which can be classified as dry spinning method and wet spinning method [17,56]. The former employs a high volatile solvent for the dry gel-spinning process, while the latter utilizes a low volatile solvent for the wet gel-spinning process. The solvent utilized and subsequent procedures are the primary distinctions between these two process routes [57]. Owing to the substantial disparities in the attributes of the two types of solvents, subsequent solvent recovery processes are also completely distinct, each possessing its own unique advantages. Gel-spinning mechanisms are intricate, prompting numerous investigations of UHMWPE spinning mechanisms, which is mainly based on the theory of entanglement and disentanglement of polymer chains [58–60]. There is a well-established outline elucidating the basic mechanism of UHMWPE fiber gel-spinning. Primarily, the UHMWPE solution undergoes heating and shearing within the extruder to form polymer fibers. At this point, polymeric crystals within the fiber are disentangled, thereby establishing a preferred alignment between the polymer chains within the fibers. Subsequently, the disentangled polymer chains in the fiber are forced to align further. The elevated drawing ratio endows the orientation of the chains in the fiber, which also instigates high crystallinity. By drawing, the crystallinity of the polymer can reach up to 85 % compared to crystallinity below 60 % in PE fibers with low polymer orientation [61]. Given that UHMWPE polymer chains within the fiber are highly oriented in specific directions, the fibers exhibit a highly anisotropic behavior. While mechanical properties such as tensile strength (up to 2.9 GPa with Young's modulus of 101 GPa) and stiffness along the fiber orientation are extremely high, axial compression and transverse strength are diminished due to the weak interaction of polymer chains with each other [62].

Notably, the advanced understanding of UHMWPE gel-spinning mechanism is also perpetually enhanced and refined. Recently, Wang et al. [17] elucidated the influence of entanglements and intracrystalline chain dynamics on UHMWPE mechanical traits, explored disentangled UHMWPE crystal construction theories, and deduced the rationale behind the superior modulus and strength of final fiber. Significantly, they deduced that utilization of high molecular weight PE resins diminishes both the defect fraction at chain termini and also lessens the entanglement concentration (i.e., ϕ_e). A higher entanglement magnitude per polymer chain at a specific concentration bolsters the stability of the gel framework, inhibiting the formation of individual crystals. Additionally, immersing UHMWPE resins in solvents like decalin and paraffin, yielding dilute solutions, mitigates entanglement density, with this disengagement potentially preserved post crystallization, yielding

superior ultrafine drawability. Meanwhile, Sun et al. [58] established the entropy-viscosity model, facilitating the correlation between the tangible macroscopic determinant (drawing stress) and the microscopic quantity (macromolecular entanglements). The study revealed that the trend in the N_skT parameter, reflecting the chain-slippage within the slip links during extension on spinning lines, supports the observation of a peak in each relationship curve linking the tensile strength and modulus of UHMWPE fibers through the maximum solid-state draw-down ratio. This indicates the "disentanglement on the spinning line" molecular motion mechanism. As these entangled molecules are incorporated into the flowing units, their apparent count decreases. Notably, molecular entanglement numbers, derived from theoretical fitting to pre-draw and post-draw data, have escalated dramatically, mainly due to agglomeration rather than topological entanglements. Besides, Wang et al. [63] utilized in situ wide-angle X-ray diffraction (WAXD), small-angle X-ray scattering (SAXS) and SEM to scrutinize the structural evolution from shish-kebab to fibrillar crystals of UHMWPE fibers fabricated from dilute solution during the hot-stretching procedure. As the hot-drawing strain escalates, kebab crystals (lamellae) exhibit stress-induced breakage and recrystallization at 90 ℃, 100 ℃, and 110 ℃, and fusion followed by recrystallization at 120 ℃, transforming into fibrillary structures. Remarkably, the length of pre-fiber shish initially increases steadily at each strain level before decreasing slowly, while their numbers persistently increase and diameter widens gradually until reaching constant. Regardless of the strain temperature, the crystallinity index exceeds 0.9 throughout the entire stretching procedure. These findings suggest that shish-kebab crystals in low-concentration polyethylene fibers can seamlessly transition into fibrillar form through hot stretching technology.

4.2. Dry method gel-spinning

The dry spinning process route primarily utilizes decalin as the spinning solvent, which is blended with UHMWPE resin, and subsequently undergoes high-temperature shearing, blending, and spinneret extrusion in a twin-screw extruder to form a melt flow [64,65]. The solvent is eliminated by blowing with inert gas (i.e., N_2) and other techniques, and the melt solidifies into precursor fibers that can be rolled and shaped. UHMWPE fibers with high strength and modulus can be obtained by subjecting the precursor fibers to high multiples of heat stretching (**Figure 5**). Compared to wet spinning, dry spinning possesses a more streamlined procedure, is cost-effective and environmentally friendly, and produces fibers with a smooth surface, fewer defects, softness, high crystallinity, high fiber density, high T_m, short melting range, and low solvent residue. Notably, the crucial process technology of the dry process route principally comprises the following aspects. Initially, the swelling process of the resin in decalin solvent is critical for uniform dissolution of the spinning solution. Subsequently, uniform discharge of the spinning solution is the critical determinant of fiber dimensions. Further, proficient volatilization of solvents in precursor fibers is the critical factor impacting solvent recovery and mechanical characteristics of final fibers. Ultimately, thermal tensile temperature, tensile ratio, and tensile velocity are the principal determinants of fiber

crystallization and mechanical properties.

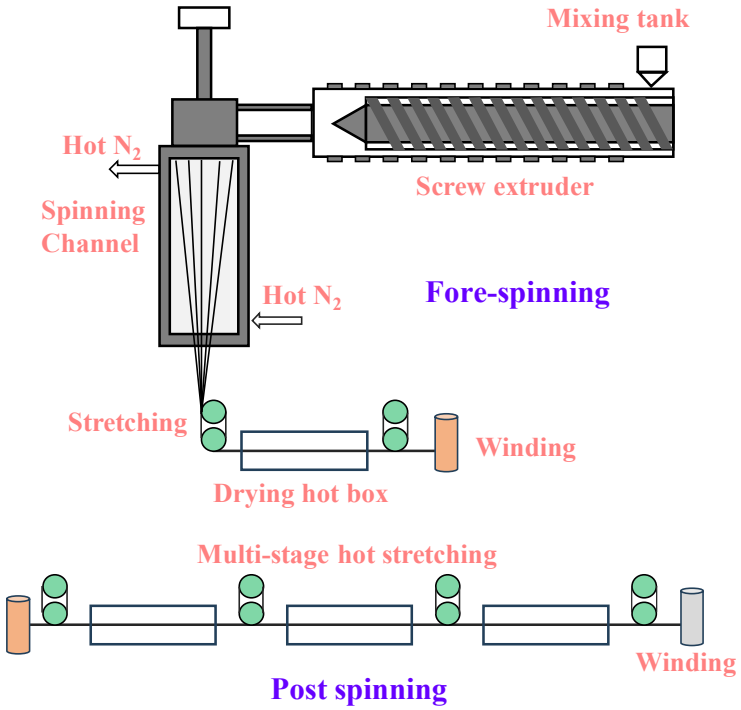

Figure 5. Schematic illustration of dry method gel-spinning of UHMWPE fibers.

Recently, Wang et al. [65] produced UHMWPE fibers via the dry spinning process with an UHMWPE resin viscosity-average MW (Mv) of 600 × 10^4 Da, observing structural transformation during hot-drawing. UHMWPE (6%) was incorporated into decalin and fed into a twin-screw extruder. Processing parameters were set above the T_m of UHMWPE and the solvent boiling point (189 °C). Then pre-drawing was executed in a hot box to generate initial fibers with a draw ratio of ~10. Hot-drawing with varying DRs of 10–75 yielded tensile strengths of 4.49 cN/dtex–35.04 cN/dtex. Notably, as DR increased, fiber linear density initially diminished, attaining a maximum of 83.5 N at DR 40, indicating stress orientation of amorphous phase molecules and orthorhombic crystal formation. Moreover, chain slip occurred at higher DRs, diminishing fracture force but augmenting fiber strength. Note that a shoulder peak appeared on differential scanning calorimetry (DSC) curves at 154 °C, accompanied by three unique peaks in the X-ray diffraction pattern, i.e., (001) at 2θ of 19.3°, (110) at 2θ of 21.6°, and (200) at 2θ of 24.1°. As DR increased, the average grain size of these planes decreased, indicating enhanced fiber structure integration. Furthermore, Ding et al. [59] fabricated 7 diverse types of fibers by dry spinning technique, encompassing raw fibers (with high fracture strain) and final fibers with varying fore-spinning and post-spinning draw ratios. Initially, UHMWPE powder was mixed into decalin (6 wt%), fed into a twin-screw extruder for complete dissolution, and extruded through a spinneret via a metering pump. A gel fiber formed after cooling and pre-drawing at 80 °C–100 °C in a drying box, yielding a dry raw fiber. Findings indicated that the fiber's tensile strength obeyed the Weibull distribution, which located in the range of 24.72 cN/dtex–36.84 cN/dtex. Interestingly, pre-spinning spinneret's draw ratio significantly affected the strength

distribution. Diverse drawing methods altered the fiber's fracture mechanism as confirmed by DSC and the taut tie molecules (TTMs) fraction analysis. Notably, Weibull distribution parameters signified fiber quality, while Weibull modulus correlated with fiber property dispersion and processing conditions. The characteristic strength corresponded to the mean test stress, indicating its efficacy as a metric for fiber reliability in practical use.

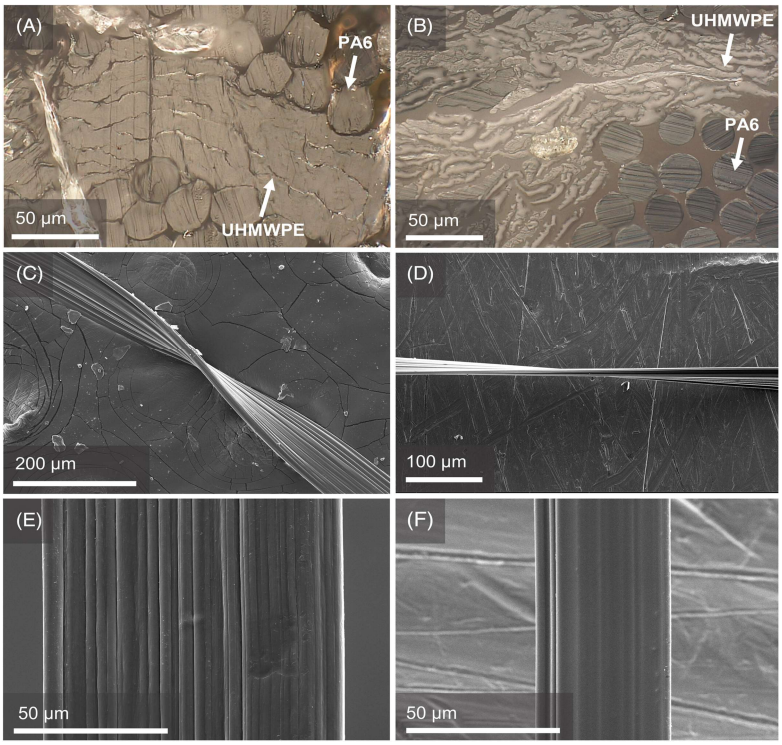

Figure 6. Cross-sectional optical microscope images of (A) as-spun; and (B) drawn UHMWPE fibers using cross-sectional polyamide 6 (PA6) fibers as mounting filler, and scanning electron microscopy (SEM) images of twisted; (C) as-spun fiber; and (D) drawn fiber, and SEM side view of; (E) as-spun fiber; and (F) drawn fiber. Reprinted with permission from reference [66], copyright John Wiley and Sons 2024.

In view of the common utilization of hazardous petrochemicals in large-scale UHMWPE fiber manufacturing, it's noteworthy that orange terpenes, a byproduct of citrus fruits, can serve as an environmentally friendly bio-degradable alternative. Brown et al. [66] have thoughtfully conducted research on ultrafine UHMWPE fibers utilizing orange terpenes as a solvent with a 5:1 dilution ratio (**Figure 6)**. The process involved preparing a blend of UHMWPE and orange terpenes by heating a solution containing both substances above the T_m of UHMWPE, followed by the addition of the polymer while stirring. The blend was instantly introduced into a preheated extruder barrel (130 ℃), allowing it to stabilize for 5 minutes. The nozzle featured a round aperture of 250 μm diameter and approximately 500 μm length. Extrusion was executed at 130 ℃, with a syringe pump operating at a rate of 0.07 mL/min. The extruded filament extruded through a 10 cm air void into a room temperature deionized water coagulation bath, lingering for about 68 cm before being coiled onto a spool at a speed of 2.5 m per minute. The resulting fibers

displayed a smooth, micrometer ribbon cross-sectional profile, optimally configured for high fiber volume fraction composites. Post-extrusion, the fibers demonstrated enhanced tenacity (8.6 cN/dtex) and modulus (229.2 cN/dtex). This investigation effectively underscores the prospective application of orange terpenes as an environmentally conscious solvent for UHMWPE gel-spinning, establishing a platform for future process enhancement initiatives pertaining to these fibers. Interestingly, shape memory polymer fibers (SMPF) including UHMWPE fibers, a significant component of smart fabrics, are applied in textiles, polymers, and medicine, such as surgical sutures and medical devices. Li et al. [67] developed external stress-free two-way SMPFs using UHMWPE matrix based on gel-spinning and hot-drawing of UHMWPE to yield raw fibers. A blend of UHMWPE powder (12.66 g) and Irganox 1010 (0.09 g) in decalin (1000 g) was heated to 155 ℃ under mechanical stirring for 150 min. The resulting transparent UHMWPE solution (1.25 wt%) was injected into a glass syringe maintained at 155 ℃ via a heater. Filaments were formed by extrusion through a 1.5 mm syringe needle, which was then cooled in an ice petroleum ether bath to form a gel fiber. Subsequently, the gel fiber was dried at room temperature for 24 h before being hot-drawn thrice at 100 ℃, 110 ℃, and 120 ℃ to produce raw UHMWPE fibers. After programming, these UHMWPE fibers exhibited high tensile strength (338.72 MPa) and Young's modulus (2287.34 MPa), along with one-way SME, quasi-two-way SME, and external stress-free reversible two-way SME, with a reversible strain of 27.42%. These fibers can be utilized to fabricate artificial muscles and actuators, which can lift over 250 times their own weight with a reversible strain of ~10%. Given their simplicity in preparation and programming, they are suitable for industrial mass production.

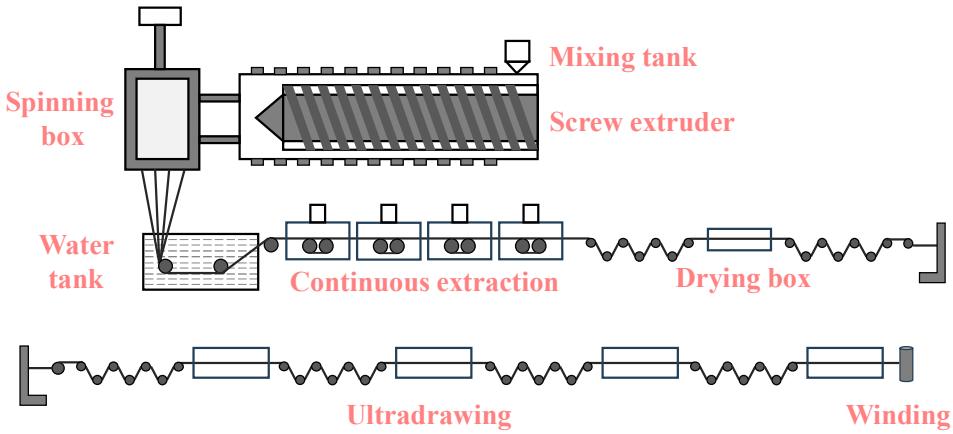

Figure 7. Schematic illustration of wet method gel-spinning of UHMWPE fibers.

4.3. Wet method gel-spinning

Notably, the wet method technique was first incorporated in 1985 following licensing DSM patents from Honeywell in the United States [68]. The primary fiber grades launched encompass the Spectra series items, with Spectra-HT grades with tensile strength of up to 40 cN/dtex [69]. In addition, Mitsui Corporation of Japan formally launched the manufacture of Tekmilon UHMWPE fiber in 1988, targeting the markets for work gloves, cables, and fishing lines. Contrasting vastly with the dry spinning method, the wet spinning technique employs a non-volatile spinning

solvent with a high boiling point, such as naphthalene, paraffin oil and other hydrocarbons including kerosene, white oil, mineral oil, etc. [70]. Consequently, the spinning processing temperature can be varied over a wide range. The spinning material is extruded through a spinneret and subsequently condensed and solidified in a water bath to yield frozen precursor fibers [71]. Subsequently, the spinning solvent necessitates to be extracted and dried at the latter stage of spinning (**Figure 7**). Commonly utilized extractants encompass xylene, dichloromethane, hydrocarbon cleaning agents, etc. Note that after more than a decade of industrial evolution, the spinning solvent recovery process is relatively straightforward and mature, yet there persist the issues of residual solvent, escalating pressure on environmental protection and safety. From the appearance, there is no obvious difference between the precursor fibers and the final fiber product, but the product fibers usually have a low denier (**Figure 8**). Generally, gel-spinning is currently a more widespread method in fiber yarns that is capable of preparing products with excellent morphology and regularity in industrial production.

(a) **(b)**

Figure 8. Schematic diagrams of UHMWPE **(a)** precursor fiber; and **(b)** final fiber product.

The progress of wet processing methods stems from the inherent drawbacks of the traditional wet processing method, which impact the uniformity of product quality, particularly the fiber diameter deviation is typically substantial. Refining the existing process route to further enhance the mechanical properties, stability, and functionality of fibers is currently the research focus of wet processing methods. For example, considering the harsh conditions during the decomposition of UHMWPE fibers caused by heat and shear heavily decimates the MW of UHMWPE, Hu et al. [72] successfully facilitated the dissolution of UHMWPE in paraffin oil whilst circumventing substantial degradation, thereby enhancing fiber tensile strength. The application of gel-spinning utilizing supercritical carbon dioxide (SC-CO_2) treated UHMWPE/paraffin oil suspension yielded fibers possessing superior MW preservation and disentanglement efficacy. Significantly, the tensile strength of SC-CO_2-modified UHMWPE fibers reached 30.11 cN/dtex, an appreciable augmentation of 10.3% compared to untreated counterparts, with a modulus of 1328.71 cN/dtex. Furthermore, the thermal and crystallization attributes of the modified fibers were enhanced. Thorough examination of the thermo-mechanical,

mechanical, and crystalline properties of these fibers indicated that SC-CO_2 treatment notably enhanced MW and disentanglement of UHMWPE gel fibers, as demonstrated by both thermo-mechanical and rheological assessments, corroborated by cross-sectional morphologies of the fibers. Similarly, Wang et al. [73] utilized decalin (dec) as a pre-soaking agent to optimize the UHMWPE solubility in paraffin oil, avoiding severe deterioration, thereby producing UHMWPE fibers with high MW preservation and low tangled structure (**Figure 9**). UHMWPE fibers are prepared using gel-spinning and hot-drawing techniques. Among them, the UHMWPE/dec-s-3 sample, where UHMWPE was pre-soaked in a decalin solution at a mass ratio of 3:1, exhibited the highest MW. Notably, the entanglement of UHMWPE fibers from this sample is noticeably less dense than those from UHMWPE-neat or other swollen samples. Furthermore, the tensile strength and modulus of UHMWPE/dec-s-3 fibers increased significantly, reaching 31.41 and 1446.26 cN/dtex, an increase of 15.1% and 14.3% over UHMWPE-neat fibers. Additionally, the thermal and crystallization properties of UHMWPE fibers from swollen UHMWPE are enhanced. Moreover, investigation by Yu et al. [74] delved into the structural characteristics and functional performance progression of UHMWPE fibers generated via industrial manufacturing plants, incorporating draw ratios of up to 54.5. This study used. This study utilized advanced analytical tools such as DSC, WAXD and SAXS. The UHMWPE fibers, fabricated from 8 wt% paraffin oil emulsion, encompassed 60 filamentary yarns per bundle. Initially, the paraffin oil concentration in the unprocessed fibers approximated 75 wt%, with a residual content of 2.0 wt% after extraction. Findings revealed considerable augmentation in amorphous molecular chain alignment and crystallinity during preprocessing, but no discernible alteration in fiber mechanics. Initial drawing led to an elevation in crystallinity and orientation from 68% to 81% and 0.88 to 0.97, respectively, accompanied by substantial increments in modulus and tensile strength (29.5 cN/dtex to 878.1 cN/dtex and 4.3 cN/dtex to 21.1 cN/dtex). Subsequent steps of drawing accentuated the monoclinic phase content, substantially contributing to the ongoing fortification of mechanical attributes.

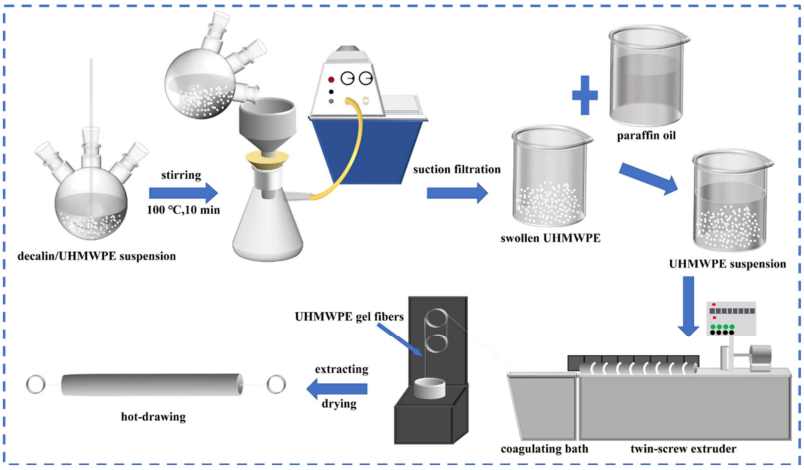

Figure 9. Schematic illustration for the preparation process of UHMWPE fibers by regulating the dissolving system to enhance mechanical properties. Reprinted with permission from reference [73], copyright John Wiley and Sons 2022.

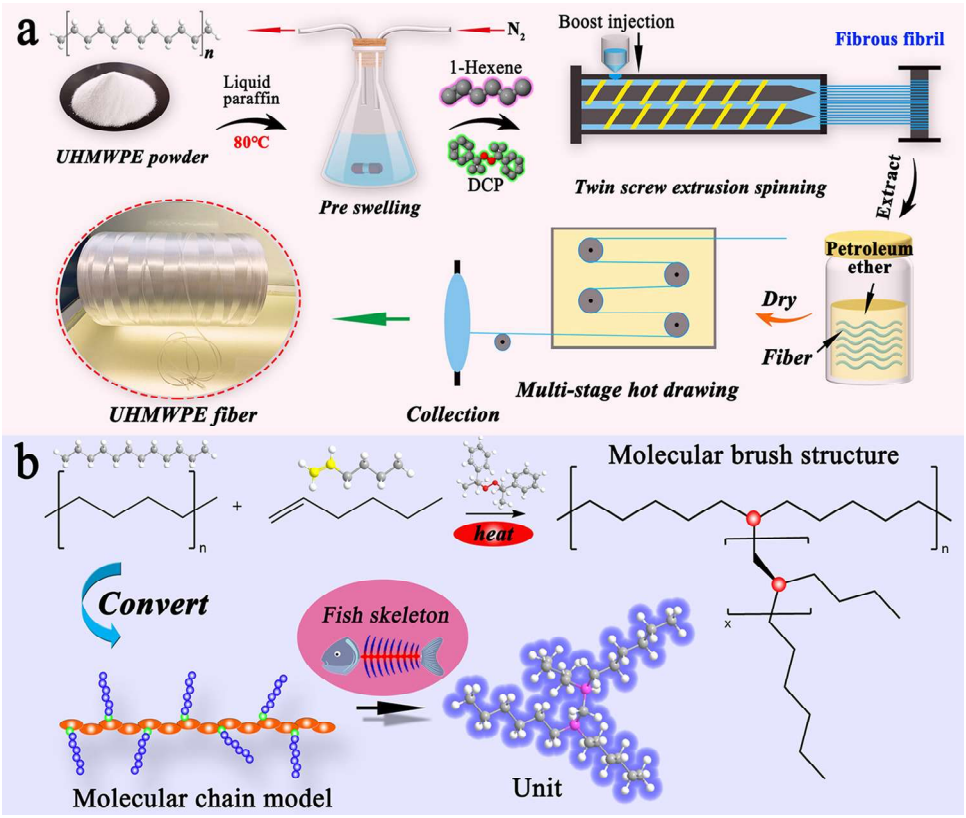

Figure 10. Schematic illustration for the **(a)** online fabrication process; **(b)** mechanism of modification of a highly creep-resistant UHMWPE fiber. Reprinted with permission from reference [75], copyright American Chemical Society 2024.

The advancement of UHMWPE fibers possessing distinct functionality, accompanied by the materialization of UHMWPE fibers suitable for practical deployment, represents an ongoing evolution in this specialized field. For example, Yang et al. [75] innovated highly creep resistant UHMWPE fibers mimicking the molecular architecture of a fish skeleton **(Figure 10)**. They formulated a spinning blend comprising UHMWPE (10%), an antioxidant, and liquid paraffin, which was subjected to stirring and swelling for 6 h at 80 °C followed by the addition of *n*-hexene (at 1 wt%, 3 wt%, 5 wt%) and diisopropylbenzene peroxide. This blend was subsequently restituted in a pressurized dissolving kettle for 1 hour before being fed into a twin screw for additional swelling and extrusion. A raw UHMWPE wire was prepared by inserting a 1.0 mm diameter spinneret into a cooling tank. Solvent-free UHMWPE filaments were extracted and subjected to thermal drawing, resulting fiber with tensile strength of 26 cN/dtex–30 cN/dtex and modulus of 800 cN/dtex–1268 cN/dtex. Melt-grafting spinning and hyperthermal drafting were used to produce modified UHMWPE fiber products with improved polymer chain slip hindrance. Notably, raising the monomer concentration to 5.0% notably decreased elongation from 8.5% to 2.5% at 70 °C, representing a substantial improvement (over 70%). This approach effectively overcomes traditional industrial modification limitations, online spinning modifications, and high creep resistance, making it a practical and economical solution. Hu et al. [76] developed advanced abrasive UHMWPE fibers by gel-spinning, utilizing an 8 wt%–16 wt% UHMWPE formulation via a single-hole spinneret, extraction, drying, and drawing methods.

The incorporation of dispersed UHMWPE powder and antioxidant 1076 (0.7 wt%) into paraffin oil yielded 8 wt%, 10 wt%, 12 wt%, 14 wt%, and 16 wt% UHMWPE gel-spinning solutions. The fiber tensile strength attained values ranging from 23 cN/dtex–30 cN/dtex, while the modulus ranged from 882 cN/dtex–1103 cN/dtex. Moreover, the influence of solution concentration on solvent phase separation, crystallinity, erosion protection, and mechanical properties was evaluated. The findings revealed that elevated solution concentration can expedite phase separation equilibrium, thereby curtailing production duration. The wear resistance improved by almost 3-fold with a 2-fold solution concentration and a doubling of UHMWPE monofilament density. Despite marginal reductions in MW and tensile strength, enhanced erosion resistance and rapid phase separation equilibrium render this method advantageous, substantially bolstering the utilization of UHMWPE fibers in civil engineering applications.

5. Recent advances in UHMWPE fibers-based composite materials

The employment of UHMWPE fiber, renowned for its exceptional strength-to-weight ratio, robust tenacity, and supreme chemical and abrasive resistance, is deemed to be the most advantageous reinforcement element. Nonetheless, substandard interaction and compatibility between UHMWPE fibers and polymeric matrix has hindered the progress of UHMWPE composites with superior properties. To mitigate this issue, ongoing contemporary investigations have focused on surface modification of UHMWPE fibers and UHMWPE/polymer interfacial interactions. For instance, the physico-chemical approach involving plasma modification and polypyrrole (PPy) grafting was adopted by Yang et al. [77], to enhance the impact resistance of UHMWPE fiber/epoxy composites at low velocities. Two distinct gas compositions, N/O (N_2:O_2, 5:5) and pure N_2, were utilized in plasma processing. Polypyrrole was applied after treatment and residual compression strengths for impacted laminates were measured. Results showed compression strength of 30.9 MPa and 30.4 MPa for PP-N/O and PP-N_2 composites, respectively, and 25.9 MPa and 22.1 MPa for PM-N/O and PM-N_2 composites, respectively. Comparative analysis indicated significant improvements in impact resistance and residual strength following combined plasma treatment and polypyrrole grafting, accompanied by a notable reduction in void fraction. Notably, the impact resistance of a single physical plasma treatment was primarily influenced by the N_2-O_2 ratio. Besides, cyanate (CE) resin and UHMWPE fiber are pivotal constituents serving as matrix and reinforcement, respectively, for facilitating lightweight, high wave transparency within composites. Nonetheless, compatibility barriers may pose challenges in composite manufacturing, therefore Jiang et al. [78] overcame this obstacle through the utilization of the polysulfide catalyst (PSC), which accelerated the curing process of CE resin, thereby lowering its activation energy and the required molding temperature (**Figure 11**). The observed activation energy of the CE-PSC resin was reduced from 107.2 kJ mol^{-1} to 60.7 kJ mol^{-1}, with a T_g of 257.2 ℃ and flexural and tensile strengths of 120.2 MPa and 60.8 MPa, respectively. Accordingly, the CE-PSC/UHMWPE fiber composites fabricated at an optimized molding temperature of 135 ℃, exhibit remarkably low density (1.05 g

cm^{-3}), low dielectric constant (2.4), minimal dielectric loss (0.006), and superior wave transmittance (92.2%). Thus, these composites possess considerable potential in the field of lightweight, high wave-transparent materials.

Considering the recent focus on material ballistic threshold and single hit behavior, Xiang et al. [79] presented a novel method to probe the multi-point asynchronous impact responses and damage mechanisms of UHMWPE fibers, aiming to elucidate why there are significant variations in the ballistic threshold and energy absorption capacities of UHMWPE fiber composite panels, depending on their impact separation. By leveraging CT scanning and DIC (Digital Image Correlation), delamination extent and dynamic response can be quantified. The results indicated that the ballistic threshold of the subsequent impact increased by 3.05% at an impact distance equal to 2.5 dm of the bullet. Despite interference within the damaged zone, the maximum disparity in energy absorption between consecutive impacts remains limited to 3.7%, even at impact separation of 5 dm of the bullet. Thus, from the point of view of energy absorption, the two impacts remain independent. Overall, multi-impact testing is critical for protective materials, and this study provides valuable insights into the multi-impact performance of UHMWPE fiber laminates. Qiao et al. [80] examined a class of composites designated as thermoplastic polymer-fiber-reinforced polymers (PFRPs), commonly referred to as self-reinforced composites (SRCs). As an example, they utilized unidirectional (UD) UHMWPE fibers embedded in a high-density polyethylene (HDPE) matrix for optimal PFRP. They exposed the filament-wound PFRPs, possessing varying fiber volume fractions (V_f), to rigorous experimental examination under different compression molding temperatures and pressures. The maximum specific tensile strength and modulus of PFRP laminas achieve values of 600 MPa/(g/cm^3) and 31 GPa/(g/cm^3), respectively. These parameters rival those of glass-/aramid-fiber-reinforced polymers, with PFRPs showcasing superior ductility (specific strain at peak load of ~4%/(g/cm^3)) compared to other prevalent polymer composites. Moreover, Liu et al. [81] formulated an innovative environment-friendly, formaldehyde-free impregnation solution for improving the interfacial bond between UHMWPE fiber cords and rubber. Prior to impregnation with a blend of glycerol triglycidyl ether (GTE), diethylenetriamine (DETA), and vinyl pyridine latex, the UHMWPE fiber cords undergo treatment using dopamine (DA) and N-(β-aminoethyl)-γ-aminopropylmethyldimethoxysilane (KH602). The data showed no adverse effect on post-impregnation fiber strength and a 257% increase in bond strength between the modified fibers and rubber as demonstrated by H pull-outs results. Subsequent to impregnation, significant fiber strength was maintained. When equating GTE/DETA to proportion of 5:1.5, the resulting H pull-out resistance and 180° peel strength for UHMWPE-PK-Resorcinol-formaldehyde-latex (RFL) fiber cord/elastomeric composites increased to 52.7 N and 8.3 N/mm, respectively, akin to that of UHMWPE-PK-RFL fiber cord/rubber composites.

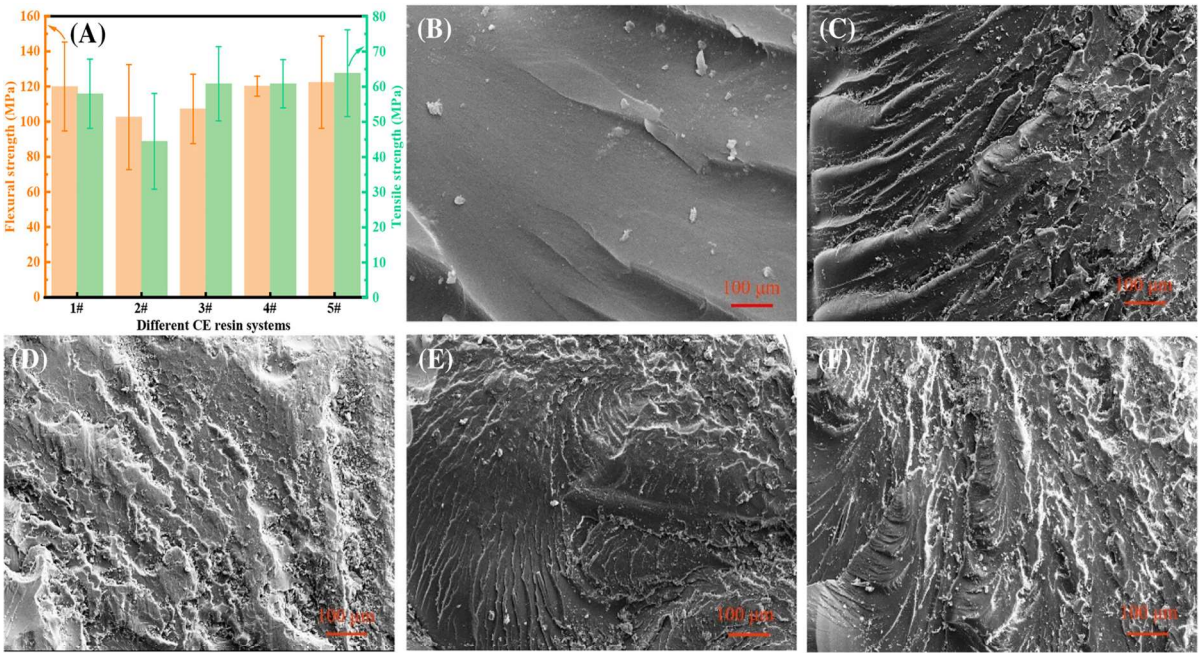

Figure 11. CE resin with polysulfide cation catalyst and its UHMWPE composites. **(A)** Flexural and tensile strength of different CE resin systems. Fractured surface morphology of flexural strength samples: **(B)** uncatalytic CE resin, **(C)** 121 ℃-CE-PSC, **(D)** 130 ℃-CE-PSC, **(E)** 135 ℃-CE-PSC, and **(F)**140 ℃-CE-PSC. Reprinted with permission from reference [78], copyright John Wiley and Sons 2024.

Notably, inorganic compound materials can also be incorporated into the polymeric matrix, facilitating synergistic properties enhancement for UHMWPE fiber-reinforced composites. For instance, Wang et al. [82] deployed wrapping to amplify armor material impact resistance. They infiltrated polyurethane (PU) into UHMWPE threads, interwoven it with ZrO_2 for added tenacity, and evaluated the outcomes using several microscopic methodologies inclusive of three-dimensional X-ray computed tomography, optical microscopy, and SEM. Observations indicated that PU coated composite threads exhibited strain-rate sensitivity reaching 4.4×10^{-2} s^{-1}; beyond this limit, strain rate ceases to affect their peak force. Furthermore, ZrO_2 integration substantially enhanced peak forces, potentially owing to fiber cohesion reinforcement. Additionally, PU insertion noticeably amplified UHMWPE thread peak tensile forces, escalating rates by 47.2% (95% CI, 28.4%–66.0%) for PU/PE threads and 44.0% (95% CI, 29.0%–58.9%) for ZrO_2/PU/PE threads across varying strain rates, likely due to improved fiber connectivity. Henceforth, these composite threads hold the promise to refine impact energy dissipation, thereby bolstering large-scale armor structure impact resistance. In order to surmount the impediment for materials in domains such as extraterrestrial exploration with versatility, low mass, high strength, and superior neutron shielding capabilities, novel organic-inorganic composites have been innovated by Xu et al. [83] This research employed the self-reinforcement technique of UHMWPE fibers within a linear low-density polyethylene (LLDPE) matrix, coupled with a hierarchical scattering and absorption methodology. A flexible, lightweight multi-layer construct was engineered through alternate layers of gadolinium oxide (Gd_2O_3)/LLDPE and UHMWPE fiber stacks fabricated using hot-pressing techniques to bolster the composites mechanical resilience and neutron shielding efficacy. Consequently, a

shielding efficiency of approximately 90.0% can be attained with just 2 mm thickness of the composites (comprising 20 wt% Gd_2O_3), while an equivalent Gd areal density (EGdAD) value of 0.0489 g/cm^3 suffices to attain 99% shielding proficiency. Additionally, the composites exhibited substantial enhancements in tensile strength and modulus, averaging 1000% (from 15.86 MPa to 179.95 MPa) and 1238% (from 230.53 MPa to 2787.55 MPa) boost over the Gd_2O_3/LLDPE counterparts, respectively. The overall performance of multilayer Gd_2O_3/UHMWPE/LLDPE composites exceed previous literature reports, thus presenting immense potential for applications in diverse sectors such as aerospace. Besides, Gangwani et al. [84] assessed the tribological efficacy of graphite, hexagonal boron nitride (hBN), and short carbon fibers (CFs), utilized as micro-nano fillers in a hybrid UHMWPE composite under boundary lubrication. The filler combinations tested were subjected to contact pressures ranging from 5 to 15 MPa using distilled water. The study identified synergistic effects among fillers, with optimal performance achieved by incorporating all scale fillers. The most efficient composite, comprising short CFs, micrographite, micro-hBN, and nano-hBN, exhibited a 75% friction reduction, a friction coefficient of 0.06, and a specific wear rate reduction of two orders of magnitude to 2×10^{-7} mm^3/Nm, compared to the original UHMWPE. Notably, strategic incorporation of BN resulted in a reduced wear rate, with nano-BN composites displaying 40% lower friction than those containing solely micro-scale fillers. Consequently, it deterred the extraction of short carbon fibers, transitioning the dominant wear mechanism from abrasive to adhesive in nature.

6. Prospect

UHMWPE fibers have great application potential and significant practical implications in the field of contemporary engineered materials. Nevertheless, due to its shortcomings, including inadequate heat resistance, poor interfacial performance, it continues to encounter the obstacle of propagation and implementation. Therefore, it is imperative to strengthen the research and development of UHMWPE fibers, reduce production costs, and promote their application in an expanded range of fields.

Firstly, the manufacturing process of UHMWPE fiber materials requires continuous enhancement, mainly focusing on reducing energy consumption, augmenting solvent recuperation, streamlining processes, or employing intelligent technology to assist in the spinning process and fiber quality analysis and control, in order to increase the tensile strength and elongation at break of fibers, reduce residual additives, and mitigate the unevenness of deniers. Secondly, by refining the crystal structure, crystallinity, molecular weight distribution (MWD) of raw materials, regulating the entanglement degree of raw material chains, and incorporating nanomaterials, more opportunities can be provided for its application in the field of engineered materials. Moreover, in terms of functional modification of UHMWPE fiber materials, surface treatment, composite material formulation, and nanofiller reinforcement are employed to enhance the strength of composite materials, UV resistance, wear resistance, and anti-static properties, enriching the

preparation of differentiated fibers and broadening their application scope in the field of functional materials. Specifically, the introduction of novel chemical conversion technologies aids in amplifying the potential application of UHMWPE in the recycling and utilization of long-chain polyethylene. Reflecting on the future, with the relentless progress of technology and the intensification of environmental mandates, the modification and application methodology of UHMWPE will persistently evolve, establishing it as a more indispensable role in the field of high-performance materials.

7. Conclusions

The relentless advancement of society has led to an escalating use of engineered materials across diverse domains, particularly in aerospace, national security, and renewable energy. The demand for advanced materials with unique properties is progressively increasing. Among them, UHMWPE fibers have emerged as a notable high-performance fiber, primarily attributed to their exceptional strength, elevated modulus, superior low-temperature resistance, and robust wear resistance. These characteristics render UHMWPE fibers suitable for a variety of applications, thereby presenting substantial market opportunities. In this review, we provide a comprehensive analysis of the performance characteristics of UHMWPE fibers, along with an in-depth discussion of their fundamental fabrication techniques and recent research advances. We believe that these efforts will catalyze progressive and enduring advancement in this area. Furthermore, within the realm of UHMWPE fibers, more pioneering material processing procedures, theoretical advancements, and augmented industrial applications will manifest, in order to optimize the performance and potential of this material.

Conflict of interest: The authors declare no conflict of interest.

References

1. Baye B, Tesfaye T. The new generation fibers: a review of high performance and specialty fibers. Polymer Bulletin. 2022, 79(11): 9221-9235. doi: 10.1007/s00289-021-03966-6
2. Shelly D, Lee S-Y, Park S-J. Compatibilization of ultra-high molecular weight polyethylene (UHMWPE) fibers and their composites for superior mechanical performance: A concise review. Composites Part B: Engineering. 2024, 275: 111294. doi: 10.1016/j.compositesb.2024.111294
3. Liu Z, Yin X, Zhang H, et al. Efficient self-reinforcement technology and mechanism for ultra-high molecular weight polyethylene based on powder solid-state extension. Polymer. 2024, 290: 126498. doi: 10.1016/j.polymer.2023.126498
4. Siskey R, Smelt H, Boon-Ceelen K, et al. 22 - UHMWPE Homocomposites and Fibers. In UHMWPE Biomaterials Handbook (Third Edition), Kurtz, S. M., Ed. William Andrew Publishing: Oxford, 2016; pp 398-411.
5. Sobieraj MC, Rimnac CM. Ultra high molecular weight polyethylene: Mechanics, morphology, and clinical behavior. Journal of the Mechanical Behavior of Biomedical Materials. 2009, 2(5): 433-443. doi: 10.1016/j.jmbbm.2008.12.006
6. Houben SJA, Verpaalen RCP, Engels TAP. Processing and Properties of Melt Processable UHMW-PE Based Fibers Using Low Molecular Weight Linear Polyethylene's. 2020, 305(10): 2000360. doi: 10.1002/mame.202000360
7. Wang J, Hu X, Liu F, et al. Gel-spinning of ultra-high molecular weight polyethylene by a twin-screw extruder with an ultra-large length-to-diameter ratio. 2022, 62(11): 3773-3785. doi: 10.1002/pen.26143
8. Li C, Wang G, Jia J, et al. The mechanical properties of UHMWPE fiber-knitted composites. Journal of Engineered Fibers and Fabrics. 2018, 13(2): 7-14. doi: 10.1177/155892501801300202

9. Zhu Y, Song Y, Wu W, et al. Ballistic performance and energy transfer of ultrahigh molecular weight polyethylene laminate. Materials Letters. 2024, 367: 136540. doi: 10.1016/j.matlet.2024.136540
10. Zhang R, Song X-T, Qiang L-S, et al. Ballistic performance of UHMWPE fiber laminates with pre-formed holes. Thin-Walled Structures. 2024, 201: 112011. doi: 10.1016/j.tws.2024.112011
11. Hussain M, Naqvi RA, Abbas N, et al. Ultra-High-Molecular-Weight-Polyethylene (UHMWPE) as a Promising Polymer Material for Biomedical Applications: A Concise Review. 2020, 12(2): 323. doi: 10.3390/polym12020323
12. Pan L, Wang Y, Wang C, et al. UHMWPE fibers reinforced gradient structure to break the thermal-dielectric-mechanical trade-off in high filled polyethylene. Composites Science and Technology. 2024, 246: 110375. doi: 10.1016/j.compscitech.2023.110375
13. Ren L, Guo H, Kang L, et al. Lightweight, electrical insulating, and high thermally conductive all-polymer composites with reinforced interfaces. Composites Science and Technology. 2023, 240: 110080. doi: 10.1016/j.compscitech.2023.110080
14. Ruan F, Bao L. Mechanical enhancement of UHMWPE fibers by coating with carbon nanoparticles. Fibers and Polymers. 2014, 15(4): 723-728. doi: 10.1007/s12221-014-0723-9
15. Yu Q, Gao J, Wang Z, et al. Excellent interfacial bonding in UHMWPE fiber/ epoxy resin composites fabricated via a swelling approach. Journal of Polymer Research. 2023, 30(7): 275. doi: 10.1007/s10965-023-03597-7
16. Pilato LA, Michno MJ. High Performance Fibers. In Advanced Composite Materials, Springer Berlin Heidelberg: Berlin, Heidelberg, 1994; pp 75-96.
17. Wang Z, Sangroniz L, Xu J, et al. Polymer Physics behind the Gel-Spinning of UHMWPE Fibers. 2024, 45(15): 2400124. doi: 10.1002/marc.202400124
18. Forster AL, Forster AM, Chin JW, et al. Long-term stability of UHMWPE fibers. Polymer Degradation and Stability. 2015, 114: 45-51. doi: 10.1016/j.polymdegradstab.2015.01.028
19. Li C, Shan J, Cui Y, et al. Anti-ultraviolet Properties of Weft-Knitted Textile Composite Materials Based on Modified Aramid and UHMWPE Fabrics. Fibers and Polymers. 2024, 25(2): 631-649. doi: 10.1007/s12221-023-00396-1
20. Sun H, Kong H, Ding H, et al. Improving UV Resistance of Aramid Fibers by Simultaneously Synthesizing TiO2 on Their Surfaces and in the Interfaces Between Fibrils/Microfibrils Using Supercritical Carbon Dioxide. 2020, 12(1): 147. doi: 10.3390/polym12010147
21. Li M, Cheng K, Wang C, et al. Functionalize Aramid Fibers with Polydopamine to Possess UV Resistance. Journal of Inorganic and Organometallic Polymers and Materials. 2021, 31(7): 2791-2805. doi: 10.1007/s10904-021-01910-9
22. Li H, Zong S, Xiong X. The influence of penetration angle on anti-penetration performance and reverse penetration ricochet phenomenon of UHMWPE laminates. International Journal of Impact Engineering. 2023, 182: 104780. doi: 10.1016/j.ijimpeng.2023.104780
23. Wang H, Weerasinghe D, Hazell PJ, et al. Ballistic impact response of flexible and rigid UHMWPE textile composites: Experiments and simulations. Defence Technology. 2023, 22: 37-53. doi: 10.1016/j.dt.2022.08.009
24. Cui W, Yang S, Zhang X, et al. High Wear Resistance of Ultralow-Wear Polyethylene with Different Molecular Weights Under Different Contact Pressure. Tribology Letters. 2022, 70(2): 51. doi: 10.1007/s11249-022-01595-2
25. Mohammed AS, Fareed MI. Improving the friction and wear of poly-ether-etherketone (PEEK) by using thin nano-composite coatings. Wear. 2016, 364-365: 154-162. doi: 10.1016/j.wear.2016.07.012
26. Minn M, Sinha SK. DLC and UHMWPE as hard/soft composite film on Si for improved tribological performance. Surface and Coatings Technology. 2008, 202(15): 3698-3708. doi: 10.1016/j.surfcoat.2008.01.012
27. Panin SV, Kornienko LA, Alexenko VO, et al. Increasing Wear Resistance of UHMWPE by Loading Enforcing Carbon Fibers: Effect of Irreversible and Elastic Deformation, Friction Heating, and Filler Size. 2020, 13(2): 338. doi: 10.3390/ma13020338
28. Liu H, Ji H, Wang X. Tribological properties of ultra-high molecular weight polyethylene at ultra-low temperature. Cryogenics. 2013, 58: 1-4. doi: 10.1016/j.cryogenics.2013.05.001
29. Han L, Cai H, Chen X, et al. Study of UHMWPE Fiber Surface Modification and the Properties of UHMWPE/Epoxy Composite. 2020, 12(3): 521. doi: 10.3390/polym12030521
30. Yu J, Chen S, Huang H, et al. A universal strategy for rapid and scalable surface modification of ultra high molecular weight polyethylene fiber. Composite Structures. 2024, 334: 117935. doi: 10.1016/j.compstruct.2024.117935

31. Joshi A, Mishra A, Saxena VK. Impact response and energy absorption mechanisms of UHMWPE fabric and composites in ballistic applications: A comprehensive review. Composites Part A: Applied Science and Manufacturing. 2024, 185: 108314. doi: 10.1016/j.compositesa.2024.108314
32. Fallahi H, Kaynan O, Asadi A. Insights into the effect of fiber–matrix interphase physiochemical- mechanical properties on delamination resistance and fracture toughness of hybrid composites. Composites Part A: Applied Science and Manufacturing. 2023, 166: 107390. doi: 10.1016/j.compositesa.2022.107390
33. Huang S, Fu Q, Yan L, et al. Characterization of interfacial properties between fibre and polymer matrix in composite materials – A critical review. Journal of Materials Research and Technology. 2021, 13: 1441-1484. doi: 10.1016/j.jmrt.2021.05.076
34. Fang C, Zhao Y, Chen Z, et al. Influence of oxygen/argon duoplasmatron synergistic modification on the mechanical properties of UHMWPE/vinyl ester composites. 2023, 44(10): 6811-6825. doi: 10.1002/pc.27599
35. Zhao Y, Fang C, Jia L, et al. Influence of Oxygen/Argon/Nitrogen multi-component plasma modification on interlayer toughening of UHMWPE fiber reinforced composites. Composite Structures. 2024, 339: 118142. doi: 10.1016/j.compstruct.2024.118142
36. Meng L, Li W, Ma R, et al. Long UHMWPE fibers reinforced rigid polyurethane composites: An investigation in mechanical properties. European Polymer Journal. 2018, 105: 55-60. doi: 10.1016/j.eurpolymj.2018.05.021
37. Wang H, Xu L, Hu J, et al. Radiation-induced oxidation of ultra-high molecular weight polyethylene (UHMWPE) powder by gamma rays and electron beams: A clear dependence of dose rate. Radiation Physics and Chemistry. 2015, 115: 88-96. doi: 10.1016/j.radphyschem.2015.06.012
38. Enomoto I, Katsumura Y, Kudo H, et al. Graft polymerization using radiation-induced peroxides and application to textile dyeing. Radiation Physics and Chemistry. 2011, 80(2): 169-174. doi: 10.1016/j.radphyschem.2010.07.028
39. Wu M, Jia L, Chen Z, et al. Synergetic enhancement of interfacial properties and impact resistant of UHMWPE fiber reinforced composites by oxygen plasma modification. Composite Structures. 2022, 292: 115663. doi: 10.1016/j.compstruct.2022.115663
40. Yang X, Zhang Z, Xiang Y, et al., Superior Enhancement of the UHMWPE Fiber/Epoxy Interface through the Combination of Plasma Treatment and Polypyrrole In-Situ Grown Fibers. In Polymers, 2023; Vol. 15.
41. Wang S, Ma J, Feng X, et al. An effective surface modification of UHMWPE fiber for improving the interfacial adhesion of epoxy resin composites. Polymer Composites. 2020, 41(4): 1614-1623. doi: 10.1002/pc.25483
42. Wang K, Shen L, Lu R, et al. Remarkably improved interfacial adhesion of UHMWPE fibers reinforced composite by constructing a three-dimensional stacked nanoparticles structure at interphase. Journal of Industrial and Engineering Chemistry. 2022, 110: 552-563. doi: 10.1016/j.jiec.2022.03.031
43. Liu H, Li W, Zhou Y, et al. Effects of Donut-Shaped ZnO Decorated UHMWPE Fibers on the Mechanical Properties of Rigid Polyurethane-Based Composites. ACS Applied Polymer Materials. 2022, 4(8): 5422-5430. doi: 10.1021/acsapm.2c00511
44. Liu H, Yu X, Ji M, et al. High through-plane thermal conductivity and light-weight of UHMWPE fibers/PDMS composites by a large-scale preparation method. Polymer. 2021, 229: 123975. doi: 10.1016/j.polymer.2021.123975
45. Yan Y. 2 - Developments in fibers for technical nonwovens. In Advances in Technical Nonwovens, Kellie, G., Ed. Woodhead Publishing: 2016; pp 19-96.
46. Xu R, Zhou C, Sun X, et al. Fabricating UHMWPE-based shielding materials with excellent high-temperature mechanical properties and irradiation endurance properties via controlling crosslinked and crystalline structures. 2024, 35(1): e6204. doi: 10.1002/pat.6204
47. Dong T, Niu F, Qiang Z, et al. Thermal aging behavior and heat resistance mechanism of ultraviolet crosslinked ultra-high molecular weight polyethylene fiber. Journal of Applied Polymer Science. 2024, 141(28): e55648. doi: 10.1002/app.55648
48. Yu D, Liu S, Xin Y. Air Plasma-Nano ZnO Coating Improves the Impact Resistance of Ultra-High Molecular Weight Polyethylene Fiber. Composite Interfaces. 2023, 30(11): 1247-1267. doi: 10.1080/09276440.2023.2209370
49. Wang H, Xu L, Li R, et al. Improving the creep resistance and tensile property of UHMWPE sheet by radiation cross-linking and annealing. Radiation Physics and Chemistry. 2016, 125: 41-49. doi: 10.1016/j.radphyschem.2016.03.009
50. Liu X, Zhang S, Xu X, et al. Study on the creep and recovery behaviors of UHMWPE/CNTs composite fiber. Fibers and Polymers. 2013, 14(10): 1635-1640. doi: 10.1007/s12221-013-1635-9

51. Chhetri S, Bougherara H. A comprehensive review on surface modification of UHMWPE fiber and interfacial properties. Composites Part A: Applied Science and Manufacturing. 2021, 140: 106146. doi: 10.1016/j.compositesa.2020.106146
52. Yuan H, Long C, Yu J, et al. Synthesis of Granular Hydroxy-Functionalized Ultra-high-molecular-weight Polyethylene and Its Fiber Properties. Advanced Fiber Materials. 2022, 4(4): 786-794. doi: 10.1007/s42765-022-00136-9
53. Li Zhiyao WX, YANG Chenguang, WANG Dong. Study on Preparation and Creep Resistance of UHMWPE Fiber with Crosslinked Structure on the Surface. 2023, 37(21): 22040008-22040006. doi: 10.11896/cldb.22040008
54. Dong T, Niu F, Qiang Z, et al. Structure and properties evolution of UV crosslinked ultra-high molecular weight polyethylene fiber during processing. Journal of Polymer Science. 2024, 62(11): 2385-2398. doi: 10.1002/pol.20230919
55. Wen X, Li Z, Yang C, et al. Electron beam irradiation assisted preparation of UHMWPE fiber with 3D cross-linked structure and outstanding creep resistance. Radiation Physics and Chemistry. 2022, 199: 110370. doi: 10.1016/j.radphyschem.2022.110370
56. Kuo CJ, Lan WL. 5 - Gel spinning of synthetic polymer fibres. In Advances in Filament Yarn Spinning of Textiles and Polymers, Zhang, D., Ed. Woodhead Publishing: 2014; pp 100-112.
57. Da Silva Chagas NP, Lopes Da Silva Fraga G, Marques MdFV. Fibers of Ultra-High Molecular Weight Polyethylene Obtained by Gel Spinning with Polyalphaolefin Oil. Macromolecular Research. 2020, 28(12): 1082-1090. doi: 10.1007/s13233-020-8147-4
58. Sun Y, Duan Y, Chen X, et al. Research on the molecular entanglement and disentanglement in the dry spinning process of UHMWPE/decalin solution. Journal of Applied Polymer Science. 2006, 102(1): 864-875. doi: 10.1002/app.23672
59. Ding J, Chen G, Huang W, et al. Tensile Strength Statistics and Fracture Mechanism of Ultrahigh Molecular Weight Polyethylene Fibers: On the Weibull Distribution. ACS Omega. 2024, 9(11): 12984-12991. doi: 10.1021/acsomega.3c09230
60. Wang H, Yan X, Tang X, et al. Contribution of the Initially Entangled State and Particle Size to the Sintering Kinetics of UHMWPE. Macromolecules. 2022, 55(4): 1310-1320. doi: 10.1021/acs.macromol.1c02058
61. Tam T, Bhatnagar A. 1 - High-performance ballistic fibers and tapes. In Lightweight Ballistic Composites (Second Edition), Bhatnagar, A., Ed. Woodhead Publishing: 2016; pp 1-39.
62. Van Der Werff H, Heisserer U. 3 - High-performance ballistic fibers: Ultra-high molecular weight polyethylene (UHMWPE). In Advanced Fibrous Composite Materials for Ballistic Protection, Chen, X., Ed. Woodhead Publishing: 2016; pp 71-107.
63. Wang Z, An M, Xu H, et al. Structural evolution from shish-kebab to fibrillar crystals during hot-stretching process of gel spinning ultra-high molecular weight polyethylene fibers obtained from low concentration solution. Polymer. 2017, 120: 244-254. doi: 10.1016/j.polymer.2017.05.062
64. Zhao GL. Progress in Manufacturing and Application of UHMWPE Fiber. Journal of Beijing Institute of Clothing Technology (Natural Science Edition). 2019, 39(2): 95-102. doi: 10.16454/j.cnki.issn.1001-0564.2019.02.014
65. Wang X, Zheng H, Sun Y. Study on structures and properties of ultra-hot drawing UHMWPE fibers fabricated via dry spinning method. Journal of Polymer Engineering. 2018, 38(9): 863-870. doi: 10.1515/polyeng-2017-0400
66. Brown KR, Love-Baker C, Xue Z, et al. Ultra-high molecular weight polyethylene micro-ribbon fibers gel spun using orange terpenes. Polymer Engineering & Science. 2024, 64(4): 1743-1755. doi: 10.1002/pen.26656
67. Li Y, Min L, Xin JH, et al. High-performance fibrous artificial muscle based on reversible shape memory UHMWPE. Journal of Materials Research and Technology. 2022, 20: 7-17. doi: 10.1016/j.jmrt.2022.07.045
68. Fukushima Y, Murase H, Ohta Y. Dyneema®: Super Fiber Produced by the Gel Spinning of a Flexible Polymer. In High-Performance and Specialty Fibers: Concepts, Technology and Modern Applications of Man-Made Fibers for the Future, The Society of Fiber, S., Techno, J., Eds. Springer Japan: Tokyo, 2016; pp 109-132.
69. On SY, Park S, Kim SS. Preparation and Characterization of Hybrid Structured MWCNT/UHMWPE Fiber Sensors for Strain Sensing and Load Bearing of Composite Structures. 2019, 4(12): 1900807. doi: 10.1002/admt.201900807
70. Da Silva Chagas NP, De Fátima Vieira Marques M. Effect of polyalphaolefin oils as a solvent in gel-spinning of ultra-high molecular weight polyethylene fibers. 2021, 138(46): 51372. doi: 10.1002/app.51372
71. Cao T, Ren L, Meng L, et al. Structural Evolution of UHMWPE Fibers during Poststretching with Distinct Initial Structures. Journal of Wuhan University of Technology-Mater. Sci. Ed. 2023, 38(2): 280-285. doi: 10.1007/s11595-023-2694-4
72. Wang Y, Fu J, Yu J, et al. Dissolving of Ultra-high Molecular Weight Polyethylene Assisted Through Supercritical Carbon Dioxide to Enhance the Mechanical Properties of Fibers. Advanced Fiber Materials. 2022, 4(2): 280-292. doi: 10.1007/s42765-021-00107-6

73. Wang Y, Fu J, Song Q, et al. Regulating the dissolving system of ultra-high molecular weight polyethylene to enhance the high-strength and high-modulus properties of resultant fibers. 2022, 139(29): e52653. doi: 10.1002/app.52653
74. Yu L, Bao J, Wang G, et al. Structure and properties of gel-spun ultra-high molecular weight polyethylene fibers obtained from industrial production line. Journal of Applied Polymer Science. 2021, 138(44): 51317. doi: 10.1002/app.51317
75. Yang C, Tao D, Wang F, et al. Ultrahigh-Molecular-Weight Polyethylene Fibers with Excellent Creep Resistance Derived from an Online-Tailored Fish-Skeleton-like Molecular Structure. Macromolecules. 2024, 57(14): 6848-6859. doi: 10.1021/acs.macromol.4c00641
76. Wang H, Liu R, Yu J, et al. Effect of Gel-spun Solution Concentration on the Structure and Properties of UHMWPE Monofilaments with Coarse Denier. Fibers and Polymers. 2022, 23(7): 1807-1816. doi: 10.1007/s12221-022-3227-z
77. Yang X, Zhang Z, Lin Y, et al. Low-velocity impact responses of UHMWPE fiber/epoxy laminates with plasma treatment and polypyrrole grafting. Materials Letters. 2024, 362: 136199. doi: 10.1016/j.matlet.2024.136199
78. Jiang J, Geng H, Xu K, et al. Catalytic cyanate resin with polysulfide cation catalyst and its ultra-high molecular weight polyethylene fiber composites for radome. Polymer Composites. 2024, 45(12): 11241-11251. doi: 10.1002/pc.28562
79. Xiang Y, Zhang Z, Jiang Y, et al. Effect of impact spacing on the dynamic response of UHMWPE fiber composites under two-point high velocity impacts. Thin-Walled Structures. 2024, 200: 111969. doi: 10.1016/j.tws.2024.111969
80. Qiao Y, Ko S, Ramos JL, et al. Effects of processing temperature, pressure, and fiber volume fraction on mechanical and morphological behaviors of fully-recyclable uni-directional thermoplastic polymer-fiber-reinforced polymers. Composites Part C: Open Access. 2024, 14: 100497. doi: 10.1016/j.jcomc.2024.100497
81. Liu R, Yan Z, Ruan C, et al. Surface modification of ultra-high molecular weight polyethylene fibers by an eco-friendly impregnation solution to enhance interfacial adhesion with rubber. Materials & Design. 2024, 238: 112707. doi: 10.1016/j.matdes.2024.112707
82. Wang H, Shen Y, Wei J, et al. Dynamic strengthening of UHMWPE yarns by incorporating ZrO2/PU coatings. Composites Science and Technology. 2024, 255: 110730. doi: 10.1016/j.compscitech.2024.110730
83. Liu H, Zhang H, Yu X, et al. Flexible, lightweight, high strength and high efficiently hierarchical Gd2O3/PE composites based on the UHMWPE fibers with self-reinforcing strategy for thermal neutron shielding. Composites Science and Technology. 2024, 251: 110549. doi: 10.1016/j.compscitech.2024.110549
84. Gangwani P, Kovač J, Emami N, et al. Effect of multi-scale fillers on the tribological behavior of UHMWPE composites in water-lubricated contacts. Tribology International. 2024, 196: 109669. doi: 10.1016/j.triboint.2024.109669

Materials Technology Reports 2024, 2(2), 2136.
https://doi.org/10.5940mtr2136

Review

Thermoelectric materials—Challenges, approaches and classes

N. Karthikeyan[1,*], C. Prabhakaran[1], R. Akilan[2]

[1] Department of Physics, Anna University, Chennai 600025, India
[2] Faculty of Science, Aksheyaa College of Arts and Science, Madhuranthagam 603314, India
*** Corresponding author:** N. Karthikeyan, karthin10@gmail.com

CITATION

Karthikeyan N, Prabhakaran C, Akilan R. Thermoelectric materials—Challenges, approaches and classes. Materials Technology Reports. 2024; 2(2): 2136. https://doi.org/10.59400/mtr2136

ARTICLE INFO

Received: 16 November 2024
Accepted: 18 December 2024
Available online: 24 December 2024

Abstract: Thermoelectric (TE) materials have gained significant attention in recent days for their ability to convert waste heat energy into electrical energy. Numerous advances in new and a unique thermoelectric materials have been developed during the last decades due to their ease of device fabrication technique and technology. Thermoelectric research has become a hotspot in materials science over the recent years due to its promising global necessity in energy generation, energy conservation and subsequent utilization. Here this article seeks to highlight some of the recent advances in thermoelectric research such as criteria for ideal TE materials, various strategies that are in practice to improve TE performance and different methodologies adopted in the preparation of TE-based materials. This article also highlights some of the explored state-of-art materials in thermoelectric research to layout a grid for future purposes.

Keywords: thermoelectrics; figure of merit; power factor; waste heat; electricity

1. Introduction

The energy crisis was a universal concern due to many factors including the global campaign to reduce the emission of carbon and other related effects. In the early 2000s, the demand for fossil fuels contributed to show the renewed interest in the negative effects on climate change and it focused on reducing the emission of carbon [1]. Since much attention is gained on renewable energy i.e. it is derived from the sources that can be refilled, restored or reused [2]. One of the major advantages of renewable energy is that it does not release any harmful pollutants into the environment. The investment in renewable energy in our global market is considerably increased in our daily lives and the dropping investment in fossil fuels energy led to an energy shortage, which could not be filled by the emerging energy sources [3,4]. The major key factor influencing the growth of global energy demand is due to economic growth, urbanization, and industrialization. Solar and waste heat energy is the most attractive, abundant, renewable, clean and green energy sources.

Due to the rapid economic expansion and world's fastest-growing energy markets, severe energy demand was to be expected across the world, including in developing countries by 2035. It is projected that global energy demand will increase approximately by 128% in 2035, with an average annual growth rate of nearly 5%. Currently, about 65% of world's electricity is generated from thermal power plants utilizing fossil fuels such as coal, natural gas and petroleum. Nuclear sources contribute 20% of the electricity generation, while renewable sources account for 15%. It's worth noting that up to 50% of input energy is wasted as heat during the energy production process [5]. Thus, the major drawback associated with the above energy production sources are its environmental pollution and greenhouse gas emission. Hence, the future growth depends on the long-term and steady sources that are

affordable, easily accessible, and environment-friendly. Also, there is a huge need in developing technologies that can utilize the wasted heat energy and convert it into an electrical energy [6]. **Figure 1** shows the schematic view that generates electrical energy from various sources. By making advancements in these areas, researchers aim to overcome the existing limitations by the usage of TE devices and unlock their full potential for practical applications in power generation, waste heat recovery, and refrigeration. These efforts are crucial for realizing the promise of thermoelectricity as a clean and sustainable energy technology.

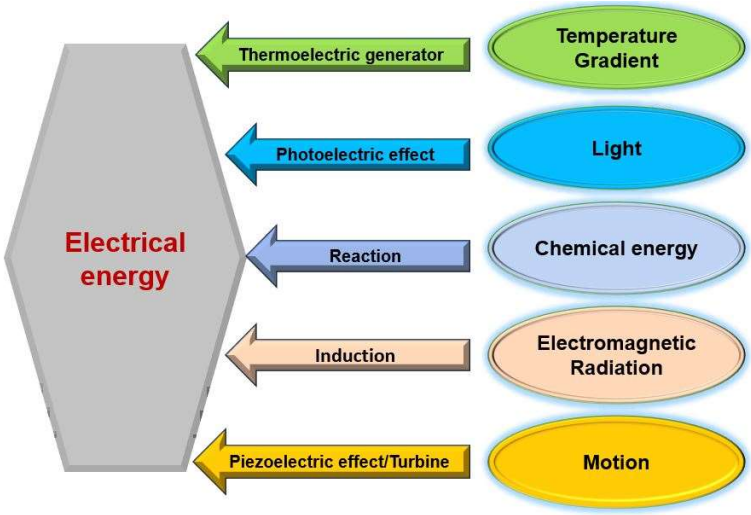

Figure 1. Schematic view of various sources that generates electrical energy.

2. Importance of thermoelectrics

The field of thermoelectric technology faces its limitations in widespread of application due to several factors such as low energy conversion efficiency, higher cost, and limited usage at higher temperature. Modern research efforts are primarily focused on addressing these limitations by improving the efficiency and power output of thermoelectric devices. A key parameter in this pursuit is the figure of merit (ZT), which quantifies the efficiency of thermoelectric materials [7]. The performance of TE materials can be analysed using figure of merit which can be calculated as $ZT = (S^2\sigma/\kappa)\,T$, where S denotes the factor Seebeck coefficient, σ is electrical conductivity, T is an absolute temperature and κ is thermal conductivity. Researchers continually strive to enhance ZT values to maximize energy conversion efficiency. **Figure 2** illustrates the different steps involved in achieving the high ZT value. The barrier of the current TE materials is a low ZT, to be competitive with the today's power systems, TE devices must have a high ZT of 4. A secondary limitation of present technology is their unstability and poor performance at higher temperatures particularly their mechanical stability at elevated temperature is very low, the above are the main constraints to be taken into account while developing the materials for TE device [8]. Currently Bi_2Te_3 PbTe, CdO, Bi_2e_3 Sb_2Te_3 have appreciable ZT values and used in present commercial TE devices which are rare, toxicity, high cost, too hazardous to human health and environment. The present TE materials are too brittle which reduces the strength, hardness, and toughness during utilization, which might have to be

considered for commercial viability. A material used in thermoelectric applications must possess a high stiffness (i.e. Young's modulus) to prevent defects during manufacturing, moderate hardness to resist surface damage during handling and significant thermal toughness to withstand thermal cycling without failure [9]. Improving materials with such mechanical properties by maintaining high ZT values possess a significant challenge due to the inverse relationships between mechanical, electrical and thermal behaviour. Enhancing one aspect often comes at the expense of others, complicating the search for an ideal thermoelectric material. Nevertheless, ongoing research and development efforts aim to overcome these challenges by exploring a new material, optimizing doping levels and employing advanced fabrication techniques. The ultimate goal is to identify materials with the highest potential for achieving a high figure of merit while also exhibiting desirable mechanical properties for commercial applications.

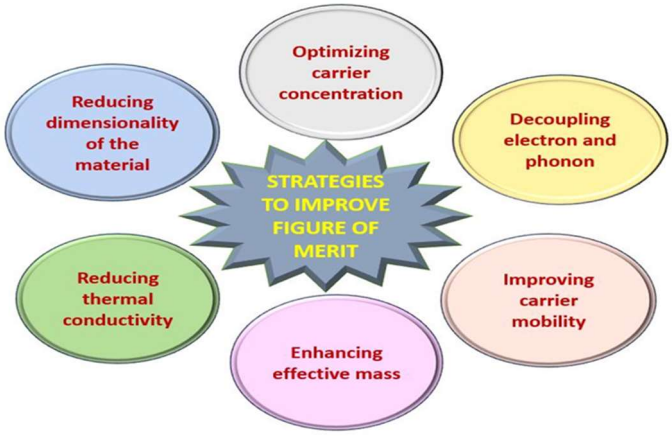

Figure 2. Strategies to improve the figure of merit.

Among vast field, this thermoelectrics presents a major challenge to physicists, as well as to materials scientists. Major challenge here is to develop a stable, efficient, less expensive, and an environment-friendly solid-state material. Further the research on developing new materials requires a combination of theoretical direction, intense chemical intuition, synthetic skill, materials processing, and a good expertise in measurement techniques. The combination on all of these led to a development of new and emerging thermoelectric materials.

3. Criteria for good thermoelectric materials

The good TE materials should have large Seebeck coefficient and electrical conductivity at the same time low thermal conductivity. By rule of thumb, both Seebeck coefficient and electrical conductivity must be high, while thermal conductivity is minimized to obtain the maximum ZT. From the formula it is known, that by reducing the thermal conductivity as shown in **Figure 3**. one can create the more efficient thermoelectric device. The parameter $S^2\sigma$ also known as the power factor (PF), which means by having a large PF the device could output, a large voltage and current. Historically, most of TE materials and devices had ZT values around 2.0, and the energy conversion efficiency was approximately about 25% or less. Achieving

a higher ZT value, ideally around 4 or higher, is considered a significant milestone in thermoelectric research [10]. With such a ZT value, the theoretical maximum energy conversion efficiency between heat and electricity could reach approximately 30%. This level of efficiency would represent a substantial improvement over current thermoelectric technologies and would open up a wide range of practical applications, including waste heat recovery in industrial processes, automotive exhaust systems, and power generation from renewable energy sources. Researchers are actively exploring various strategies to enhance the thermoelectric performance of materials and devices, including novel material synthesis techniques, nano structuring, and advanced characterization methods. By pushing the ZT value closer to the theoretical limit, thermoelectric technology holds the potential to become a more efficient and sustainable solution for energy harvesting and conversion in the future. By Slack, maximum ZT is referred as "Phonon Glass Electron Crystal" (PGEC). The PGEC material features the property as glass-like thermal conductivity by the coexistence of high mobility and charge carriers. However, those properties are interdependent to each other in a bulk material to increase the ZT, and it is hard to adjust one parameter individually [11]. Along with the concept of PGEC, a strategy named as Phonon-Liquid Electron-Crystal (PLEC)was also used to decrease the lattice thermal conductivity by using the liquid-like behaviour of superionic conductors for the transport of phonons. Both PGEC and PLEC strategies represent an innovative way to tailor the thermal and electronic properties of materials. By optimizing a balance between phonon scattering and electron transport mechanism, researchers aim to develop a material with an enhanced thermoelectric efficiency, ultimately enabling more efficient energy conversion in thermoelectric devices.

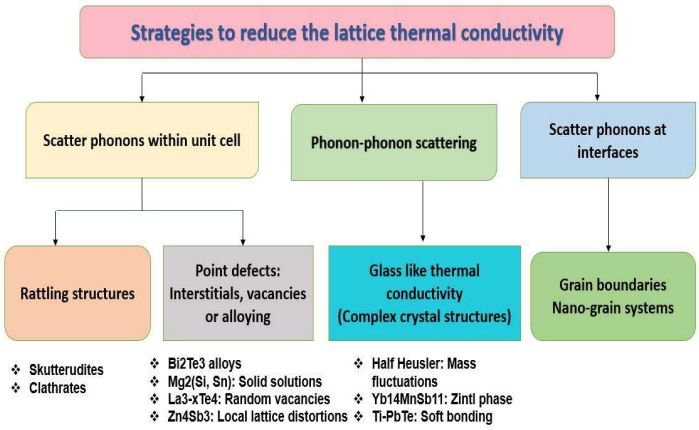

Figure 3. Strategies to achieve low thermal conductivity.

- Low temperature (up to 600 °C): Common application of TE are wearable and medical devices, here the device works near to room temperature and also used in the Microelectronics applications.
- Mid temperature (from 600 °C to 1000 °C): Commonly employed TE materials in this range are used in automotive and industries, where the heat waste is converted into an electricity.

- High temperature (from 1000 °C): Here the TE materials are mainly used in aerospace for energy harvesting, space missions and in exploration of outer space also [12].

4. Art of thermoelectric materials

In the past, many different techniques have been used to develop the thermoelectric materials. An overview about the recent most TE materials and its preparation methods are reported here. Hence, the below guidelines should be taken in to an account for best production and fabrication techniques in practical applications:

1) Employed technique needs to be adopted at low cost for the high crystallinity production and mass distribution.
2) For practical applications, the density of material should be 95% or above to that of theoretical density and the material must be normally stable during entire range of operation.

By the above-mentioned properties, various synthesis techniques have been progressed in the research such as single crystal growth, bulk technologies (Powder synthesis) and few of them are discussed below.

5. Preparation methods

5.1. Processing technologies: Single crystal growth

Currently, lot of studies have been reviewed on a modern technique called temperature gradient growth that enables the ease-fabrication of high-performing TE single crystals. Recently reported P and N-type SnSe shows the ZT values from 0.8–1.2 around 300–600K [13].

5.2. Bulk technologies: Powder synthesis

Bulk materials are fabricated from the route of powder processing technologies; among these few methods such as mechanical alloying, ball milling, magnetron sputtering, arc-melting and other are discussed below [14].

5.2.1. Hydrothermal method

Hydrothermal synthesis is a viable chemical process for material synthesis and it has been increased during the years. This method refers to the heterogeneous reactions for synthesizing inorganic materials in solution of aqueous as the reaction associated with high temperature and high-pressure systems. Hence, this method is associated to class of the liquid phase chemical solution synthesis and has numerous advantages such as quiet operation, simple and easy synthesis process, controlled particle size and morphology, high crystallization & homogeneity, and phase purity can be achieved. Here the **Table 1**. shows the different figure of merit values for different materials at different temperature, which was synthesized using the hydrothermal method.

Table 1. Figure of merit values for various materials prepared by hydrothermal method.

Materials	Methods	Figure of merit (ZT)	Temperature (K)	References
Ag/Cu_2S	Hydrothermal	1.4	773	Yue et al. [15]
Bi_2S_3/GO	Hydrothermal	0.17	300–650	Bai et al. [16]
Bi_2S_3 + 0.5Wt%f-$MWCNT_s$	Hydrothermal	0.33	589	Bai et al. [17]
$Bi_{1.985}Cu_{0.015}S_3$	Hydrothermal and SPS	0.3	573	Liu et al. [18]
$Zn_{0.3}$BTS	Hydrothermal	0.79	600	Yun et al. [19]

5.2.2. Mechanical alloying

Mechanical alloying and milling include two different ways of synthesizing thermoelectric materials. Mechanical alloying means individual elements are directly ground to form alloys while mechanical milling usually refers to grinding crystalline ingots into nanoparticles. The advantage of mechanical alloying and milling is that large quantity of nano powders can be produced through a relative convenient procedure and with a minimal requirement for equipment. Before high energy ball milling was introduced, mechanical alloying and milling was considered as a path to synthesize these TE materials directly and a wide variety of materials were produced, such as Si-Ge, rare-earth sulfides, Bi-Sb-Te, Pb-Te, Fe-Si and skutterudites. In conclusion, mechanical alloying has been developed into a very mature method of making different kinds of thermoelectric nanocomposites and significant improvement of ZT was observed in literature which was shown in the **Table 2**. The advantages of this method include simple procedure, minimal requirement on equipment, large yield, and surfactant-free environment. The disadvantages include energy intensive, time consuming and little morphology control. The oxide-based TE materials are earth abundant, non-toxic, and stable at higher temperature and also in oxidizing atmosphere. These oxide TE have low figure of merit due to their large thermal conductivity and lower mobilities compared to other TE materials like selenides, chalcogenides and pnictides.

Table 2. Figure of merit values for various materials prepared by mechanical alloying.

Materials	Methods	Figure of merit (ZT)	Temperature (K)	References
Bi_2O_2Se	Mechanical alloying	0.45	823	Zhou et al. [20]
$Bi_XSb_{2-x}Te_3$	Mechanical alloying	1.01–1.13	355	Ioannou et al. [21]
$Mg_2Si_{0.57}Sn_{0.4}Bi_{0.03}$ $Mg_2Si_{0.53}Sn_{0.4}Ge_{0.05}Bi_{0.02}$	Mechanical alloying	1.07 1.2	750	Symeou et al. [22]

5.2.3. Arc melting

Arc melting is one of the most primary and modern method which is used for melting metals to form an alloy. Here an arc is struck between the electrode, most commonly a tungsten is used and here the sample are placed over water-cooled copper hearth. Then electric arc generates a large amount of heat towards the sample, which melts the metal together in order to form an ingot. Evacuation chamber is mostly filled with an argon gas to prevent unwanted oxidation and reaction of the sample with the outer atmosphere. Then repeated melting of the sample is done to improve the homogeneity of alloy, but the small localized region in a melted sample is common.

And the different figure of merit for various materials prepared using an arc melting method was shown in **Table 3**.

Table 3. Figure of merit values for various materials prepared by arc melting.

Materials	Methods	Figure of merit (ZT)	Temperature(K)	References
$Ni_{0.07}Co_{0.93}Sb_3$	Arc melting	≈ 0.041	640	Bhardwaj et al. [23]
$TiNiFe_{0.03}Sn$	Arc melting/Melt spinning/SPS Method	0.54	900	He et al. [24]
$Ba_8Ga_xSi_{46-X}$	Arc melting and SPS	0.55	873	Anno et al. [25]
$Nb_{0.8}Ti_{0.2}Fe_{1.02}Sb$	Arc melting	0.73	390	Kihoi et al. [26]
Ru_2TiGe	Arc melting	0.025	1000	Mondal et al. [27]
P type-Ru_2TiSi &N type-$Ru_2Ti_{0.80}Ta_{0.20}Si$	Arc melting	0.42	900	Fujimoto et al. [28]

5.2.4. Solid state reaction

Solid-state reaction is a decomposition of chemical reaction, where a reactant of solid is heated to form a composition of new solid material. This method is usually employed for the oxide preparation from the source of simple oxides, carbonates, nitrates, hydroxides, oxalates, alkoxides, and other metal salts. Normally, the procedure used in this reaction is employed with multiple steps of annealing and intermediate milling to increase the phase homogeneity, and to decrease particle size. Extra milling makes the powder more compact and to be active. This solid-state is one of the reactions which is most inexpensive routes and requires a simple apparatus. In this method a large volume of powder can be prepared by a simple and easy manner. Compared to other wet preparation routes, this solid-state reaction shows a higher agglomeration, large particle size as well as relative homogeneity. Here in the **Table 4** maximum figure of merit is 1.3 which was achieved at 680K in solid state reaction is reported by our research group [28].

Table 4. Figure of merit values for various materials prepared by solid state reaction.

Materials	Methods	Figure of merit (ZT)/Power factor (PF)	Temperature (K)	References
$Zn_{3.9}Cd_{0.1}Sb_3$	Solid state reaction	ZT = 1.3	680	Karthikeyan et al. [29]
Graphene/$CuAlo_2$	Solid state reaction	ZT = 0.0045	575	Daichakomphu et al. [30]
$Sn_{1-x}Sb_xO_2$	Solid state reaction	ZT = 0.06	1073	Macario et al.[31]
$Na_{1.2}Co_{1.8}Ag_{0.2}O_4$/rGO	Solid state reaction	PF (444 $\mu WCm^{-1}K^{-2)}$	859	Phochai et al. [32]
$Cu_{0.15}B_{0.15}Co_4Sb_{11.5}Te_{0.5}$	Solid state reaction	ZT = 0.66	814	Bai et al. [33]
$CuO_{0.75}ZnO_{0.25}$	Solid state reaction	PF (12.92 $\mu WCm^{-1}K^{-2}$)	575	Ghazi and Kadhim [34]
$La_{0.9}Ba_{0.1}FeO_3$	solid state reaction	PF (3.73 $\mu WCm^{-1}K^{-2}$)	650	Karthikeyan et al. [35]

5.2.5. Ball milling

Recently, ball milling was one of the popularly used method for preparing the nanostructured thermoelectric materials. During this process both mechanical alloying and nano structuring occurs simultaneously through a collision of events inside a high energy mill. This whole process was done inside an argon gas filled glove box to reduce the unwanted oxidation of precursor materials. Then the jar was placed in a high energy milling machine. Thus, the merit of ball milling includes high yield, with

the potential to produce kilograms of material. Additionally, the resulting nanomaterials are conducive to sintering, facilitating the formation of high-density pellets with larger grain boundaries. This characteristic is advantageous for enhancing the Seebeck coefficient and reducing lattice thermal conductivity, thereby improving the figure of merit as illustrated in **Table 5** of relevant studies. However, a major significant drawback of milling is the challenge of controlling particle size distribution, particularly as materials may lose crystallinity over prolonged milling durations. This loss of crystallinity can impact the final properties of the material, necessitating careful monitoring and optimization of milling conditions to achieve desired outcomes.

Table 5. Figure of merit values for various materials prepared by ball milling.

Materials	Methods	Figure of merit (ZT)	Temperature (K)	References
P-type $(Bi, Sb)_2Te_3$	Ball milling	1.14	323	Son et al. [36]
Higher Manganese Silicide	Ball milling followed by SPS	0.39	770	Chen et al. [37]
ZnSb	Ball milling	0.76	600	Balasubramanian et al. [38]
$Bi_{0.9}Sn_{0.1}Se$	Ball milling	0.32	473	Lu et al. [39]

5.2.6. Magnetron sputtering

This magnetron sputtering is one of the techniques in vacuum coating process which allows material deposition, such as metals and ceramics, over a substrate material with the help of suitable magnetic field, which is applied into a sputtering target. Here the deposition rate is faster at lower pressure compared to other techniques by a strong adhesive coating on a substrate. Thus sputtering deposition does not require any high melting or evaporation of the source material, which lead to many advantages compared to other PVD technologies: first, all of the materials can be deposited with the help of magnetron sputtering regardless of their melting temperature; second, sources can be scaled up and positioned anywhere within the chamber based on our requirements; Then finally, a film of alloys and compounds can be deposited over the source material by maintaining the similar composition. Here **Table 6** shows the different power factor values for different materials using the magnetron sputtering method.

Table 6. Figure of merit values for various materials prepared by magneton sputtering.

Materials	Methods	Power factor (PF)	Temperature (K)	References
Mg_3Bi_2	Magnetron Sputtering	1.1 $\mu WCm^{-1}K^{-2}$	393	Fang et al. [40]
Cu_2Se	Magnetron Sputtering	15.6 $\mu WCm^{-1}K^{-2}$	723	Rapaka et al.[41]
Mg_2Sn	Magnetron Sputtering	1.45 $\mu WCm^{-1}K^{-2}$	623	Liu et al. [42]
Bi_2Te_3	Magnetron Sputtering	0.70 & 27.3$\mu WCm^{-1}K^{-2}$	573	Kurokawa et al. [43]

5.3. Role of physical methods

The physical method also plays a pivotal role in the performance and efficiency of a thermoelectric material by tuning their key parameters. These physical methods are employed to improve the figure of merit (ZT) by tailoring the various structural, electronic and phononic properties in a material. With the help of synthesis method

and advanced computational tools one can yield a high thermoelectric performance material for practical applications [44]. There are several steps employed in the physical methods and some of them are discussed below

5.3.1. Precise control and sintering methods

Tuning of the key parameters offers an unmatched precision in a thermoelectric material. Spark Plasma Sintering (SPS) and Hot pressing is one of the sintering methods which consolidates a powder to bulk material with a controlled microstructural property [45,46].

5.3.2. Band engineering for enhancement of power factor

Through the bandgap engineering or doping strategies, we can able to modify the electronic structure to improve See-beck coefficient by maintaining electrical conductivity.

5.3.3. Reduction of thermal conductivity

Nano-structuring, alloying, interface engineering, enhancing electron transport across material junctions and increasing phonon scattering at the grain boundaries is one of the effective approaches used to reduce the lattice thermal conductivity by maintaining the electrical properties [47].

5.3.4. Minimization of material defects

Using the surface modification and controlled growth techniques such as CVD, PVD, ALD and defect engineering helps to minimize the unwanted defects in a material which can degrade their thermoelectric performance [48].

5.4. Categories of thermoelectric materials

The state-of-the-art; TE materials are broadly classified into eight main categories and detailed discussions on the different TE materials are reviewed below.

5.4.1. Half Heusler alloys

Mostly the Half-Heusler (HH) alloys are the primary focus on thermoelectric research for majority of high temperature applications. Due to its high mechanical strength, high thermal stability, high electrical conductivity, and also this HH have a moderate Seebeck coefficient when compared to other TE materials. Generally, HH alloys are known as a better TE material than full-Heusler because this HH have a small band gap, low electrical resistivity and high thermopower. Additionally, the natural vacancies are created in an unit cell either by doping or substitution in the parent elements, makes strengthening the Heusler alloys electronic properties. This HH alloys are mostly nontoxic, less expensive with the high and low melting elements. Synthesis of HH materials mostly requires a high temperature when compared to the other materials. The general procedure used for most of Half Heusler alloys is a melt technique, such as an arc melting or induction levitation melting, then it was followed by a secondary heat treatment known as the annealing, to produce a dense single-phase material. Densification using Hot Isotatic Press (HIP) or Spark Plasma Synthesis (SPS) is often implemented to reduce the porosity of material. Generally, the Half Heusler alloys prepared through various methods, and its different figure of merit values are reported in the **Table 7**.

Table 7. Figure of merit values for various Half Heusler alloys.

Materials	Methods	Figure of merit (ZT)	Temperature (K)	References
$FeNb_{0.8}Ti_{0.2}Sb$	Arc & Induction melting	0.20	800	El-khouly et al.[49]
CoTiP	Theoretical	0.95	300	Bouchrit et al. [50]
P type TiXSn (X = Ni, Pd, Pt)	Quantum ESPRESSO Packages	0.56–0.70	900	Xiong et al. [51]
NaYZ (Z = Si, Ge, Sn)	DFT	1.8–1.9	900–1200	Adeleye et al. [52]
PdMX (M = Sc, Y) & (X = P, As, Sb)	Theoretical	0.28–0.44	1000	Rani et al. [53]
$ZrNiCu_{0.05}Sn$	Arc melting	1.1	950	Yan et al. [54]
$Hf_{0.3}Zr_{0.7}Co\ (Sn_{0.3}Sb_{0.7})_{1-x}Al_x$	Arc melting followed by SPS	1.5	980	Mitra et al. [55]

5.4.2. Chalcogenides

A chalcogenide is a class of compound which has atleast one chalcogen anion (group 16 element, such as Te, Se and S) and an electropositive element (such as Bi, Pb and Sn). Mostly widely used chalcogenide in the applications of TE are based on group IV-VI compounds such as (PbTe, SnSe, GeTe, etc.) and V-VI compounds (Bi_2Te_3, Sb_2Te_3, Bi_2Se_3, etc.); these compounds are generally rock-salt structure in nature. These chalcogenides are the commonly employed materials for TE applications, almost 75% of the global market is occupied by the bismuth telluride and lead tellurides. Among the other TE materials, the above two tellurides have the high ZT reported so far. Currently Bi_2Te_3, PbTe have enhanced ZT values and used in the TE modules, but one major drawback is they are rare, toxic, high cost, too hazardous to human health and environment and brittle in nature. Recently Duong et al. developed a Bi-doped SnSe single crystal with a maximum ZT of 2.2 around 773 K; currently this was only the material which shows highest ZT value, reported so far in Bulk materials as shown in **Table 8**.

Table 8. Figure of merit values for various chalcogenides.

Materials	Methods	Figure of merit (ZT)/Power factor (PF)	Temperature (K)	References
$BaErCuS_3$, $BaGdCuS_3$	Theoretical	ZT = 0.4–0.5, ZT = 0.3-0.45	400, 800	Khan et al. [56]
Sr_2GeX_4 (X = S, Se)	Theoretical	ZT = 0.001–0.006	800	Jawad et al. [57]
Bi doped n type Sn,Se single crystals	Temperature gradient growth method	ZT = 2.2	773	Duong et al. [58]
$FeIn_2Se_4$	Conventional solid state reaction method	PF ($3.5\mu WCm^{-1}K^{-2}$)	643	Karthikeyan et al. [59]

5.4.3. Skutterudites

Skutterudites (SKUs) are a trending class of materials that gained a lot of attention within the research community since 1990s. Here by incorporating a smaller ion into the voids of skutterudite results in lowering the Thermal conductivity. Skutterudite exhibit a semiconductor like property and they have common formula AB_3, where (A = Co, Rh, Ir and B = P, As, Sb). The skutterudite materials mostly used for energy conversion are based on $CoSb_3$. Both the P and N type $CoSb_3$ shows a large power factor values compared to others. These SKU generally have a high thermal

conductivity, but it can be lowered by heavy doping or alloying. Then an alternate way to reduce the thermal conductivity is by the introduction of Rare-earth elements or Lanthanides into the voids of crystal structure, by the substitution of Fe or Ni instead of Co. Currently the La-Fe-Co-Sb and Ba-Ni-Co-Sb system yielded a figure of merit above one, at or above 600 °C. The temperature range for SKUs is nearly from RT to 900K and these SKUs based materials are used in various applications such as waste heat recovery, thermophiles and high temperature energy harvesting and used in aerospace also. The highest ZT value reached in the literature is so far around 1.9 at 823K which was shown in the **Table 9**.

Table 9. Figure of merit values for various skutterudites.

Materials	Methods	Figure of merit (ZT)/Power factor (PF)	Temperature (K)	References
Double doped CO_4Sb	High temperature vacuum melting	0.65–0.7	673	Karthikeyan et al. [60]
N-type$(R_{0.33}Ba_{0.33}Yb_{0.33})_{0.35}Co_4Sb_{12.3}$	Ball milling	1.9	823	Rogl et al. [61]
Co_4Sb_{12} & $Co_4Sb_{10.8}Se_{0.6}Te_{0.6}$	Fast SHS-PPS route	PF (0.46-2.16μWCm^{-1}K^{-2})	598-673	Kruszewski et al. [62]

5.4.4. Zintls

Zintls are a class of P-type material, which demonstrates a large potential to the field of TE community. Currently Sb, Zn, Cd based Zintls yields the high TE performance via band engineering. So far, the highest ZT in Zintls is 2.5 which was achieved around 700K through the first principle method with the Generalised Gradient Approximation (GGA) was shown in the **Table 10**.

Table 10. Figure of merit values for various Zintls.

Materials	Methods	Figure of merit (ZT)	Temperature (K)	References
Sc doped Mg_3X_2 (X = Sb, Bi)	First principle calculations	1.53	703	Yu et al. [63]
P type-Mg_3Sb_2	Ball mill & SPS	0.85	723	Zhang et al. [64]
$YbMg_2X_2$ (X = P, As, Sb, Bi)	Theoretical	0.72–0.74	950	Khan et al. [65]
P type-Mg_3sb_2	Theoretical	2.5	700	Ning et al. [66]

5.4.5. Oxyselenides

Oxyselenides are a group of compounds which contains both the oxygen and selenium atoms. This Oxyselenides are a class of compound which contains various transition metal elements, and they show a wide range of structure and properties. Recently this BiCuSeO gained a much more increased attention and they have been extensively studied and widely used as a promising material, due to its low electrical conductivity and carrier concentration by comparing to other materials, here the doping is the main strategy to improve its properties and to enhance its figure of merit of a material. The low lattice thermal conductivity due to slow transport of phonons which means less stiffness makes the Oxyselenides an attractive material. Currently there is a major demand on BiCuSeO based TE materials in the market, but many papers reviewed that by doping this BiCuSeO material with Mg, Cd or Pb and Ba

shows the higher performance. The different Oxyselenide materials with different ZT values was reported in **Table 11**.

Table 11. Figure of merit values for various Oxyselenides.

Materials	Methods	Figure of merit (ZT)	Temperature(K)	References
Sm doped BiCuSeO	Two step solid state method	0.74	873	Feng et al. [67]
Sm doped BiCuSeO	Two step solid state method	0.65	823	Kang et al. [68]
I doped Bi_2O_2Se	Solid state reaction	0.32-0.35	790	Kim et al. [69]
Pb doped BiCuSeO	Microwave synthesis combined with SPS Sintering	0.76	773	Lei et al. [70]

5.4.6. Organic-inorganic and hybrid materials

Hybrid organic-inorganic materials are a emerging new material in the Te field, due to its great potential by utilizing a lower thermal conductivity in organic materials, and high Seebeck coefficient and electrical conductivity in inorganic materials. Here the Metal-organic coordination polymers belong to a class of metal compounds where each metal tends to bind with more than a ligand to create an array of metal centres. Linearly coordinated polymers with transition-metal ions and Ethylenetetrathiolate are expected to be an attractive and highly efficient material for achieving the good electrical conductivity. Recently these hybrid perovskites, such as $CH_3NH_3PbI_3$ and $CH_3NH_3SnI_3$ have been known as an effective TE material compared to other material due to its high seebeck coefficient and low thermal conductivity. So far, Iron phthalocyanine polymer achieved the highest figure of merit 1.02 at 300K was reported by M. Bashi et al. shown in the **Table 12** using the theoretical FP-Law method.

The different ways implied for improving the TE Performance in the Hybrid Organic–Inorganic Nanocomposites.

1) By controlling a major factor, such as size, shape, morphology and dimension led to improvement of high figure of merit in a inorganic nanostructure material.
2) Modifying their properties literally improves the electrical conductivity of organic materials either through doping or by controlling the oxidation state
3) Tuning and modifying the interfaces of material led to an increased power factor by improving the Seebeck coefficient on the hybrids.

Table 12. Figure of merit values for various organic-inorganic & hybrid materials.

Materials	Methods	Figure of merit (ZT)	Temperature (K)	References
Iron phthalocyanine polymer	Theoretical	1.02	300	Bashi et al. [71]
PE DOT: PSS-Bi_2Te_3	Solution mixing	0.58	Room temperature (RT)	Wang et al. [72]
WSe_2	Electrochemical-intercalation	0.245	340	Liang et al. [73]
2AL-PR-X (X = 2H, Ni, Pt, Zn)	Theoretical	0.32,0.9	RT,800	Wu et al. [74]

6. Conclusion

Development of new and modification in existing materials have been considerably increased in thermoelectric research over the past decades. It has been perceived that due to interdependence between the key parameters such as electrical conductivity, Seebeck coefficient and thermal conductivity, various criterions and

strategies are adopted to achieve high ZT values and still yet to develop. Several mechanisms are been in trend to increase the power factor (σS^2) and to diminish the thermal conductivity (κ) to pull off high figure of merit values. Both theoretical and experimental approaches were been in a practise to move the field forward. Based on the current advances numerous TE materials were already developed and achieved reasonable ZT values of ≈ 2 with thermoelectric efficiency of ≈ 25% as potential barrier. It is anticipated that for the futuristic TE materials development various strategies has to be made to improve the ZT values to ≈ 4 with thermoelectric efficiency of ≈ 45%.

Conflict of interest: The author declares no conflict of interest.

References

1. Filonchyk M, Peterson MP, Zhang L, et al. Greenhouse gases emissions and global climate change: Examining the influence of CO_2, CH_4, and N_2O. Science of the Total Environment. 2024; 935: 173359.
2. Cassia R, Nocioni M, Correa-Aragunde N, et al. Climate Change and the Impact of Greenhouse Gasses: CO_2 and NO, Friends and Foes of Plant Oxidative Stress. Front. Plant Sci. 2018; 9: 273.
3. Ang TZ, Salem M, Kamarol M, et al. A comprehensive study of renewable energy sources: Classifications, challenges and suggestions. Energy Strategy Reviews. 2022; 43: 100939.
4. Lacetera N. Impact of climate change on animal health and welfare. Animal Frontiers. 2018; 9(1): 26–31.
5. Ozili PK, Ercan O. Global Energy Crisis: Impact on the Global Economy. SSRN Publishing; 2023.
6. Yang J, Stabler FR. Automotive Applications of Thermoelectric Materials. Journal of Electronic Materials. 2009; 38(7): 1245–1251.
7. Zheng XF, Yan YY, Liu CX, et al. A review of thermoelectrics research–Recent developments and potentials for sustainable and renewable energy applications. Renewable and Sustainable Energy Reviews. 2014; 32: 486–503.
8. Zou M, Li JF, Du B, et al. Fabrication and thermoelectric properties of finegrained TiNiSn compounds. Journal of Solid-State Chemistry. 2009; 182(11): 3138–3142.
9. Karthikeyan N, Ghanta S, Misra S, et al. Tuned thermoelectric transport properties of $Co_{2.0}Sb_{1.6}Se_{2.4}$ and $Co_{2.0}Sb_{1.5}M_{0.1}Se_{2.4}$ (M = Zn, Sn): Compounds with high phonon scattering. Journal of Alloys and Compounds. 2017; 729: 303–312.
10. Biswas K. Advances in Thermoelectric Materials and Devices for Energy Harnessing and Utilization. Proc. Indian Natn. Sci. Acad. 2015; 81(4): 903–913.
11. Amine ZM, Bourouis M, Bentouba S, et al. A Review on Thermoelectric Generators: Progress and Applications. Energies. 2020; 13: 3606.
12. Hendricks T, Caillat T, Mori T. Keynote Review of Latest Advances in Thermoelectric Generation Materials. Devices, and Technologies. 2022; 15: 7307.
13. Ma J, Chen Y, Li W, et al. Predictability of thermoelectric figure of merit for the single crystal from first principles. International Journal of Heat and Mass Transfer. 2023; 211: 0017–9310.
14. Lee KH, Kim SW. Design and Preparation of High-Performance Bulk Thermoelectric Materials with Defect Structures. Journal of the Korean Ceramic Society. 2017; 54(2): 75–85.
15. Yue Z, Zhou W, Ji X, et al. Enhanced thermoelectric properties of Ag doped Cu_2S by using hydrothermal method. Journal of Alloys and Compounds. 2022; 919(25): 16583.
16. Bai Y, Ouyang T, Wang W, et al. Graphene oxide embedded in Bi_2S_3 nanosheets by hydrothermal method to enhance thermoelectric performance. Materials Chemistry and Physics. 2023, 301(1): 127643.
17. Bai Y, Li X, Ouyang T, et al. High thermoelectric performance in the n-type Bi_2S_3/f-MWCNTs nanocomposites prepared by hydrothermal method. Carbon. 2023; 212: 18158.
18. Liu H, Zhang L, Shen Y, et al. Enhanced thermoelectric performance of $Bi_{2-x}Cu_xS_3$ by hydrothermal synthesis and spark plasma sintering. Ceramics International. 2023; 49: 36130–36136.
19. Yun YH, Ann EJ Jeong YJ. Impact of Zn-doping on the thermoelectric properties of $Bi_2Te_{2.7}Se_{0.3}$ nanostructures synthesized by hydrothermal method. Materials Letters. 2023; 346(1): 134499.

20. Zhou Z, Liu R, Yang Y, et al. Synergistic effects of CuI doping on enhancing thermoelectric performance for n-type Bi2O2Se fabricated by mechanical alloying. Scripta Materialia. 2023; 225(1): 115163.
21. Ioannou I, Ioannou P, Kyratsi T, et al. Low-cost preparation of highly-efficient thermoelectric $Bi_xSb_{2-x}Te_3$ nanostructured powders via mechanical alloying. Journal of Solid State Chemistry. 2023; 319: 123823.
22. Symeou E, Karyou M, Delimitis A, et al. Preparation of highly efficient thermoelectric Bi-doped $Mg_2Si_{0.55-x}Sn_{0.4}Gex$ (x = 0 and 0.05) materials with a scalable mechanical alloying method. Journal of Physics and Chemistry of Solids. 2022; 161: 110472.
23. Bhardwaj R, Tyagi T, Bathla S, et al. Exploration of synthesis route and effect of Ni-doping on thermoelectric performance of $CoSb_3$. Journal of Physics and Chemistry of Solids. 2024; 186: 111835.
24. He J, Shen Y, Zhai L, et al. Effects of magnetic Fe doping on the thermoelectric properties of TiNiSn nanomaterials prepared via melt spinning method. Journal of Alloys and Compounds. 2024; 975: 172808.
25. Anno H, Yamada H, Nakabayashi T, et al. Gallium composition dependence of crystallographic and thermoelectric properties in polycrystalline type-I $Ba_8Ga_xSi_{46-x}$ (nominal x = 14−18) clathrates prepared by combining arc melting and spark plasma sintering methods. Journal of Solid State Chemistry. 2012; 193: 94–104.
26. Ngugi KJ, Nam WH, Kihoi SK, et al. Detrimental effects of impurity phases on the thermoelectric performance of $Nb_{0.8}Ti_{0.2}Fe_{1.02}Sb$ synthesized by arc-melting. Journal of Alloys and Compounds. 2021; 871: 159634.
27. Mondal S, Ghosh K, Ranganathan K, et al. Thermoelectric properties of Ru_2TiGe Heusler phase. Journal of Alloys and Compounds. 2023; 961: 171050.
28. Fujimoto T, Mikami M, Miyazak H, Nishino Y. Enhanced thermoelectric performance of Ru_2TiSi Heusler compounds with Ta substitution. Journal of Alloys and Compounds. 2023; 969: 172345.
29. Karthikeyan N, Jaiganesh G, Anbarasu V, et al. Thermoelectric transport investigations on Cd/In substituted β-Zn_4Sb_3 compounds. Materials Today Communications. 2018; 14: 128–134.
30. Daichakomphu N, Sakdanuphab R, Harnwunggmoung A, et al. Achieving thermoelectric improvement through the addition of a small amount of graphene to $CuAlO_2$ synthesized by solid-state Reaction. Journal of Alloys and Compounds. 2018; 753.
31. Macario LR, Golabek A, Kleinke H, et al. Thermoelectric properties of Sb-doped tin oxide by a one-step solid-state reaction. Ceramics International. 2022; 48(3): 3585–3591.
32. Phochai T, Chueachot R, Singsoog K, et al. Enhanced thermoelectric power factor of $Na_{1.2}Co_{1.8}Ag_{0.2}O_4$ with reduced graphene oxide synthesized by the polymerized complex method and solid-state reaction. Materials Letters. 2019; 249: 1–4.
33. Bai Z, Ji Y, Li Y, et al. Effect of forming pressure on thermoelectric properties of $CoSb_3$-based skutterudite prepared by solid-state reaction. Solid State Sciences. 2022; 132: 106999.
34. Ghazi N, Kadhim A. Thermoelectric properties of solid state reaction-prepared ZnO based alloys with various CuO doping in $(CuO)_x(ZnO)_{1-x}$. Solid State Communications. 2023; 361: 115058.
35. Karthikeyan N, Kumar RR, Sivakumar K. Thermoelectric power factor of $La_{0.9}M_{0.1}FeO_3$ (M = Ca and Ba) system: Structural, band gap and electrical transport evaluations. Physica B: Physics of Condensed Matter. 2018, 529: 1–8.
36. Son JH, Oh MW, Kim BS, et al. Effect of ball milling time on the thermoelectric properties of p-type $(Bi, Sb)_2Te$. Journal of Alloys and Compounds. 2013; 566: 168–174.
37. Chen X, Shi L, Zhou J, et al. Effects of ball milling on microstructures and thermoelectric properties of higher manganese silicides. Journal of Alloys and Compounds. 2015; 641: 30–36.
38. Balasubramanian P, Battabya M, Bose AC, et al. Effect of ball-milling on the phase formation and enhanced thermoelectric properties in zinc antimonides. Materials Science and Engineering B. 2021; 271: 115274.
39. Lu W, Lai X, Liu Q, et al. Enhanced thermoelectric performance of BiSe by Sn doping and ball milling. Ceramics International. 2021, 47(18): 26375–26382.
40. Fang W, Zhu W, Shao Y, et al. Formation of metastable cubic phase and thermoelectric properties in Mg_3Bi_2 films deposited by magnetron sputtering. Applied Surface Science. 2022; 596: 153602.
41. Rapaka SS, Anwar S, Priyadarshini B, et al. The effect of sputtering power on structural, mechanical, and electrical properties of Copper Selenide Thermoelectric thin films deposited by magnetron sputtering. Materials Chemistry and Physics. 2023; 304: 127879.
42. Liu Y, Guihong S, Yusheng L, et al. Thin films of thermoelectric Mg_2Sn containing nano-sized metal Sn phase by magnetron sputtering. Chemical Physics Letters. 2022; 788: 139305.

43. Kurokawa T, Mori R, Norimasa O, et al. Influences of substrate types and heat treatment conditions on structural and thermoelectric properties of nanocrystalline Bi_2Te_3 thin films formed by DC magnetron sputtering. Vacuum. 2020; 179: 109535.
44. Gayner C, Kar KK. Recent advances in thermoelectric materials. Progress in Materials Science. 2016; 86: 330–382.
45. Delaizir G, Bernard-Granger G, Monnier J, et al. A comparative study of Spark Plasma Sintering (SPS), Hot Isostatic Pressing (HIP) and microwaves sintering techniques on p-type Bi_2Te_3 thermoelectric properties. Materials Research Bulletin. 2012; 47(8): 1954–1960.
46. Mansour MA, Nakamura K, AbdEl‐Moneim A. Enhancing the thermoelectric properties for hot‐isostatic‐pressed Bi2Te3 nano‐powder using graphite nanoparticles. J. Mater. Sci: Mater Electron. 2024; 35: 705.
47. Dong J, Liu Y, Liu J, et al. Relating Local Structure to Thermoelectric Properties in $Pb_{1-x}GexBi_2Te_4$. Chem. Mater. 2024; 36: 10831−10840.
48. Hamada T, Hamada M, Horiguchi T, et al. High Seebeck coefficient in PVD-WS_2 film with grain size enlargement. Japanese Journal of Applied Physics. 2022; 61: SC1007.
49. El-Khouly A, Egami RH, AlDien MS, et al. Thermoelectric and transport properties of half-Heusler $FeNb_{1-x}Ti_xSb$ alloys. Vacuum. 2024; 220: 112828.
50. Bouchrit A, Ahmoum H, Khamkhami JEL, et al. First principle investigation on electronic and thermoelectric properties of CoTiP half-Heusler with Co, Ti, and P vacancies. Physica B. 2024; 674: 415543.
51. Xiong M, Yang S. First-principles study on the lattice dynamics, electronic, mechanical, and thermoelectric properties of half-heusler compounds TiXSn (X = Ni, Pd, Pt). Materials Today Communications. 2024; 38: 108051.
52. Adeleye OG, Adetunji BI, Njah AN, Olusola OI. First-Principles study of the structural, electronic, elastic, lattice dynamics and thermoelectric properties of the newly predicted half-heusler alloys NaYZ (Z = Si, Ge, Sn). Solid State Communications. 2024; 378: 115413.
53. Rani B, Khandy SA, Singh J, et al. Electronic structure, elastic and transport properties of new Palladium-based Half-Heusler materials for thermoelectric applications. Materials Today Communications. 2023; 36: 106461.
54. Yan R, Shen C, Widenmeyer S, et al. The role of interstitial Cu on thermoelectric properties of ZrNiSn half-Heusler compounds. Materials Today Physics. 2023; 33: 101049.
55. Mitra M, Benton A, Akhanda MS, et al. Conventional Half-Heusler alloys advance state-of-the-art thermoelectric properties. Materials Today Physics. 2022; 28: 100900.
56. Khan MS, Gul B, Benabdellah G, et al. Tailoring the optoelectronic, thermoelectric, and thermodynamic properties of rare-earth quaternary chalcogenides: An inclusive first-principles study. Materials Today Communications. 2024; 38: 107848.
57. Jawad M, Rahman AU, Rafique Q, et al. First principle investigation of structural, electronic, optical and thermoelectric properties of Chalcogenide Sr_2GeX_4(X = S, Se). Materials Science in Semiconductor Processing. 2024; 173: 108105.
58. Duong AT, Nguyen VQ, Duvjir G, et al. Achieving ZT = 2.2 with Bi-doped n-type SnSe single crystals. Nature communications. 2016; 12(7): 13713.
59. Karthikeyan N, Aravindsamy G, Balamurugan P, et al. Thermoelectric properties of layered type $FeIn_2Se_4$ chalcogenide compound, Materials Research Innovations. 2017; 22(5): 278–281.
60. Karthikeyan N, Ghanta S, Sekaran JG, et al. Thermoelectric properties of Se and Zn/Cd/Sn double substituted Co_4Sb_{12} skutterudite compounds. Royal society of chemistry. 2017; 19(41).
61. Rogl G, Grytsiv A, Rogl P, et al. n-Type skutterudites $(R,Ba,Yb)_yCo_4Sb_{12}$ (R = Sr, La, Mm, DD, SrMm, SrDD) approaching ZT $\approx$ 2.0. Acta Materialia. 2014; 63: 30–43.
62. Kruszewski MJ, Cymerman K, Choińska E, et al. A comparative study of oxidation behavior of Co_4Sb_{12} and $Co_4Sb_{10.8}Se_{0.6}Te_{0.6}$ skutterudite thermoelectric materials fabricated via fast SHS-PPS route. Journal of the European Ceramic Society. 2024; 44(6): 3760–3766.
63. Yu L, Shi XL, Mao Y, et al. Advancing n-type $Mg_{3+\delta}Sb_{1.5}Bi_{0.47}Te_{0.03}$-based thermoelectric Zintls via sc-doping-driven band and defect engineering. Chemical Engineering Journal. 2024; 482: 149051.
64. Zhang Y, Liang JS, Liu C, et al. Enhancing thermoelectric performance in P-type Mg_3Sb_2-based Zintls through optimization of band gap structure and nanostructuring. Journal of Materials Science & Technology. 2024; 170: 25–32.
65. Khan S, Khan DF, Neffati R, et al. Electronic and thermoelectric properties of $YbMg_2X_2$ (X = P, As, Sb, Bi) zintl compounds by first-principles method. Journal of Rare Earths. 2024; 42: 147–154.

66. Ning S, Huang S, Zhang Z, et al. Band convergence boosted high thermoelectric performance of Zintl compound Mg_3Sb_2 achieved by biaxial strains. Journal of Materiomics. 2022; 8: 1086–1094.
67. Feng B, Jiang X, Pan Z, et al. Preparation, Structure, and enhanced thermoelectric properties of Sm-doped BiCuSeO oxyselenide. Materials & Design. 2020; 185: 108263.
68. Kang H, Zhang X, Wang Y, et al. Enhanced thermoelectric performance of variable-valence element Sm-doped BiCuSeO oxyselenides. Materials Research Bulletin. 2020. 126: 110841.
69. Bae SY, Kim HS, Lee SW, et al. Enhanced thermoelectric properties of I-doped polycrystalline Bi_2O_2Se oxyselenide. journal of materials research and technology. 2022;19: 2831-2836.
70. Lei Y, Zheng R, Yang H, et al. Microwave synthesis combined with SPS sintering to fabricate Pbdoped p-type BiCuSeO oxyselenides thermoelectric bulks in a few minutes. Scripta Materialia. 2021; 199: 113885.
71. Bashi M, Aliabad HAR. Electronic structure, optical properties and high thermoelectric figure of merit in iron phthalocyanine polymer: FP-LAPW comparative studies. Physica B. 2024; 674: 415542.
72. Wang L, Zhang Z, Liu Y, et al. Exceptional thermoelectric properties of flexible organic−inorganic hybrids with monodispersed and periodic nanophase. Nature communications. 2018; 9: 3817.
73. Liang J, Li Y, Yin S, et al. Flexible organic-intercalated WSe_2 hybrid: electronic structure modification and thermoelectric performance optimization. Materials Today Energy. 2023; 36: 101355.
74. Wu CW, Li F, Zeng Y, et al. et al. Machine learning accelerated design of 2D covalent organic frame materials for thermoelectrics. Applied Surface Science. 2023; 638: 157947.

Academic Publishing Pte. Ltd.

Add: 73 Upper Paya Lebar Road #07-02B-01 Centro Bianco Singapore 534818

Tel: +65 83184869

E-mail: editorial_office@acad-pub.com

Web: http://ojs.acad-pub.com/